Sea Ice Modelling in the Pikialasorsuaq: Parameter Sensitivities and Future Prospects

by

Liam Buchart

A thesis submitted in partial fulfillment of the requirements for the degree of

Master of Science

Department of Earth and Atmospheric Science

University of Alberta

Abstract

In northern Baffin Bay, of the Canadian Arctic, resides Pikialasorsuaq. Pikialasorsuaq mean "great upwelling" in Greenlandic. Also known as the North Water Polynya, polynya are regions of open water surrounded by thick pack ice. The open water generates conditions which enhance primary productivity throughout the year, and are capable supporting large marine life, making Pikialasorsuaq one of the most important ocean ecosystems on the planet. Local communities rely on the polynya for hunting, fishing, and transportation due to its open water when the rest of the region is covered in ice. The polynya forms when an ice bridge blocks ice flowing through Nares Strait in winter, prevailing winds push ice away from the bridge leaving open water.

Climate warming threatens this region. As ice thins it may move through Nares Strait more easily. Greenland melt is expected to increase and enhance the stratification. Changes to the amount of ice and stratification of the region are then predicted to have significant impacts on the wildlife and humans which call it home. The modelling of Pikialasorsuaq is a difficult task due to the complex set of dynamics which form it. Improve ments are required to better simulate the polynya currently and in the future.

I start with presenting sensitivity experiments with a high resolution sea ice model to access the importance of parameters involved in ice dynamics and mechanical redistribution. Tidal constituents, ice density, ice shear strength, ice compressive strength, and vertical resolution are modified to test their relative impact on resolving Pikialasorsuaq as well as Arctic Ocean, basin-scale sea ice. Parameter perturbation experiments impact basin-scale ice thickness and are capable of producing sea ice velocity and volume fluxes consistent with an ice bridge in Nares Strait.

A small member ensemble is used to look at the potential impact of climate change on Pikialasorsuaq. Extending from 1981-2070 changes to sea ice, ocean, and biogeochemical variables are analyzed in the context of polynya formation and maintenance. Two different warming scenarios are used in the ensemble to provide and upper and lower limit on the expected changes of the coming decades. Ice concentration and thickness diminish while the upper layers of the region become more fresh and the lower layers more saline. The surface and lower layers are found to warm significantly.

Preface

Chapter 3 of this thesis is being prepared for publication with the following authorship:

L. Buchart and P.G. Myers. I was responsible for preparing, carrying out experiments, analysis and writing. P.G. Myers provided computational resources and observational datasets as well as provided insight and manuscripts edits.

Chapter 4 of this thesis has been submitted for publication as:

Buchart, L., L. Castro de la, Guardia, Y. Xu, N. Ridenour, J.M. Marson, I. Deschepper, A.K. Hamilton, N. Grivault, and P.G. Myers (2020): Future Climate Scenarios for northern Baffin Bay and the Pikialasorsuaq (North Water Polynya) region, *Atmosphere-Ocean*.

P.G. Myers designed and carried out experiments. I was responsible for analyzing the physical variables and writing the Introduction, Methods, and Conclusion. Myself and L. Castro de la Guardia wrote the analysis and discussion. L. Castro de la Guardia carried out analysis and of the biogeochemical properties and wrote the results and discussion on this analysis. J.M. Marson and N. Ridenour provided information and analysis on the runoff product used. N. Grivault provided code for analysis. Y. Xu, I. Deschepper, and A.K. Hamilton provided insight and edits on the manuscript. P.G. Myers provided further guidance and edits.

Acknowledgements

I would first like to thank my supervisor Dr. Paul Myers. I am thankful for your unwavering support, dedication, and guidance even when receiving my emails at all hours of the day. Your efforts have helped me to grow not only as a scientist, but as a person.

To all members of the lab: Ran, Yiran, Natasha, Laura, Laura, Charlène, Yarisbel, Juliana, Andrew, Clark, Inge, Gary, Adam, Tahya, David, Alain, and Ujjwal, thank you for providing continuous support and friendship even though we had to work from home for much of our time together. Thank you to Natasha, Ran, and Yiran for guiding me through my first months in the lab, without you I would have been lost.

Thank you to my parents, Todd and Shannon, for putting up with my complaints and late night work hours. I will always be grateful for your support and cherish our backyard, patio chats. To Maiya for helping my pick the perfect colorbars and for putting up with my laptop use during our T.V. series.

Finally, I would like to thank Bailey for being there every step of the way. Thank you for being there to listen to my rambling, looking at many of my plots, and for taking my mind away from school when I needed it.

Contents

List of Figures

List of Tables

Chapter 1

Introduction

The Arctic Ocean is an estuary-like ocean, which is connected to the Pacific Ocean at Bering Strait and the North Atlantic Ocean through the narrow channels of the Canadian Arctic Archipelago (CAA), Fram Strait and the Barents Sea opening. High stratification and two distinct water origins; Pacific and Atlantic Waters (PW, AW) characterize the Arctic Ocean (e.g., Alkire et al. (2017), Karcher et al. (2012)). PW is fresh and enters the region through Bering Strait, AW enters the Arctic through the Barents Sea Opening and Fram Strait. Greater steric heights in the north Pacific drive a through-flow towards the north Atlantic, i.e., the Transpolar Drift (Steele and Ermold, 2007). Another key aspect of the Arctic surface circulation is the wind-driven, anticyclonic Beaufort Gyre. The Beaufort Gyre acts an area of freshwater storage due to Ekman pumping which drives flow towards the center of the gyre (e.g., Morison et al. (2012)). Both the CAA and Fram Strait are major locations of Arctic outflow in terms of volume, freshwater and sea ice fluxes. Fram Strait is the primary gateway with a volume transport of $2.33 \pm 0.56Sv$ (Dickson et al. (2007), McGeehan and Maslowski (2012)), the CAA volume flux is estimated to be $\sim 1Sv$ (Petersen et al., 2012). Aagaard and Carmack (1989) estimate that the Fram Strait freshwater volume transport is $820km^3/yr.$ and through the CAA is $920km^3/yr$, both relative to a salinity of 34.8. The vertical structure of the Arctic ocean is influenced by the amount of freshwater present and is defined by a strong halocline. The halocline separates a salty $(34.8 - 35)$ lower layer composed of north Atlantic inflow, and a thin, $\sim 300m$ thick, surface fresh layer (Alkire et al., 2017). The Arctic Ocean is seasonally covered by a sea ice canopy which isolates the surface layers from the atmosphere.

1.1 Arctic Ocean Sea Ice

Arctic Ocean sea ice is characterized by a maximum thickness to the west of Ellesemere Island, thickness is found to decrease towards the Siberian coast (Kwok and Rothrock, 2009). Ekman transport causes ice to build up along the west coast of the CAA (McGeehan and Maslowski, 2012). This thick, deformed ice along the CAA has a winter mean thickness of $3.4m$, though there are areas which have mean ice thicknesses of $5.5m$ (Melling, 2002). The 1980 mean, winter thickness is measured to be $3.64m$, this values was measured to be $1.89m$ in 2008 (Kwok and Rothrock, 2009). Sea ice covers roughly $15 \times 10^6 km^2$ of the polar and subpolar oceans in the winter and

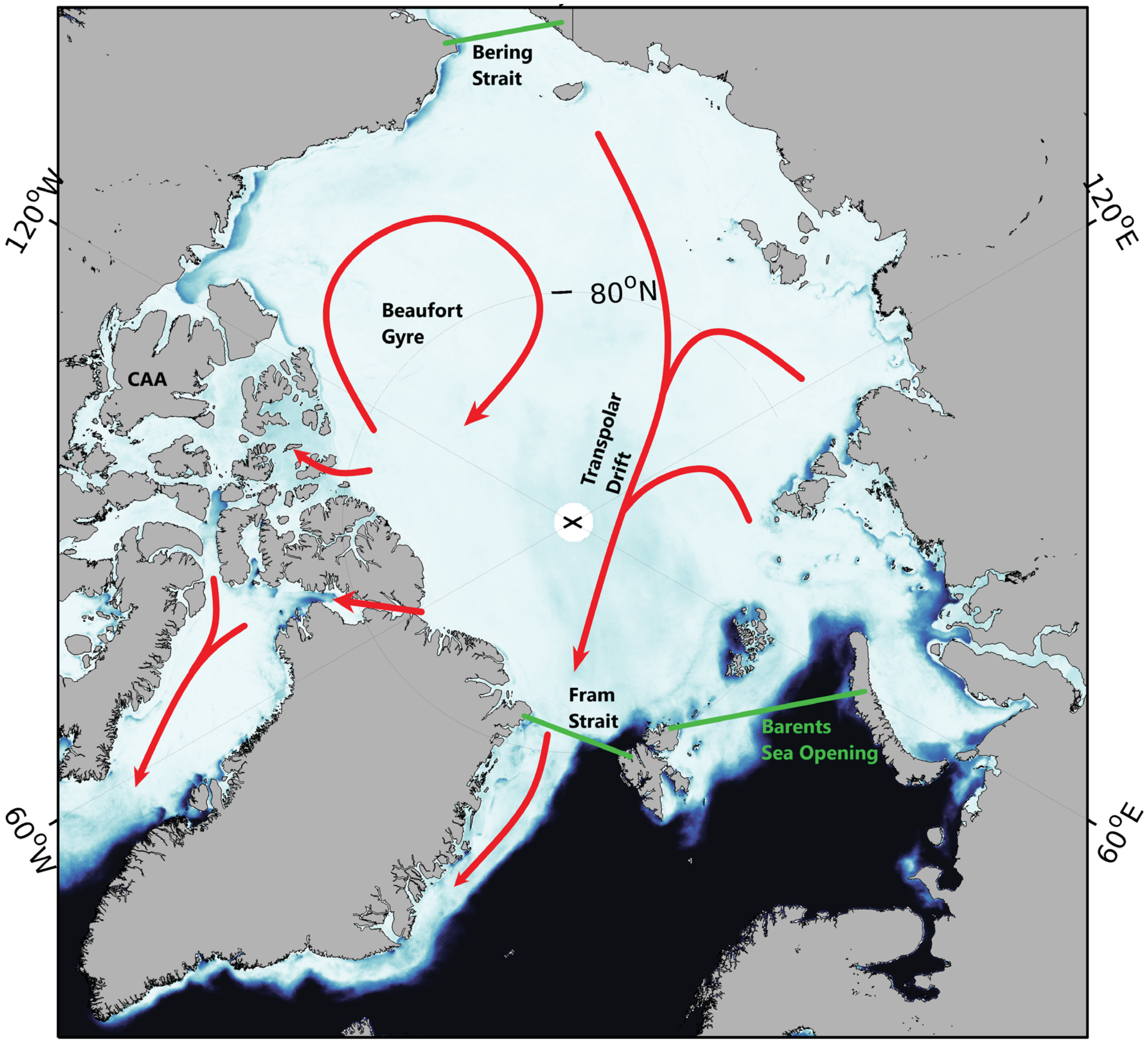

Figure 1.1: Red arrows represents Arctic Ocean idealized general sea ice circulation. Green lines represent major Arctic gateways. The black "X" at center is the North Pole. CAA = Canadian Arctic Archipelago. Background sea ice plots comes from the AMSR2 sea ice concentration (Spreen et al. (2008), Melsheimer and Spreen (2019))

$\sim 5 - 7 \times 10^6 km^2$ during the summer minimum (Cavelieri and Parkinson, 2012). In winter, the Arctic Ocean is almost entirely covered by sea ice. Summer melt creates a more mobile ice pack, leading to enhanced sea ice export (e.g., Howell et al. (2013)). The Arctic sea ice cover is composed, primarily of two different types of ice: first-year and multi-year ice. First-year ice is thin and has a surface salinity of $10 - 12$. Multi-year ice is defined to have survived at least a full melt season and has a surface salinity which is ~ 0 (Comiso, 2012).

There are two key aspects to Arctic sea ice circulation: the Beaufort Gyre (Howell et al., 2016) and a persistent linear drift from Siberia towards Fram Strait, i.e. the Transpolar Drift (Kwok et al., 2013). The Beaufort Sea is known as a location where sea ice thickens and ages before recirculating across the Arctic. Ice volume and transport is important due to the role sea ice plays in transporting freshwater (e.g.Aagaard and Carmack (1989)). There is found to be an ice-area transport of 94 $\pm 92 \times 10^3 km^2$ across the Central Beaufort (Howell et al., 2016). Fram Strait is the primary gateway where sea ice exits the Arctic, the average annual ice export is $2400 \pm 640 km^3$ (Spreen et al., 2020). Further, Spreen et al. (2020) estimate that 14% of the total Arctic sea ice volume moves through Fram Strait each year. A non-negligible volume of sea ice exits the Arctic via the CAA and Nares Strait, where it can melt, recirculate back into the Arctic Ocean, or move into Baffin Bay. M'Clure Strait and the Queen Elizabeth Islands are the major gateways of ice into and out of the CAA. M'Clure Strait has a 1997-2012 mean May to September ice area flux of $1 \pm 21^3 km^2$ and the Queen Elizabeth Islands have a ice area flux of $-8 \pm 8 \times 10^3 km^2$, where a positive flux corresponds to CAA inflow Howell et al. (2013). The 1996-2002 Nares Strait ice area flux is found to be $33 \times 10^3 km^2$ (Kwok, 2005). In Nares Strait, like other regions throughout the Arctic, an ice bridge can form and create what is known as the North Water Polynya (NOW).

1.2 Pikialasorsuaq Region

Polynya are unique features of high latitude oceans. A polynya is defined as a region of open water or reduced sea ice cover, surrounded by thick, pack ice. Open water in polynyas increases the ocean response to atmospheric forcing and enhances the ocean-air heat flux (Ingram et al., 2002). These regions of open water would typically be covered by ice. Lower ice cover in polynyas enhances primary production for longer periods of time compared to surrounding waters and create conditions capable of supporting large sea mammals (Ingram et al. (2002), Mei et al. (2003)). Brine rejection generated by ice formation in the open water increases vertical convection and mixing of nutrients to the surface of the water column (Melling et al. (2002), Ingram et al. (2002)). Diverging ice conditions are necessary to form polynyas as well as an upwelling of oceanic heat.

Pikialasorsuaq (also known as the North Water) meaning 'the great upwelling' in Greenlandic, is one of the largest reoccurring polynyas in the Arctic (Ingram et al., 2002, Figure 1.2b). It is also one of the most productive ocean ecosystems on the planet. The polynya is formally defined as the area between Ellesmere Island and Greenland, spanning $76^\circ - 78.5^\circ N$ (Ingram et al., 2002). Pikialaorsuaq is a critical hunting, fishing, and transportations grounds for local Greenlandic and Inuit communities due to the lower ice cover year-round (Ingram et al., 2002). In the winter or early spring, when ice is at its maximum thickness (and strength), an ice bridge forms in the south end of Kane Basin in Nares Strait. The amount of multi-year ice which moves south through Nares Strait year-to-year determines the ice bridge formation (Ingram et al. (2002), Dumont et al. (2009)). The ice bridge takes the form of a concave arch (also known as ice arches) (Dumont et al., 2009). When Pikialasorsuaq is not present, northern Baffin Bay receives thick, multi-year ice from the Arctic ocean via Nares Strait. Kwok (2005) estimate that $130km^3 (\sim 4mSv)$ of ice moves through Nares Strait each year. Winds and open water create enhanced sea ice velocities in northern Baffin Bay up to $16cm/s$ (Grivault and Myers, 2018). These winds force an Ekman transport towards the western side of the Smith Sound (Melling et al., 2002). Persistent northerly winds advect ice southward, leaving open ocean conducive to new ice growth. Ice forms in open water when the polynya is present and temperatures are cool enough in the autumn, winter, and spring months. Latent heat release due to ice formation plays a role in the maintenance of the polynya adjacent to the Greenland coast (Melling et al. (2002), Yao and Tang (2003)). Ice growth rates can exceed $1.2m/month$ in the open water of the polynya (Yao and Tang, 2003). Convection related to brine rejection during ice growth enhances the surface heat flux and can reach $30-60Wm^{-2}$ (Yao and Tang, 2003). Open water next to the Greenland coast is formed by Ekman transport away from the coast (Melling et al., 2002). However, Ingram et al. (2002) emphasized that the ice arch and subsequent diverging ice conditions are of first-order importance to the formation of Pikialasorsuaq. In the early summer, ice melts and the ice bridge breaks down, dissipating the polynya as sea ice moves southward Vincent (2019). During the summer months the polynya is not present at any time.

Maxwell (1981) describe the the climate of Pikialasorsuaq as unique to the Canadian Arctic islands as it is often impacted by low pressure systems which stop and dissipate in the region, thus bringing greater precipitation than adjacent regions. Enhanced precipitation combined with the open water of the polynya give the region a more maritime climate compared to the CAA. This is evident in the mean, winter surface air termperatures of the region. Over northern Baffin Bay the temperature ranges from $-33°C$ to $-36°C$, in the polynya the temperature increases to $-22°C$. Winter winds in Pikialasorsuaq are from the northwest and aid in moving ice out of the region Ingram et al. (2002). The strongest winds occur at the center of channels (such as through Kennedy Channel) due to the topography of the region. Finally, cyclonic atmospheric stress drives surface circulation across northern Baffin Bay (Yao and Tang, 2003).

Three straits connect Baffin Bay to the Arctic at Lancaster Sound, Jones Sound, and Smith Sound. Davis Strait connects Baffin Bay to the Labrador Sea and north Atlantic. Davis Strait has both the largest volume and freshwater fluxes, followed by Lancaster Sound and Nares Strait (Curry et al. (2011), McGeehan and Maslowski (2012), Petersen et al. (2012), Curry et al. (2014), Munchow2015, Münchow (2016)). Flows in Baffin Bay are mainly in barotropic, geostrophic balance (Morison et al., 2012). The West Greenland Current (WGC) and Baffin Island Current (BIC) are the two most prominent features of the surface circulation in Baffin Bay (Curry et al., 2011). Both currents have multiple branches, velocity cores, and eddies (Morison et al., 2012).The WGC carries warm, salty Irminger north through Davis Strait and the BIC carries cool, fresh Arctic Water south-

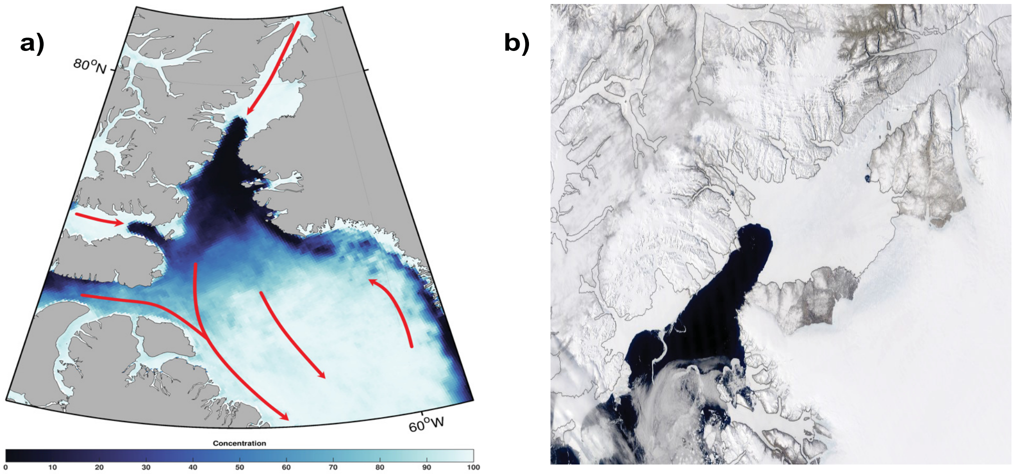

Figure 1.2: a) Red arrow represent Pikialasorsuaq region idealized general sea ice circulation. Background sea ice plots comes from the AMSR2 sea ice concentration (Spreen et al. (2008), Melsheimer and Spreen (2019)) b) MODIS Satellite image of Pikialasorsuaq (North Water Polynya), February 14, 2020. `https://eoimages.gsfc.nasa.gov/images/imagerecords/146000/146791/naresstrait_tmo_2020142_lrg.jpg`.

ward(Morison et al., 2012). Melling et al. (2002) describe the surface circulation of Baffin Bay as follows: the WGC flows northward along the coast of Greenland to $\sim 75°N$, where is crosses northern Baffin Bay, just south of the typical southern end of Pikialasorsuaq. The WGC then crosses the northern part of Baffin Bay and joining the BIC. The BIC is fast flowing ($10-15cm/s$) and roughly follows the bathymetry and flows southward from Smith Sound and then along the coast of Baffin Island. Similar patterns are observed at both the surface and at $500m$ depth.

Pikialasorsuaq and adjacent regions are highly stratified and the mixed-layer depth (MLD) is not consistent. The greatest MLDs are found on the eastern portion of Baffin Bay. The western side, adjacent to Ellesemere Island has shallower MLDs due to the large volume of Arctic Waters (cool, fresh) which occupies the majority of the water column (Melling et al., 2002). When the polynya is present in the winter and spring, open water decreases stratification and promotes vertical mixing which brings nutrients and heat to the surface (Melling et al., 2002).

1.3 Climate Change

Recent surface air temperature changes are attributed to anthropogenic forcing (e.g., Johannessen et al. (2004)). Losses in the Arctic sea ice cover are attributed to anthropogenic warming, this has replaced natural variability as the dominant force in ice cover changes (Sou and Flato, 2009). Sea ice acts as a primary indicator of climate change due to its role in the high-latitude climate due to the ice-albedo feedback and subsequent relation to Arctic amplification. From 1979-2006 there is an overall negative trend in the sea ice extent of $-45100 \pm 4600 km^2/yr$. (Cavelieri and Parkinson, 2012). Further, all twelve months show negative sea ice extent trends. Over the satellite period (1979-2006), sea ice extent has decreased at a rate of $-9.1\%/decade$ (Stroeve et al., 2007). Thick multi-year ice extent loss is even larger at $-15.6\%/decade$ (Comiso, 2012). The Arctic is moving towards a first-year ice regime where no ice may survive the summer melt season (Howell et al., 2015). There is found to be a mean ice thickness decrease of $1.75m$, from $3.64m$ to 1.89 over the ICESat period (1958-2008) (Kwok and Rothrock, 2009). A diminished ice cover is responding more readily to wind forcing and sea ice velocities are increasing (Kwok et al., 2013). More ice is moving into regions which promote melting. Kwok and Rothrock (2009) found a muting of the annual cycle of ice growth caused by warmer winters and shorter ice growth seasons. Ice losses are leaving the surface of the Arctic ocean exposed to the atmosphere and freshwater is increasing ocean stratification and the resulting impact on ocean mixing and stratification expected to be significant.

Climate change is expected to have a large impact on Pikialasorsuaq region as the freshwater fluxes from the Greenland Ice Sheet and CAA glaciers increase (Dukhovskoy et al., 2016). There is predicted to be a salinity decrease of 0.2 near the coast of Greenland from 2012-2016 associated with enhance melt (Dukhovskoy et al., 2019). An increasing Greenland freshwater flux is expected to produce a negative salinity trend in the top $300-500m$ of the subpolar basins, though no trend is observed below $500m$. This study also emphasizes that there is uncertainty in the depth to which enhanced freshwater discharge can mix and to the related impact on the stratification in Baffin Bay. Bamber et al. (2018) found that the Greenland freshwater contribution to Baffin Bay and adjacent regions was $514km^3/yr.$ from 2000-2010 and increases to $563km^3/yr.$ from 2007-2016. The Greenland freshwater flux is expected to continue increasing in the future and impact Baffin Bay and Pikialasorsuaq. A thinning ice cover is expected to weaken the ice bridge at the south end of Kane Basin, making the polynya less stable. The ice bridge is decreasing in duration by $2.1 days/year$ over a period of 1979-2019 (Vincent, 2019).

Ice losses will impacts the Arctic ranging from wildlife habitats, to northern communities hunting, fishing, and transportation practices. In recent decades, ice-ocean models have become the foremost tool for studying large-scale sea ice properties and to predict future ice regimes. Ice-ocean models are critical due to the challenges which come with making direct observation across the Arctic, particularly in winter. However, ice-ocean models are underforecasting sea ice losses (Stroeve et al., 2007). Modelling the Arctic and sub-Arctic sea, as well as sea ice is a complex process with many advantages and shortcomings to consider. Further, the use of ice-ocean models requires a knowledge of the Arctic system and observations are required to verify and motivate model experiments. Improvements to the current ice-ocean models are necessary to continue to make more accurate predictions of the future and current state of the Arctic ocean and sea ice. Improving knowledge in these areas will be critical in the near future to help the wildlife and people of the north best adapt to and prepare for changes which are already occurring.

1.4 Thesis Objectives

1. Assess key parameters in a state-of-the-art sea ice model (Louvain-la-Neuve LIM3) in modelling Arctic and Pikialasorsuaq sea ice. Then further, choose a set of tuned parameters which best model sea ice for both regions in terms of satellite observed ice concentration and thickness.

Modern sea ice models use many parameters to accurately represent sea ice, many of which are not bound by physical observations (Hunke, 2010). Determining how important different parameters are to the model output guides future experiments and model development. Studies by Hunke (2010), Dumont et al. (2009), and Holland et al. (1993) provide a framework for assessing the relative impact of certain parameters. Hunke (2010) found that sea ice thickness is sensitive to sea ice conductivity, mechanical redistribution, oceanic heat flux, and ice-ocean dynamic stress, and shortwave radiation. Dumont et al. (2009) found that ice arches are sensitive to the ice stiffness and shear strength of ice. Holland et al. (1993) found large sensitivities to the cloud cover percentage and the albedo parameterization. However, Hunke (2010) found that tuning the albedo can lead to complex and unknown feedbacks in the sea ice system. Chapter 3 will aim to better understand the impact of key model parameters on the mean state and seasonal cycle of sea ice. Model output studied includes sea ice thickness and concentration, mean circulation, and ice volume fluxes. The parameters looked at in this study are: the inclusion of tidal constituents, ice density, ice shear strength, ice compressive strength, and the number of ice categories used in the model. Two regions are of interest: Arctic, on the basin-scale and Pikialasorsuaq in northern Baffin Bay. An emphasis of the sensitivity study in chapter 3 is placed on resolving the ice arch in Nares Strait and which model parameters can produce a realistic polynya in terms of ice volume fluxes and ice concentration year-to-year. Parameter perturbations which move model output closer the observed is then deemed desirable for future studies.

2. Analyze the potential impact of climate warming on Pikialasorsuaq and adjacent regions. Predict the state of the polynya and the changes in oceanic temperature, salinity, stratification, and primary production which are expected to accompany Arctic warming.

Climate change and Arctic warming pose a significant threat to fragile Arctic ecosystems. Pikialasorsuaq is no exception. Enhanced freshwater input (e.g., Bamber et al. (2018), Dukhovskoy et al. (2019)) and melting sea ice (e.g., Sou and Flato (2009), Comiso (2012)) put into question the stability of the polynya (Vincent, 2019). Ice-ocean models are necessary to make predictions to the future state of the region. Chapter 4 uses a numerical model assess the potential impact of climate change on Pikialsorsuaq and adjacent areas to the year 2070. There have been countless studies on Arctic basin scale changes to sea ice, though the small regional impacts are of greater uncertainty. The study aims to understand how sea ice thickness, concentration, and ice fluxes will change in the coming decades. Additionally, to predict potential impacts on oceanic heat, salinity, and mixed layer depth driven by climate warming, enhanced Greenland runoff, and changes to the sea ice regime. Finally, the role in which Atlantic Waters penetrating northern Baffin Bay play in these changes due to the significant amounts of heat and salt this water mass brings to the region. Impacts on ocean and sea ice properties are then analyzed in terms of the formation and stability of the polynya in the future.

Bibliography

Aagaard, K. and Carmack, E. (1989). The role of sea ice and other freshwater in the arctic circulation. *Journal of Geophysical Research*, 94:14485–14498.

Alkire, M., Morison, J., Schweiger, A., Zhang, J., Steele, M., Peralta-Ferriz, C., and Dickinson, S. (2017). A meteoric water budget for the arctic ocean. *Journal of Geophysical Research: Oceans*, 122:10020–10041.

Bamber, J., Tedstone, A., King, M., Howat, I., Enderlin, E., van den Broeke, M., and Noel, B. (2018). Land ice freshwater budgets of the arctic and north atlantic oceans: 1. data, methods, and results. *Journal of Geophysical Research: Oceans*, 123.

Cavelieri, D. and Parkinson, C. (2012). Arctic sea ice variability and trends, 1979-2006. *J. Geophys. Res.*, 113.

Comiso, J. (2012). Large decadeal decline of the arctic multiyear ice cover. *Journal of Climate*, 25:1176–1193.

Curry, B., Lee, C., and Petrie, B. (2011). Volume, freshwater, and heat fluxes through davis strait, 2004-2005. *J. Phys. Oceanogr.*, 41:429–436.

Curry, B., Lee, C., Petrie, B., Moritz, R., and Kwok, R. (2014). Multiyear volume, liquid freshwater and sea ice transport through davis strait, 2004-2010. *J. Phys. Oceanogr.*, 44:1244–1266.

Dickson, R., Rudels, B., Dye, S., Karcher, M., Meincke, J., and Yashayaev, I. (2007). Current estimates of freshwater flus through arctic and sub-arctic seas. *Progress in Oceanography*, 73:210–230.

Dukhovskoy, D., Myers, P., Platov, G., Timmermans, M.-L., Curry, B., Proshutinsky, A., Bamber, J., Chassignet, E., Hu, X., Lee, C., and Somavilla, R. (2016). Greenland freshwater pathways in the sub-arctic seas from model experiments with passive tracers. *Journal of Geophysical Research*, 121:1–31.

Dukhovskoy, D., Yashayaev, I., Proshutinsky, A., Bamber, J., Bashmachnikov, I., Chassignet, E., Lee, C., and Tedstone, A. (2019). Role of greenland freshwater anomaly in recent freshening in the subpolar north atlantic. *Journal of Geophyiscal Research: Oceans*, 124.

Dumont, D., Gratton, Y., and Arbetter, T. (2009). Modeling the dynamics of the north water polynya ice bridge. *Journal of Physical Oceanography*, 39:1448–1461.

Grivault, N. and Myers, P. (2018). Impacts of surface stress on volume and freshwater transport in the canadian arctic archipelago from a high resolution numerical simulation. *Journal of Geophysical Research*, 123:9038–9060.

Holland, D., Mysak, L., Manak, D., and Oberhuber, J. (1993). Sensitivity study of a dynamic thermodynamic sea ice model. *Journal of Geophysical Research: Oceans*, 98.

Howell, S., Brady, M., Derkens, C., and Kelly, R. (2016). Recent changes in the sea ice area flux through the beaufort sea during the summer. *Journal of Geophysical Research: Oceans*, 121:2659–2672.

Howell, S., Derkksen, C., Pizzolato, L., and Brady, M. (2015). Multiyear ice replenishment in the canadian arctic archipelago: 1997-2013.

Howell, S., Wohlleben, T., Dabboor, M., Derksen, C., Komarov, A., and Pizzolato, L. (2013). Recent changes in teh exchange of sea ice between the arctic ocean and the canadian arctic archipelago. *Journal of Geophysical Research: Oceans*, 118:3595–3607.

Hunke, E. (2010). Thickness sensitivities in the cice sea ice model. *Ocean Modelling*, 34:137–149.

Ingram, R., Bácle, J., Barber, D., Gratton, Y., and Melling, H. (2002). An overview of physical processes in the north water.

Johannessen, O., Bengtsson, L., Miles, M., Kuzmina, S., Semenov, V., Alakseev, G., Nagurnyi, A., Zakharov, V., Bobylev, L., Pettersson, L., Hasselmann, K., and Cattle, H. (2004). Arctic climate change: observed and modelled temperature and sea-ice variability. *Tellus A: Dynamic Meteorology and Oceanography*, 56:328–341.

Karcher, M., Smith, J., Kauker, F., Gerdes, R., and Smiethie, W. (2012). Recent changes in the arctic ocean circulation revealed by iodine-129 observations and modelling. *Journal of Geophysical Research*, 117.

Kwok, R. (2005). Variability of nares strait ice flux. *Journal of Geophysical Research Letters*, 32.

Kwok, R. and Rothrock, D. (2009). Decline in arctic sea ice thickness from submarine and icesat record: 1958-2008. *Geophysical Research Letters*, 36.

Kwok, R., Spreen, G., and Pang, S. (2013). Arctic sea ice circulation and drift speed: decadal trends and ocean currents. *Journal of Geophysical Research: Oceans*, 118:2408–2425.

Maxwell, J. (1981). Climate regions of the canadian arctic archipelago. *Arctic*, 34:225–240.

McGeehan, T. and Maslowski, W. (2012). Evaluation and control mechanisms of volume and freshwater export through the canadian arctic archipelago in a high-resolution pan-arctic ice-ocean model. *Journal of Geophysical Research*, 117.

Mei, Z.-P., Legendre, L., Gratton, Y., Trembley, J.-E., LeBlanc, B., Klein, B., and Gosselin, M. (2003). Phytoplankton production in the north water polynya: size-fractions and carbon fluxes, april to july 1998.

Melling, H. (2002). Sea ice of the northern canadian arctic archipelago. *J. Geophys. Res.*, 107(3181).

Melling, H., Gratton, Y., and Ingram, G. (2002). Ocean circulation within the norh water polynya of baffin bay. *Atmosphere-Ocean*, 39:301–325.

Melsheimer, C. and Spreen, G. (2019). Amsr2 asi sea ice concentration data, arctic, version 5.4 (netcdf) (july 2012 - december 2018). *PANGAEA*.

Morison, J., Kwok, R., Peralta-Ferriz, C., Alkire, M., Rigor, I., Andersen, R., and Steele, M. (2012). Changing arctic ocean freshwater pathwats. *Nature*, 481.

Münchow, A. (2016). Volume and freshwater flux observations from nares strait to the west greenland at daily time scales from 2003 to 2009. *J. Phys. Oceangr.*, 46:141–157.

Petersen, I., Hamilton, J., Prinsenberg, S., and Pettipas, R. (2012). Wind forcing and volume transport through lancaster sound. *Journal of Geophysical Research*, 117.

Sou, T. and Flato, G. (2009). Sea ice in the canadian arctic archipelago: Modelling the past (1950-2004) and future (2041-2060). *Journal of Climate*, 22:2181–2198.

Spreen, G., de Steur, L., Divine, D., Gerland, S., Hansen, E., and Kwok, R. (2020). Arctic sea ice volume export through fram strait from 1992 to 2014. *Journal of Geophysical Research: Oceans*, 125.

Spreen, G., Kaleschke, L., and Heygster, G. (2008). Sea ice remote sensing using amsr-e 89 ghz channels. *J. Geophys. Res.*, 113(CO2S03).

Steele, M. and Ermold, W. (2007). Steric sea level change in the northern seas. *Journal of Climate*, 20:403–417.

Stroeve, J., Holland, M., Meier, W., Scambos, T., and Serreze, M. (2007). Arctic sea ice decline: Faster than forecast. *Geophysical Research Letters*, 34(L09501).

Vincent, R. (2019). A study of the north water polynya ice arch using four decades of satellite data. *Science Reports*, 9(20278).

Yao, T. and Tang, C. (2003). The formation and maintenance of the north water polynya. *Atmosphere-Ocean*, 4(3):187–201.

Chapter 2

Model Description

This thesis used the Nucleus for European Modelling of the Ocean (NEMO) ocean modelling framework. All work done uses NEMO version 3.6 (Madec, 2008). NEMO consists of four main components; Océan PArallélisé (OPA) which is used for ocean dynamics and thermodynamics, the Louvain-la-Neuve (LIM) sea ice model (Vancoppenolle et al. (2009), Rousset et al. (2015)), and Tracer in the Ocean Paradigm (TOP) for online oceanic tracer transports, finally, there is a biogeochemical dynamics module.

The focus of this chapter is on the sea ice module and, to a lesser extent, the ocean model of which a comprehensive description can be found in Madec (2008). A brief overview of the ocean model is given in section 2.1 and key aspect of the sea ice model are presented in section 2.2.

2.1 Ocean Model

2.1.1 Primitive Equations

OPA uses primitive equations written in curvilinear coordinates to describe ocean dynamics and thermodynamics. The model uses two horizontal, unit vectors **i, j**, which are perpendicular to the vertical, unit vector **k**. They are as follows:

Horizontal equation of motion:

$$\frac{\partial \mathbf{U}_h}{\partial t} = -[(\nabla \times \mathbf{U}) \times \mathbf{U} + \frac{1}{2}\nabla(\mathbf{U}^2)]_h - f\mathbf{k} \times \mathbf{U}_h - \frac{1}{\rho_o}\nabla_h P + D^U + F^U \tag{2.1}$$

where U is the velocity vector ($\mathbf{U} = \mathbf{U}_h + \omega\mathbf{k}$), $\mathbf{U}_h$ is the horizontal velocity vector and ω is the vertical velocity, f is the Coriolis term, $\rho_0 = 1026 kg/m^3$ is the reference density, and P is the pressure. Hence, on the left hand side, the horizontal acceleration is equal to the terms on the right-hand-side (RHS), which, from left to right, are; the inertia or non-linear processes, Coriolis, pressure gradient, and the effects of small-scale physics parameterizations of turbulent mixing, convection, diffusion, and friction, and finally, boundary inputs.

Hydrostatic equilibrium;

$$\frac{\partial P}{\partial z} = -\rho g \tag{2.2}$$

Incompressibility equation:

$$\nabla \cdot \mathbf{U} = 0 \tag{2.3}$$

Temperature Conservation:

$$\frac{\partial T}{\partial t} = -\nabla \dot{(} T\mathbf{U}) + D^T + F^T \tag{2.4}$$

Salinity Conservation:

$$\frac{\partial S}{\partial t} = -\nabla \dot{(} S\mathbf{U}) + D^S + F^S \tag{2.5}$$

Terms in the temperature (salinity) conservation equation(s) from left to right are the change in temperature (salinity) over time, heat (salt) divergence and the impacts of small-scale physics parameterizations of turbulent mixing, convection, diffusion, and friction, and last, surface and boundary forcings on temperature (salinity).

Equation of State:

$$\rho = \rho(T, S, P) \tag{2.6}$$

2.1.2 Assumptions

The NEMO modelling framework uses six assumptions to solve primitive equations 2.1 - 2.6 (Madec, 2008):

Boussinesq Approximation

The Boussinesq approximation is used as the density of the open ocean varies by a few percent from the surface to depth. In the Boussinesq approximation, density changes are only considered in the buoyancy force. In the approximation volume is conserved.

Hydrostatic Approximation

The vertical momentum equation is reduced to balance between the pressure gradient and buoyancy force (equation 2.2). This approximation is valid since horizontal flow magnitudes are far larger than that of vertical flows. Vertical accelerations are parameterized when convective processes drive vertical velocities that are similar or larger than the horizontal and the hydrostatic approximation does not hold.

Incompressibility Approximation

Seawater is assumed to be incompressible ($\frac{D\rho}{Dt} = 0$), giving a parcel of seawater a constant volume during motion. When this is combined with the continuity equation, results in the the divergence of the three dimensional velocity being equal to zero as shown in equation 2.3.

Spherical Earth

The earth is considered to be a perfect sphere, giving a constant gravitational acceleration ($9.8ms^{-2}$). Gravitational acceleration is represented as a vertical vector perpendicular to a tangent of Earth's surface.

Thin-shell Approximation

Earth's radius is assumed to be large compared to the ocean depth. This is reasonable as the mean ocean depth is $\sim 4km$ with a maximum of $\sim 10km$, while Earth's radius is assumed to be $6400km$. This approximation assumes the distance from the center of the earth to any point on the model grid is a constant values equal to Earth's radius.

Turbulent Closure Hypothesis

The impacts of turbulence and small-scale processes on the mean flow are described in terms of large scale features. Describing turbulence necessitates several unknowns, which do not have equations describing them, to be solved for. This gives more unknowns than there are equations, meaning that the system is not closed Stull (1988). The system is closed with a turbulent kinetic energy scheme based on a turbulent mixing length scale (Madec et al., 2008).

2.1.3 Coordinate System

In order to avoid convergence at the North Pole curvilinear ocean coordinates are transformed to have a tri-polar grid which has two geometric poles; one over Canada and the other over Russia. The grid is used to represent all dynamic processes on the idealized sphere used to represent Earth. Curvilinear coordinates are derived from Cartesian coordinates using a transformation to generate curved coordinate lines. Three orthogonal vectors are used (**i, j, k**). **i** and **j** are tangential to the sphere and represent horizontal motion, while **k** is parallel to the gravitational force and points upwards. The coordinate system is defined by latitude (λ), longitude (ϕ), and radial distance from the center of Earth. This system can be though of in the same manner as classical spherical coordinates.

To account for curved grid lines, grid cell sizes are defined by three variables e_1, e_2, and e_3, which are also known as the scale factors:

$$e_1 = (a+z)[(\frac{\partial \lambda}{\partial i} cos\phi)^2 + (\frac{\partial \phi}{\partial i})^2]^{1/2} \tag{2.7}$$

$$e_2 = (a+z)[(\frac{\partial \lambda}{\partial j} cos\phi)^2 + (\frac{\partial \phi}{\partial j})^2]^{1/2} \tag{2.8}$$

$$e_3 = (\frac{\partial z}{\partial k}) \tag{2.9}$$

It is evident that e_1 and e_2 are independent of k.

In the vertical, z-coordinates are used with a partial step in the bottom layer to better represent bathymetry (Figure 2.1). As shown in equation 2.9 layer thickness is only a function of of z, giving a uniform thickness as a specified depth over the entire domain. This is done to divide the vertical coordinate into levels, each with a single thickness. However the bottom cell thickness is allowed to vary according to the input bathymetry product. The bathymetry product also defines the coastline.

The ocean mesh used is Arakawa's C grid. Arakawa's C grid have scalar points T, S, P, and ρ centered in each cell. Velocity vector points u, v, w are defined at the center of each face (vertical and horizontal). Finally, at the middle of each vertical edge the planetary and relative vorticities are defined.

2.1.4 Boundaries

There are two boundaries of concern in ocean models; the boundary with the bathymetry and the ocean surface. The ocean floor boundary is defined as; $z = -H(i, j)$, and the ocean surface is defined as; $z = \eta(i, j, k, t)$. Where η defines the sea surface height which is allowed to change over time. The ocean bathymetry is set as a solid wall whereas the the model allows an exchange of fluxes at the ocean surface. These fluxes include; freshwater, heat, momentum, and salt. Surface flux contributions come from the coastline (e.g. runoff), atmosphere (e.g. precipitation), and sea ice (e.g. brine rejection).

Ocean Surface Boundary

At the ocean surface there are several important exchanges of heat, salt, momentum, and freshwater which come from the atmosphere or sea ice. Given these exchanges, there is a displacement of the sea surface boundary which is governed by the the kinematic surface condition:

$$\omega = \frac{\partial \eta}{\partial t} = \mathbf{U}_h|_{z=\eta} \cdot \nabla_h \eta + (P - E + R + I) \tag{2.10}$$

here, $\mathbf{U}_h$ is the vertically averaged horizontal velocity, P is the precipitation, E evaporation, R runoff, and I is the ice melt flux. Finally, there is a continuity of pressure across the sea surface interface.

The friction (also known as surface stress) between the ocean or ice and atmosphere is defined as the downward flux of horizontal momentum. This is represented as values outside of the logarithmic turbulent boundary layer as this layer is assumed to be $\sim 1m$, a length which is much smaller than the smallest grid size.

Ocean Bathymetry Boundary

The ocean floor exchanges no heat or salt with the ocean. The normal velocity component in grid cells adjacent to boundaries are set to zero, giving only a velocity which is parallel to the boundary. The ocean floor and coastlines can however exchange momentum with the ocean. This leads to a friction parameterization as grid cells are too large to resolve these physics. In this thesis, friction is defined in terms of modifying the turbulent fluxes using bottom and lateral boundary conditions. This is termed a non-linear quadratic boundary friction and a free-slip lateral boundary condition.

The coastline exchanges no heat but injects freshwater into the ocean to simulate runoff. All runoff is assumed to be fresh ($0psu$) and is evenly distributed though the depth of the river, this value

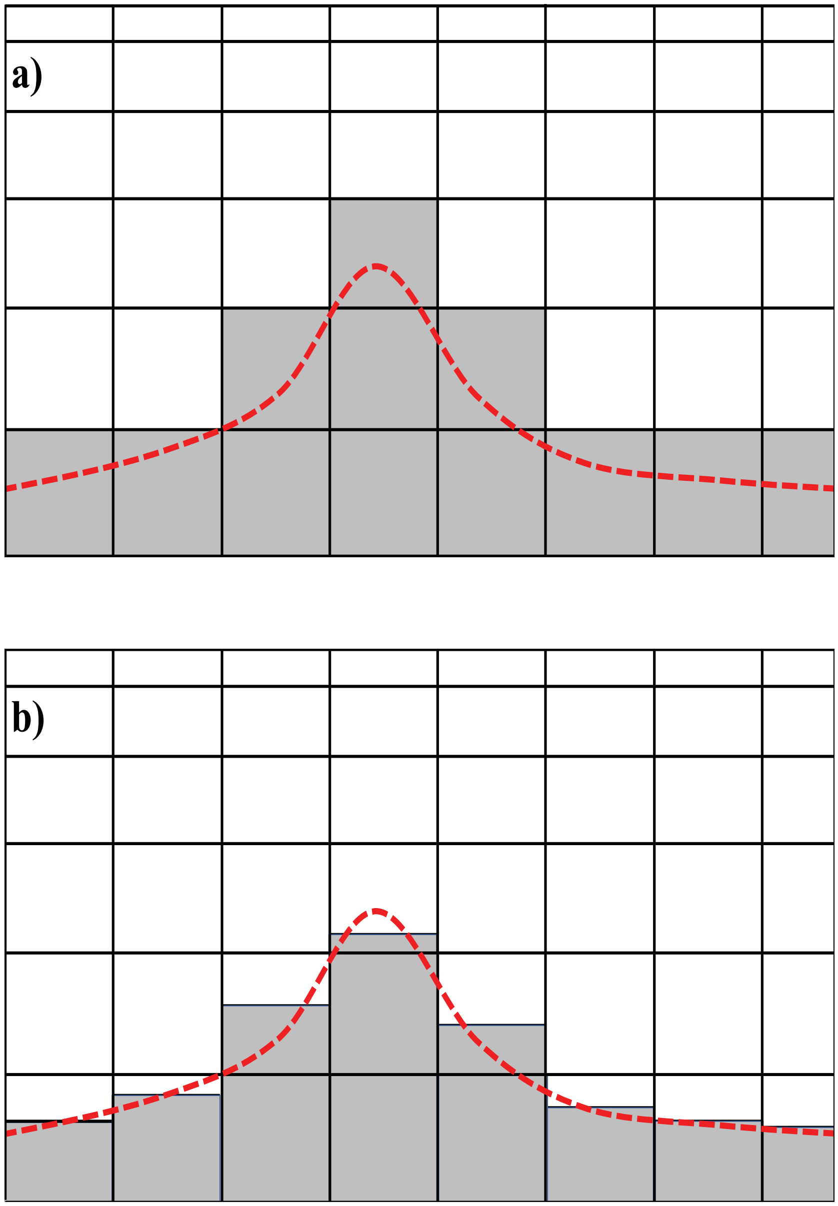

Figure 2.1: Partial Cell Schematic. Based on Figure 4.5 in Madec (2008) a) z-coordinates with a full-step to represent topography b) z-coordinates with a partial-step to represent topography

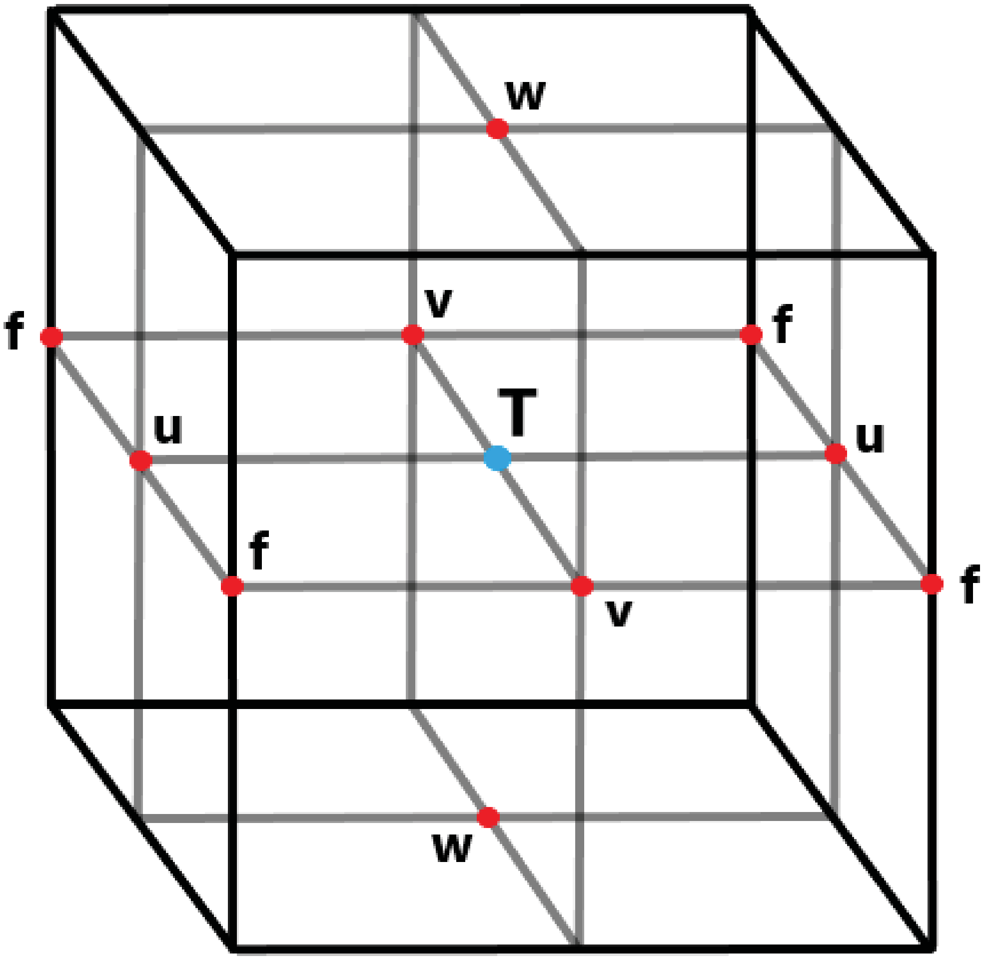

Figure 2.2: Arakawa's C Grid. Based on Figure 4.1 in Madec (2008)

is a specified input. As the linear free surface condition require a constant ocean volume, runoff is represented as a salt flux, i.e. the ocean is diluted of salt where runoff is present.

2.1.5 Time Domain

NEMO stores three arrays for the purpose of time-stepping. These can be defined as before, during, and after and represent the time-step previous to the current, the current time-step, and subsequent time-step.

$$x^{t+\Delta t} = x^{t-\Delta t} + 2\Delta t RHS_x^{t-\Delta t, t, t+\Delta t} \tag{2.11}$$

RHS corresponds to the right-hand-side an equation and x can be any scalar vector (T, S, u, or v) and ΔT is the time-step. Time stepping is performed in a single operation to avoid instabilities.

Non-diffusive processes (momentum, tracer advection, pressure gradient, and Coriolis) are marched in time using the Leapfrog scheme of Mesinger and Arakawa (1976):

$$x^{t+\Delta t} = x^{t-\Delta t} + 2\Delta t RHS^t \tag{2.12}$$

This scheme is centered in space and the achieves second-order accuracy. However, it is not suitable for diffusive processes due to a large-phase speed error. The Robert-Asselin filter (Asselin (1972), Robert (1966)) is used to prevent a possible dispersion of odd and even time-steps due to the third-order dispersive error:

$$x_F^t = x^t + \gamma[x_F^{t-\Delta t} - 2x^t + x^{t+\Delta t}] \tag{2.13}$$

here the subscript F values are filtered values and γ is the Asselin coefficient which is set to 0.1.

For diffusive processes (horizontal diffusion or tracer restoring) a forward difference scheme is used:

$$x^{t+\Delta t} = x^{t-\Delta t} + 2\Delta t D_x^{t-\Delta t} \tag{2.14}$$

here D_x denotes a diffusive term. This scheme is conditionally stable for horizontal tracer and momentum diffusion (Griffies, 2004):

$$A^h = \begin{cases} \frac{e^2}{8\Delta t} & \text{Laplacian Diffusion} \\ \frac{e^4}{64\Delta t} & \text{Bilaplacian Diffusion} \end{cases} \tag{2.15}$$

here, A^h is the mixing coefficient and e is the largest horizontal grid size. At a $1/4°$ resolution (used in this thesis) the time-step is $1080s$ and the largest grid size is $27,779.7m$. These values provide a bounds for Laplacian and Bilaplacian diffusion.

For vertical diffusion the unconditionally stable but diffusive, implicit, backward difference, time-stepping scheme is used:

$$x^{t+\Delta t} = x^{t-\Delta t} + 2\Delta t RHS_x^{t+\Delta t} \tag{2.16}$$

2.1.6 Parameterizations

There are several parameterizations in NEMO to account for physics which occur at scales that the finite grid sizes and and time steps cannot resolve. Parameterizing turbulent motion is critical for accurately modeling large scale motions. Turbulence parameterizations assume that turbulent fluxes are dependent on large-scale quantity gradients. The vertical component of the turbulent fluxes of momentum, heat and, salinity are:

$$D_v^U = \frac{\partial}{\partial z}(A_v^m \frac{\partial U_h}{\partial z}) \tag{2.17}$$

$$D_v^T = \frac{\partial}{\partial z}(A_v^T \frac{\partial T}{\partial z}) \tag{2.18}$$

$$D_v^S = \frac{\partial}{\partial z}(A_v^T \frac{\partial S}{\partial z}) \tag{2.19}$$

where $A_v^m = 1 \times 10^{-4} m^2 s^{-1}$ and $A_v^T = 1 \times 10^{-5} m^2 s^{-1}$ are the vertical eddy viscosity and diffusivity coefficients for non-turbulent conditions, respectively. In turbulent conditions the eddy viscosity and diffusivity coefficients are calculated using a turbulent kinetic energy (TKE) turbulence closure scheme. The closure scheme is:

$$TKE = \bar{e} = \frac{1}{2}(\overline{u'^2} + \overline{v'^2} + \overline{w'^2}) \tag{2.20}$$

$$\frac{\partial \bar{e}}{\partial t} = \frac{A_v^m}{e_3^2}[(\frac{\partial u}{\partial k})^2 + (\frac{\partial v}{\partial k})^2] - A_v^T N^2 + \frac{1}{e_3}\frac{\partial}{\partial k}[\frac{A_v^m}{e_3}\frac{\partial \bar{e}}{\partial k} - c_\varepsilon \frac{e^{-\frac{3}{2}}}{l_\varepsilon} \tag{2.21}$$

$$A_v^m = c_k l_k \sqrt{\bar{e}} \tag{2.22}$$

$$A_v^T = \frac{A_v^m}{P_{rt}} \tag{2.23}$$

where TKE is composed of the turbulent components of each velocity, k is the vertical index, $N = \sqrt{-\frac{g}{\rho_0}\frac{d\bar{\rho}}{dz}}$ is the Brunt-Väisälä frequency, and $P_{rt} = \frac{\nu}{\alpha}$ is the Prandtl number, $c_k = 0.1$ and $c_\varepsilon = \frac{\sqrt{2}}{2}$. Here the time evolution of TKE (left-hand side) is governed by the three terms on the right of 2.21: production through vertical shear, destruction through stratification, and vertical diffusion. The dissipation length scales are further defined as:

$$l_k = l_\varepsilon = \frac{\sqrt{2\bar{e}}}{N} \tag{2.24}$$

$$\frac{1}{e_3}|\frac{\partial l}{\partial k}| \leq 1 \tag{2.25}$$

This closure scheme works to restore static stability in the fluid column by increasing the vertical eddy diffusivity when stratification becomes unstable.

Along isopycnals (horizontal) the turbulent flux is composed of Laplacian operator ($\nabla \cdot \nabla$):

$$\nabla \cdot (A_l \mathbf{R} \nabla T) \tag{2.26}$$

$$\mathbf{R} = \begin{pmatrix} 1 & 0 & -r_1 \\ 0 & 1 & -r_2 \\ -r_1 & -r_2 & r_1^2 + r_2^2 \end{pmatrix} \tag{2.27}$$

here, T can be any tracer, $r_{1,2}$ are the slopes of the isopycnals. The horizontal diffusion equation can be further reduced to:

$$D_l^T = \frac{1}{e_1 e_2}[\frac{\partial}{\partial i}(\frac{e_2}{e_1}A_l^T \frac{\partial T}{\partial i}|_z)|_z + \frac{\partial}{\partial j}(\frac{e_1}{e_2}A_l^T \frac{\partial T}{\partial j}|_z)|_z] \tag{2.28}$$

Momentum diffusion to the second-order can then be defined in terms of relative vorticity (ζ) and flow divergence (χ).

$$D_l^U = \nabla_h(A_l^m \chi) + \nabla_h \times (A_l^m \zeta \mathbf{k}) \tag{2.29}$$

It should be noted that a fourth-order operator (bilaplacian) for momentum diffusion is used which is the same as applying this second-order operator twice.

2.2 LIM3 Sea Ice Model

To simulate sea ice, this thesis uses the Louvain-la-Neuve sea ice model (LIM3; Rousset et al. (2015), Vancoppenolle et al. (2009)). LIM3 is a C-grid dynamic-thermodynamic sea ice model designed for climate studies and operational oceanography. This model includes thickness, enthalpy, salinity, and age distributions. A series of ice thickness categories are used to represent a heterogeneous ice pack. In LIM3, sea ice levitates above the ocean surface though does exert a pressure on the ocean surface (Rousset et al. (2015); Figure 3.1).

2.2.1 Ice Thickness Distribution Theory

Ice thickness can vary by several meters over small spatial scales (e.g., Wadhams et al. (2011)). A given region of the ice pack could contain open water, thick, ridged ice or newly formed thin ice. Model grid cells are typically too large to resolve these thickness variations. To more accurately account for sub-grid scale sea ice thickness variations, Thorndike et al. (1975) introduced the ice thickness distribution (ITD). Thorndike et al. (1975) propsed the use of several thickness categories in each model grid cell to represent different concentrations and volumes of ice thickness. In this formulation the dimensionless function $g(h)$ represents sub-grid scale variations in ice thickness (h):

$$\int_{h_1}^{h_2} g(t,\mathbf{x},h)dh = \frac{1}{R}A(h_1,h_2) \tag{2.30}$$

where $g(t,\mathbf{x},h)dh$ represents the relative area covered by sea ice with a thickness that is between h_1 and h_2 in a grid cell with area R, at time t in a region R centered at $\mathbf{x}$. h_1 and h_2 are determined by the number of ice thickness categories. $A(h_1,h_2)$ is the area in R covered by sea ice with thickness between h_1 and h_2. R is considered to be a length scale which is large compared to ice thickness changes.

When assuming that $g(h)$ is continuous, the conservation of ice area can be written as:

$$\frac{\partial g}{\partial t} = -\nabla \cdot (g\mathbf{u}) - \frac{\partial}{\partial h}(fg) + \psi \tag{2.31}$$

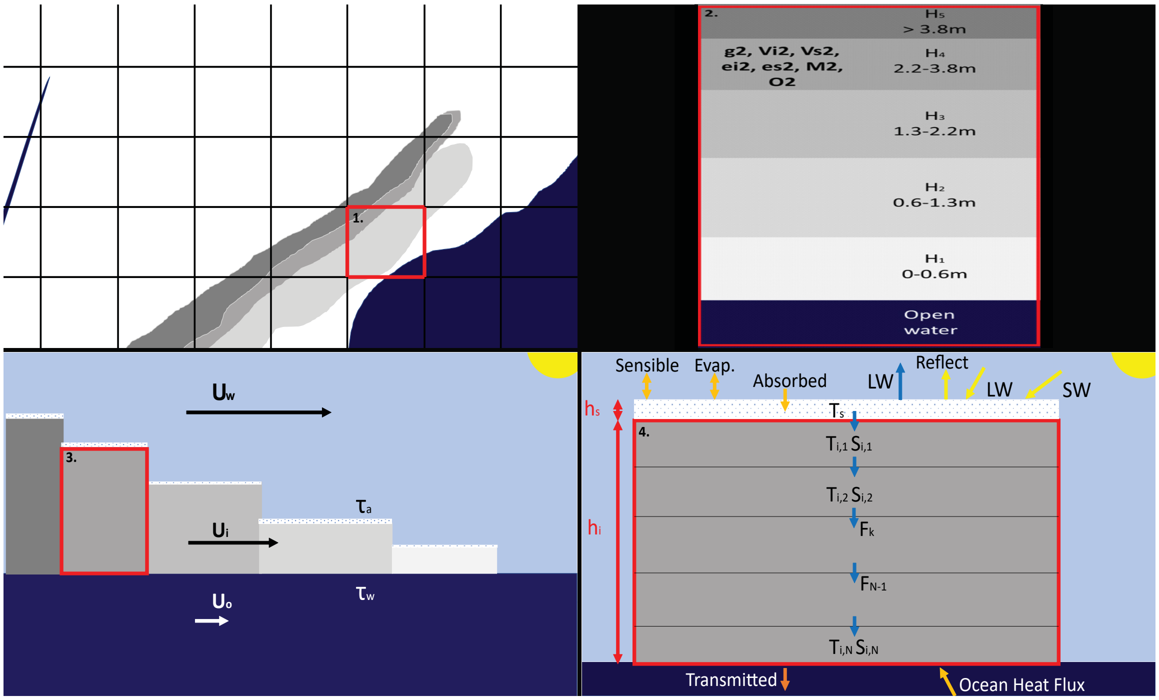

Figure 2.3: Schematic describing the ice thickness distribution in LIM3

Hence, the change in thickness over time is equal to the three terms on the right hand side; horizontal transport by the velocity field, advection in thickness space by thermodynamics (f), and mechanical redistribution (ridging and rafting), respectively. Horizontal transport $-\nabla(g\mathbf{u})$ is dependent on the two dimensional ice velocity vector. f is the thermodynamic growth rate, and ψ is the mechanical redistribution function which depends on the strain rate tensor.

LIM3 discretizes the ice thickness distribution into several categories and solves g over the ocean domain. The numerical formulation of thickness categories follows Bitz et al. (2001) and Lipscomb (2001). Boundaries between ice thickness categories are selected to produce a greater resolution for thin ice (Figure 3.1b). In this thesis, 5 discrete thickness layers (M) are used. Each layer is defined such that the mean thickness h_m^i of each layer is constrained to be; $H_{m-1} < h_m^i < H_m$, where H_0 is open water.

Each thickness category has its own set of global state variables; ice concentration (g_m^i), ice volume per unit area (v_m^i), ice enthalpy per unit area ($e_{m,k}^i, k = 1, 2, ..., N$), ice salt content ($M_m^s$), ice age content ($O_m$), snow enthalpy per unit area (e_m^s), and snow volume per unit area (v_m^s). State variables all follow an equation of the form of 2.31. Velocity is also an extensive variable in LIM3, though only one velocity is given for all thickness categories in a given grid cell (Figure 3.1c). Thickness categories are further divided into N vertically uniform layers of ice and one snow layer for thermodynamic calculations (Figure 3.1d).

2.2.2 Thermodynamics

Thermodynamics cover a range of processes associated with ice energy changes. These include storage or transmission of energy and lead to ice growth or melt. LIM3 thermodynamics include; creation of new ice in open water, basal ice growth, ice melt at the atmosphere and ocean interfaces, snow-ice formation, brine drainage, and ice ageing. Thermodynamic calculations are made at each grid cell and for each thickness category. Instead of using the extensive variables discussed above, thermodynamic calculations use equivalent (intensive) state variables; ice thickness (h^i_m), snow depth (h^s_m), ice specific energy of melting ($q^i_{m,k}$), snow specific energy of melting (q^s_m), ice temperature ($T^i_{m,k}$), snow temperature (T^s_m), ice salinity (S^i_m), and ice age (o^i_m). All thermodynamic processes are assumed to be purely vertical and follow Bitz and Lipscomb (1999).

Once all thermodynamics are calculated, state variables are transported in thickness space due to ice growth or melt. This is done by the linear remapping scheme of Lipscomb (2001). In LIM3 there is no lateral melting, though there is some semblance of this process due to the enhanced melting of thin ice (Bitz et al., 2001). Halodynamics occur after thermodynamic calculations are made.

Vertical Growth and Melt

Heat storage in sea ice is governed by a 1-dimensional heat diffusion equation. This is used to determine rates of melt or growth in subsequent steps. Each thickness category ice is divided into N uniform layers of ice and one snow layer to iteratively solve the heat diffusion equation (Figure 3.1). Each layer has its own temperature, salinity, and thermal conductivity to simulate the storage and propagation of heat through ice with varying salinity. Thus vertical heat transfer and storage are governed by:

$$\rho_i c \frac{\partial T}{\partial t} = -\frac{\partial}{\partial z}(F_c + F_r) \tag{2.32}$$

where ρ_i is ice density, c is the specific heat of the medium (ice or snow), $F_c = k\partial T/\partial z$ is the conductive heat flux, and F_r is the radiation heat flux which is discussed further in the following paragraph. The top interface with the atmosphere is defined by the surface energy balance. The bottom interface with the ocean is defined by the ocean heat flux. At the surface, temperatures above $0°C$ induce melting as the ice/snow surface is fresh, while at the ice-ocean interface follows the UNSECO (United Nations Educational, Scientific and Cultural Organization) formulation to find the freezing temperature based on the ocean surface temperature and salinity.

Imbalances of energy fluxes are used to calculate growth or melt rates. LIM3 thermodynamics are forced with downwelling solar radiation, non-solar heat flux, solid precipitation (snow), and the derivatives of the non-solar and latent heat fluxes which depend on the surface temperature. At the ice/snow-atmosphere surface the heat budget is:

$$F^{net}(T_{su}) = F^{sw}(1-\alpha)(1-i_0) + F^{\downarrow lw} - \varepsilon\sigma T_{su}^4 - F^{sh} - F^{lh} + F_c \tag{2.33}$$

where F_{sw} is the shortwave downwelling radiation, α is the albedo, i_0 is the fraction of solar radiation which penetrates into the ice, $F^{\downarrow lw}$ is the downwelling longwave radiation flux, ε is the surface emissivity, σ is the Stefan-Boltzmann constant, F_{sh} is the turbulent sensible heat flux, F_{lh} is the latent heat flux, finally, F_c is the conductive flux from the ice-snow interior. Surface albedo follows that of Shine and Henderson-Sellers (1985). If the top layer is snow, no radiation enters the snow-ice system. This stems from the simplistic treatment of the snow layer as being of constant density ($\rho_s = 330kgm^{-3}$) and having a constant temperature, zero salinity and only being impacted by precipitation, melt, snow ice formation, or ridging/rafting. If the top surface is ice, radiations is absorbed following Beer's law, $F^r = I_0 e^{-\kappa s}$, with $\kappa_i = 1m^{-1}$. If $F^{net} \geq 0$, there is heat convergence and temperature of the ice surface is fixed at $0°C$ then ablation occurs at the top and bottom interfaces according to:

$$\frac{\partial h_m^{i-}}{\partial t} = \frac{-F_m}{q(S_N, T_N)} \tag{2.34}$$

where q comes from a specific layer calculated by $q(S,T)$ in equation 2.37.

The effects of highly saline water, brine, on heat transfer and storage is included in LIM3. Thus thermal properties are functions of both salinity and temperature. The impacts of brine pockets on simulated sea ice follow Maykut and Untersteiner (1971) and Bitz and Lipscomb (1999). In equation 2.32 ice salinity is included in specific heat term c. Malmgren (1927) give the sea ice specific heat equation as:

$$c_i(S,T) = c_0 + L_0 \mu \frac{S}{T} \tag{2.35}$$

$c_0 = 2067Jkg^{-1}$ and $L_0 = 334kJkg^{-1}$ are the specific and latent heat of fusion of fresh ice, respectively. μ is a constant which relates the temperature at which seawater freezes to its salinity.

Sea ice thermal conductivity follows Pringle et al. (2007):

$$k_i(S,T) = k_0 + \beta_1 \frac{S}{T} - \beta_2 T \tag{2.36}$$

where $k_0 = 0.31WK^{-1}m^{-1}$ is the thermal conductivity of fresh water ice and β_1 and β_2 are constants. The energy required to melt a unit volume sea ice follows Bitz and Lipscomb (1999):

$$q(S,T) = \rho_i c_0(-\mu S - T) + \rho_i L_0 (1 + \frac{\mu S}{T}) + c_w \mu S \tag{2.37}$$

$\rho_i (= 917kg/m^3)$ is the ice density, c_w is the specific heat of seawater. In this formulation saline ice grows more quickly than fresher ice when a heat loss is calculated (Vancoppenolle et al., 2009).

There are three process which form ice; basal growth, new ice formation in open water, and snow ice formation. If heat is lost at the ice base and the ocean temperature is equal to the freezing point of seawater, the salinity of ice forming by basal growth is:

$$S_m^{i,b} = \nu \frac{\partial h_m^{i,b+}}{\partial t} S^w \tag{2.38}$$

where ν is dependent on ice growth (Cox and Weeks, 1988) and S^w is the sea surface salinity (SSS). The basal ice growth rate is then given by:

$$\Delta h^{i,b+} = -\frac{\max[(F^w - F^c|^b), 0]\Delta t}{q(S^b, T^b)} \tag{2.39}$$

where F^w (equation 2.69) is the turbulent ocean heat flux (coming from the ocean model) and $F^c|^b$ is the internal heat conduction flux at the ocean base. The energy q is based on the interface temperature and salinity. If there is instead basal melt equation 2.39 remains similar, though the **max** is switched to **min** and the different between the oceanic turbulent heat flux and the ice conductive heat flux is taken. In the case of melting only the enthalpy of the lowermost thermodynamic layer is looked at.

In cases where the open water ocean surface is at freezing and the surface is losing heat, new ice is formed. Thickness and volume of ice formed by basal growth are given by:

$$\frac{\partial v^{i,0}}{\partial t} = -\frac{F^{ow}}{q(S^0, T0)} \tag{2.40}$$

here F^{ow} is the open water heat loss, S^0, the new ice salinity, is a function of ice thickness which follows Kovacs (1996). New ice thicknesses typically range from $5 - 15cm$ in this formulation. New ice ice then merged into a thickness category (most commonly $m = 1$, the lowest thickness category).

Snow ice forms when snow is thick enough that it increases the overall density of the snow-ice system enough to depress the snow-ice interface beneath the ocean surface (Fichefet and Morales-Maqueda, 1997). Sea water freezes the snow layer and forms snow ice. In LIM3 this process is assumed to occur instantaneously.

At the end of each timestep there is a new ice volume and subsequent thickness for each thickness category, the N number of vertical layer used for thermodynamic calculations in the next timestep must be remapped to ensure that they remain uniform. N uniform layers are required in each thickness layer by the diffusion equation 2.32. This is done by redistributing the enthalpy per unit area on the new, uniform grid. Enthalpies per unit area are the converted to specific enthalpies and then to temperatures.

Halodynamics

Sea ice salinity evolves according to two main processes; brine entrapment and drainage, and sea ice growth or melt. Bulk salinity is defined as S^i_m and $M^s_m = S^i_m v^i_m$ is the sea ice salt content in the mth sea ice thickness category. The equation for bulk salinity evolution closely follows 2.31. Brine entrapment and drainage are a simplification of the VBF07 model (Vancoppenolle et al., 2006). The resulting equation for S^i_m is:

$$\frac{\partial S^i_m}{\partial t} = \frac{\nu S^w - S^i_m}{h^i_m}\frac{\partial h^{i,b+}_m}{\partial t} + \frac{S^{si} - S^i_m}{h^i_m}\frac{\partial h^{i,si}_m}{\partial t} - (\frac{S^i_m - S^G}{T^G})I^G - (\frac{S^i_m - S^F}{T^F})I^F \tag{2.41}$$

Moving from left to right on the right hand side the terms are; brine entrapment during ice growth, snow ice formation, gravity drainage and flushing. T^G and S^G are the winter desalination time scale and equilibrium salinity, the F superscript represents summertime values. Thermodynamic equilibrium is assumed during brine drainage, thus there is a temperature increase which compensates any desalination.

Salinity is assumed to have a vertical distribution S_k^i for thermodynamic calculations. In numerical experiments a linear salinity profile does well to approximate the sea ice salinity profile (Vancoppenolle et al., 2005). To parameterize the differences vertical salinity profile due to ice salinity LIM3 has the profile depend on the bulk salinity of ice. For high salinities, $\overline{S}^i > S_1 = 4.5$, there is a isohaline profile which follows:

$$S_k^i = S_\infty(z_{m,k}) = S^i \tag{2.42}$$

For low salinities, $\overline{S}^i < S_2 = 3.5$ the profile is linear with two constraints; the mean salinity is equal to $\overline{S}^i$ (equal to 2.41) and that the surface salinity is zero. This yields:

$$S_0(z) = 2\frac{\overline{S}^i}{h^i}z \tag{2.43}$$

For intermediate salinities ($3.5 < S_k^i < 4.5$) the profile is a combination of S_0 and S_∞. Thus, the vertical salinity profile, for the three bulk salinity cases is formulated as:

$$S_k^i(z) = \alpha(\overline{S}^i)S_0(z_k) + [1-\alpha(\overline{S}^1)]S_\infty(z_k) \tag{2.44}$$

where α is:

$$\alpha(S_m^i) = \begin{cases} 1 & if\overline{S}^i \leq S_2 \\ (S^i - 4.5)/(S_1 - S_2) & ifS_1 \leq \overline{S}^i \leq S_2 \\ 0 & if\overline{S}^i \geq S_2 \end{cases} \tag{2.45}$$

Vertical Remapping in Thickness Space

From the thermodynamic changes discussed above, there is a new mean thickness for each thickness category at the end of each timestep. The thickness distribution is advected in thickness according to the given rates of growth/melt. Since thickness is an independent variable, other state variables are also transported in thickness space. This is done using the linear remapping scheme of Lipscomb (2001). LIM3 represents this scheme in terms of delta functions following Bitz et al. (2001). There are three steps in this scheme; the displacement of category boundaries, using the displaced categories to estimate the new thickness distribution, and restoring boundaries. The ice growth rate at each thickness category boundary are interpolated. Then the amount of ice displaced in each category is gathered. Finally, using a linear polynomial approximation the boundaries are remapped to the original thickness distribution boundaries.

2.2.3 Dynamics

The ice velocity **u** is determined from the momentum balance:

$$m\frac{\partial u}{\partial t} = A(\tau_a + \tau_w) - mf\mathbf{k} \times \mathbf{u} - mg\nabla \cdot \eta + \nabla \cdot \sigma \tag{2.46}$$

where A is the ice concentration, τ_a and τ_o are the air and water stresses, respectively, m is the mass of snow and ice per unit area. mfk is the Coriolis force, $-mg\nabla\eta$ is the pressure force that arises from sea surface tilt, and $\nabla \cdot \sigma$ arises from internal forces associated with ice deformation. The stress terms are:

$$\tau_o = \rho_o C_o |\mathbf{u}_o - \mathbf{u}_i|(\mathbf{u}_o - \mathbf{u}_i) \tag{2.47}$$

$$\tau_a = \rho_a C_a |\mathbf{u}_a| \mathbf{u}_a \tag{2.48}$$

where $\mathbf{u}$ is the velocity. The subscript i, o, and a denote ice, ocean, and atmosphere variables, respectively. Drag coefficients are $C_o = 0.0055$ and C_a is formed using the CORE bulk formula from Large and Yeager (2004). External stress terms are multiplied by concentration to allow free drift at low concentrations (Connolley et al., 2004). Horizontal transport of ice follows Fichefet and Morales-Maqueda (1997) and uses the advection scheme of Prather (1986).

Ice is considered a two dimensional viscous-plastic continuum which follows Hibler (1979). The stress tensor σ is formulated using the Elastic-Viscous-Plastic (EVP, Hunke and Dukowicz (1997)) on a C-grid (Bouillion et al., 2009). The EVP formulation reduced the viscous-plastic rheology of Hibler (1979) on longer time scales ($\sim$ *days*) and on shorter timescales behaves more elastically (Hunke (2001), Hunke and Dukowicz (1997)). The VP approach assumes that stress is proportional to deformation for small deformations (viscous flow) and stress is independent of deformation above a plastic failure threshold (plastic flow). Hunke and Dukowicz (2002) give a description of the VP and EVP frameworks. Key elements of the ice internal stress tensor are σ_{11}, σ_{22}, and σ_{12}:

$$\sigma_1 = \sigma_{11} + \sigma_{22} \tag{2.49}$$

$$\sigma_2 = \sigma_{11} - \sigma_{22} \tag{2.50}$$

$$D_D = \frac{1}{h_1 h_2}\left(\frac{\partial}{\partial \xi_1}(h_2 u) + \frac{\partial}{\partial \xi_2}(h_1 v)\right) = \dot{\varepsilon}_{11} + \dot{\varepsilon}_{22} \tag{2.51}$$

$$D_T = \frac{1}{h_1 h_2}\left(h_2^2 \frac{\partial}{\partial \xi_1}(u/h_2) - h_1^2 \frac{\partial}{\partial \xi_2}(v/h_1)\right) = \dot{\varepsilon}_{11} - \dot{\varepsilon}_{22} \tag{2.52}$$

$$D_S = \frac{1}{h_1 h_2}\left(h_1^2 \frac{\partial}{\partial \xi_2}(u/h_1) + h_2^2 \frac{\partial}{\partial \xi_1}(v/h_2)\right) = 2\dot{\varepsilon}_{12} \tag{2.53}$$

Where (D_D), (D_T), and (D_S) are the divergence, tension, and shearing strain rates, respectively. ξ_1 and ξ_2 are the generalized orthogonal coordinates, and h_1 and h_2 and scale factors. $\dot{\varepsilon}_{11}, \dot{\varepsilon}_{22}$, and $\dot{\varepsilon}_{12}$ are from the symmetric strain rate tensor (Hunke, 2001). A measure of deformation rate Δ is given by:

$$\Delta = \sqrt{D_D^2 + \frac{1}{e^2}(D_T^2 + D_S^2)} \tag{2.54}$$

The rheology links the compressive stress σ_1, to the shearing stress ($\sigma_s = \sqrt{\sigma_2^2 + 4\sigma_{12}^2}$) by a quadratic relationship:

$$(\sigma_1 + P)^2 + e^2 \sigma_s^2 = P^2 \tag{2.55}$$

Thus, the threshold which defines the boundary between viscous and plastic flow is an ellipse (Hibler, 1979) with an eccentricity $e = 2$. The ice compressive strength is P and e is the eccentricity of the ellipse. The eccentricity of the elliptical yield curve determines the boundary between viscous flow and plastic deformation. Stresses which lie within the yield curve cause ice to move as a viscous fluid, those beyond cause ice to deform as a plastic. Ice compressive strength follows Hibler (1979):

$$P = P^{*}\overline{H}e^{-C(1-A)} \tag{2.56}$$

where P^{*} is an ice strength constant ($20000Nm^{-1}$ and C is an empirical positive parameter (20). $\overline{H}$ is the ice volume in per grid cell, and A is the total concentration and in this case e is now the exponential rather than the eccentricity. Ice strength is smoothed to avoid steep gradients.

On short timescales when sea ice has a greater elastic response, the internal stress tensor follows the EVP formulation of Hunke and Dukowicz (1997):

$$\frac{1}{E}\frac{\partial \sigma_1}{\partial t} = D_D - \frac{\sigma_1 \Delta}{P} - \Delta \tag{2.57}$$

$$\frac{1}{E}\frac{\partial \sigma_2}{\partial t} = D_T - \frac{\sigma_2 e^2 \Delta}{P} \tag{2.58}$$

$$\frac{1}{E}\frac{\partial \sigma_{12}}{\partial t} = \frac{1}{2}D_S - \frac{\sigma_{12} e^2 \Delta}{P} \tag{2.59}$$

Here E is the Young's modulus (or a modulus of elasticity), e is the eccentricity of the elliptical yield curve, and P is the ice strength shown in equation 2.56. In the EVP rheology static flow is represented by an elastic deformation. Again, the EVP rheology of Hunke and Dukowicz (1997) converges to the VP of Hibler (1979) for elastic time scales which are much smaller than that of the external forcing. Therefore, LIM3 uses 300 sub-iterations for sea ice dynamics, giving a time step of $96s$.Using this timescale, the elastic behaviour of ice is more prevalent. At the end of each time step, the stress tensor is saved and used in the following timestep to improve stability and convergence.

Mechanical Redistribution

Dynamical processes create regions of open water or create regions of thicker ice which are dependent on the strain rate tensor and the thickness distribution. LIM3 attempts to resolve processes which thin ice (divergence and shear) and thicken ice (convergence and shear). Mechanical deformation is defined as being either ridging which involves the piling up of smaller pieces into pressure ridges, or rafting, which piles two sheets of ice on one another. Ridging, rafting, or ice opening impact LIM3 state variables in the ψ portion of equation 2.31.

The mechanical redistribution functions follow that described by Thorndike et al. (1975). All redistribution functions ensure a conservation of area which reads:

$$\int_0^{\infty} h\psi dh = \nabla \cdot \mathbf{u} \tag{2.60}$$

The ψ function which governs mechanical redistribution has three main steps; dynamical inputs, participation functions, and transfer functions. In short, the dynamics are either can cause divergence convergence and shear (dynamical input), the ice thickness distribution then determines how much ice can participate in ridging or rafting (participation functions), then ice is transferred in thickness space due to deformation (transfer functions).

A general expression of the mechanical redistribution function associated to the ice concentration is:

$$\psi = |\dot{\varepsilon}|[\alpha_o(\theta)\delta(h) + \alpha_d(\theta)w_d(h,g)] \tag{2.61}$$

The first term on the right hand side corresponds to opening and the second term corresponds to deformation. $|\dot{\varepsilon}| = (\dot{\varepsilon}_1^2 + \dot{\varepsilon}_2)^2)^{1/2}$, where $\dot{\varepsilon}_1 = \nabla \cdot \mathbf{u}$. $\dot{\varepsilon}_2$ are the strain rate tensor invariants and $\theta = \arctan(\dot{\varepsilon}_2/\dot{\varepsilon}_{1)}$.

There are two dynamical inputs in to the mechanical redistribution functions; $|\dot{\varepsilon}|\alpha_o$, the net opening rate and $|\dot{\varepsilon}|\alpha_d$, the net closing rate. These two inputs satisfy the conservation relationship; $|\dot{\varepsilon}|\alpha_o - |\dot{\varepsilon}|\alpha_d = \nabla \cdot \mathbf{u}$.

To differentiate between ridging and rafting there are two deformation modes w^{ri} and w^{ra}:

$$w^d(g,h) = w^{ri}(g,h) + w^{ra}(g,h) \tag{2.62}$$

Ridging involves the formation of pressure ridges which are composed of broken pieces of ice. This process results in the participating ice being pushed into various thicknesses. During the ridging process volume is not conserved as there is a prescribed porosity ($p = 30\%$) which follows observations of Høoyland (2002) and Leppäranta et al. (1995). This is done to include the volume of seawater which is trapped during the ridge forming process. Thus, ridges have a greater volume than the participating ice and volume is not conserved for this process. Rafting is the process which piles two sheets of ice on top of one another. This results in a doubling of ice thickness in participating ice and all volume is conserved. Deformation modes are composed of participation and transfer functions each of which contain contributions from ridging and rafting.

It is assumed participation functions do not depend on whether the ice is ridging or rafting. Thus:

$$b^{ra}(h) = \beta(h)b(h) \tag{2.63}$$

$$b^{ri}(h) = [1 - \beta(h)]b(h) \tag{2.64}$$

where b(h) is an exponential weighting function which preferentially includes the thinnest ice available (Lipscomb et al., 2007):

$$b(h) = \frac{exp[-G(h)/a^*]}{a^*[1 - exp(-1/a^*)]} \tag{2.65}$$

$a*$ is an e-folding scale. The Lipscomb et al. (2007) version of the participation function is numerically more stable than that of Thorndike et al. (1975). $\beta(h)$ follows Haapala (2000) in that it partitions between ice which ridges or rafts. Following the Parmerter (1975) law which states that under a critical ice thickness h_P ice rafts, when ice is thicker it ridges. And $\beta(h) is : \beta(h) = \frac{tanh[-C_{ra}(h-h_P)]+1}{2}$(2.66)where $C_{ra} = 5m^{-1}$ and $h_P = 0.75m$ which follows (Haapala (2000), Babko et al. (2002)). Thus, ice participating in redistribution below the critical thickness of $0.75m$ participates in rafting, all ice with a greater thickness ridges. The *tanh* function is present to smooth the transition between ridging and rafting.

Transfer functions describe how ice thickness changes once the participating ice is selected. The more simple rafting transfer function results in a doubling of ice thickness:

$$n^{ra}(h) = \frac{1}{2}\int_0^\infty \delta(h-2h')b(h')g(h')dh \tag{2.67}$$

here δ is the Dirac delta function. The ridging transfer function is:

$$n^{ri}(h) = \int_0^\infty \gamma(h',h)(1+p)b(h')g(h')dh \tag{2.68}$$

where $\gamma(h,h')$ is a redistributor which determines how an area of thickness h' is redistributed onto an area of thickness h. Ice participating in ridging in linearly distributed between a thickness $2h'$ and $2\sqrt{H^*h'}$, where $H^* = 100m$ (Hibler, 1980). This is used in the ψ ice volume redistribution function 2.31.

Other global state variables are computed based on the redistribution of concentration and volume. A fraction of snow enthalpy and volume (50%) is lost during ridging or rafting and transferred to the ocean. The sea water which is included in ridge building is subsequently included in ice enthalpy and salt content calculations.

2.2.4 Ice-Ocean Coupling

LIM3 must be coupled to ocean as there are constant exchanges of momentum, heat, water, and salt. Coupling follows Goosse and Fichefet (1999). LIM3 is coupled to the ocean model at every timestep. The ice and ocean exchange momentum through the ice-ocean stress (τ_w; equation 2.46) which derives from a quadratic bulk formula (equation 2.47 with an oceanic drag coefficient of $C_w = 5.0 \times 10^{-3}$. The ice-ocean stress is used in equation 2.46. The oceanic heat flux is a function of of the ocean temperature and turbulent mixing (Goosse and Fichefet, 1999):

$$F_w = \rho_w c_w C_h u^*_{io}(T^w - T^{ml}) \tag{2.69}$$

where c_w is the seawater specific heat, $C_h = 0.006$ is a heat transfer coefficient (McPhee, 1992), T^{ml} is the mixed layer temperature, and u^*_{io} is a friction velocity which is a function of the difference between the ice and ocean velocities.

Freshwater fluxes use the approach of Tartinville et al. (2001). Adaptions are made to account for time varying salinity. Following Tartinville et al. (2001) when liquid or solid water is exchanged in the ice-ocean (e.g. precipitatio or evaporation) system it is introduced as a freshwater flux. Additionally, if a surface process impacts ocean salinity without a gain or loss of water (e.g. melting or freezing), the internal exchange is represented as an equivalent salt flux applied to the ocean. Here sea ice acts as a negative reservoir of salt. Ice formation releases salt into the ocean, while melt takes salt out. The surface freshwater flux is:

$$F^f = P - E - \rho_s \sum_{m=1}^{M} \frac{\partial v_m^{s,-}}{\partial t} \tag{2.70}$$

where P is the precipitation, E evaporation, and $\frac{\partial v_m^{s,-}}{\partial t}$ is the snow volume loss due to melt and snow ice formation.

The salt flux is then:

$$F^s = F^s_b + F^s_{eq} \tag{2.71}$$

which is a function of brine drainage (F^s_b) and an equivalent flux due to ice growth and melt (F^s_{eq}).

2.3 LIM2 Sea Ice Model

LIM2 (Fichefet and Morales-Maqueda, 1997) is the predecessor to LIM3 sea ice model (Rousset et al., 2015; Vancoppenolle et al., 2009) and thus many of the components are similar. However, LIM2 does not include multiple ice thickness categories, mechanical redistribution, salinity variations or halo-thermodynamics. Thus, LIM2 includes a single ice thickness category, thickness varies only due to thermodynamic growth, and thermodynamics are only dependent on ice temperature. Ice growth takes up salt from the ocean and does not release any of this mass back into the ocean as ice ages. The ice-ocean-atmosphere stress formulations are the same as in LIM3, as well as, the EVP rheology of Hunke and Dukowicz (1997). Further, the surface albedo parameterization remains the same, using that of Shine and Henderson-Sellers (1985).

As salinity is not included in thermodynamics, the heat storage equation is instead:

$$\rho C_p \frac{\partial T}{\partial t} = Gk \frac{\partial^2 T}{\partial z^2} \tag{2.72}$$

where, density, ρ, thermal conductivity, k, specific heat C_p, are specified for ice and snow. G is a correction factors to accounts for different heat conduction as ice thickness varies. Unlike LIM3 which uses multiple thermodynamic layers, LIM2 only uses a single thermodynamic layer to solve the for heat storage in the sea ice system.

To make up for a lack of thickness resolution, LIM2 includes lateral growth and decay to represent sub-grid scale ice concentration variations:

$$\frac{\partial A}{\partial t} = (1 - A^2)^{1/2} \frac{(1 - A)B_l}{L_i h_o} \tag{2.73}$$

where B_l is the open water heat budget and h$_o$ is the thickness of newly formed ice. When B_l is negative is forms, when is it positive ice melts.

Bibliography

Asselin, R. (1972). Frequency filter for time integration. *Monthly Weather Review*, 100(6):487–490.

Babko, O., Rothrock, D., and Maykut, G. (2002). Role of rafting in the mechanical redistribution of sea ice thickness. *J. Geophy. Res.*, 107:3113.

Bitz, C., Holland, M., Weaver, A., and Eby, M. (2001). Simulating the ice-thickness distribution in a coupled climate model. *J. Geophy. Res.*, 106:2441–2463.

Bitz, C. and Lipscomb, W. (1999). An energy-conserving thermodynamic model of sea ice. *J. Geophys. Res.*, 104:15669–15677.

Bouillion, S., Maqueda, M. M., Fichefet, T., and Legat, V. (2009). An elastic-visous-plastic sea ice model formulated on arakawa b and c grids. *Ocean Modelling*, 27(3-4):174–184.

Connolley, W., Gregor, J., Hunke, E., and McLaren, A. (2004). On the consistent scaling of terms in the sea-ice dynamics equation. *J. Phys. Oceanogr.*, 34:1776–1780.

Cox, G. and Weeks, W. (1988). Numerical simulations of the profile of properties of undeformed first-year sea ice during growth season. *J. Geophy. Res.*, 93:12449–12460.

Fichefet, T. and Morales-Maqueda, M. (1997). Sensitivity of a global sea ice model to the treatment of ice thermodynamics and dynamics. *J. Geophy. Res.*, 102:12609–12646.

Goosse, H. and Fichefet, T. (1999). Importance of ice-ocean interactions for the global ocean circulation: a model study. *J. Geophy. Res.*, 104:23337–23355.

Griffies, S. (2004). *Princeton, N.J. : Princeton University Press.*

Haapala, J. (2000). On the modelling of ice-thickness redistribution. *Journal of Glaciology*, 46(154):427–437.

Hibler, W. (1979). A dynamic-thermodynamic sea ice model. *Journal of Physical Oceanography*, 9:815–846.

Hibler, W. (1980). Modeling a variable thickness sea ice cover. *Monthly Weather Review*, 108:1943–1973.

Høoyland, K. (2002). Consolidation of first-year sea ice ridges. *J. Geophy. Res.*, 107(C6):3062.

Hunke, E. (2001). Viscous-plastic sea ice dynamics with the evp model: Linearization issues. *Journal of Computational Physics*, 170(1):1849–1867.

Hunke, E. and Dukowicz, J. (1997). An elastic-viscous-plastic model for sea ice dynamics. *Journal of Physical Oceanography*, 27:1849–1867.

Hunke, E. and Dukowicz, J. (2002). The elastic-viscous-plastic sea ice dynamics model in general orthogonal curvilinear coordinates on a sphere-incorporation of metric terms. *Monthly Weather Review*, 130:1848–1865.

Kovacs, A. (1996). Sea ice. part 1, bulk salinity versus ice floe thickness. In *Technical Report 96-7*. Cold Regions Research and Engineering Laboratory, Hanover, New Hampshire.

Large, W. and Yeager, S. (2004). Diurnal to decadal global forcing for ocean and sea-ice models: The data sets and flux climatologies. *No. NCAR/TN-460+STR*. University Corporation for Atmospheric Research.

Leppäranta, M., Lensu, M., Koslof, P., and Witch, B. (1995). The life story of a first-year sea ice ridge. *Cold Regions Science and Technology*, 23(3):279–290.

Lipscomb, W. (2001). Remapping the thickness distribution in sea ice models. *J. Geophys. Res.*, 106(C7):13989–14000.

Lipscomb, W., Hunke, E., Maslowski, W., and Jackaci, J. (2007). Ridging, strength, and stability in high-resolution sea ice models. *J. Geophy. Res.*, 112:C0329.

Madec, G. (2008). Nemo ocean engine. *Note du Pole de modélisation*, (27).

Madec, G., Delecluse, P., Imbard, M., and Levy, C. (2008). Opa 8 ocean general ciruclation model - reference model. tech rep., lodyc/ipsl note 11.

Malmgren, F. (1927). On the properties of sea ice in the norwegian north polar expedition with the 'maud'. *Scientific Results*, pages 1–67.

Maykut, G. and Untersteiner, N. (1971). Some results from a time-dependent thermodynamic model of sea ice. *J. Geophy. Res.*, 76:1550–1575.

McPhee, M. (1992). Turbulent heat flux in the upper ocean under sea ice. *J. Geophy. Res.*, 97(C4):5365–5379.

Mesinger, F. and Arakawa, A. (1976). Numerical methods used in atmospheric models. *GARP Publication Series No. 17*, I:64.

Parmerter, R. (1975). A model of simple rafting of sea ice. *J. Geophy. Res.*, 80:198=48–1952.

Prather, M. (1986). Numerical advection by convervation of second-order moments. *J. Geophy. Res.*, 91:6671–6681.

Pringle, D., Eicken, H., Trodahl, H., and Backstrom, L. (2007). Thermal conducitivty of landfast antarctic and arctic sea ice. *J. Geophy. Res.*, 112:C04017.

Robert, A. (1966). The integration of a low order spectral form of the primitive meteorological equations. *Journal of the Meteorological Society of Japan*, 44(5):237–245.

Rousset, C., Vancoppenolle, M., Madec, G., Fichefet, T., Flavoni, S., Barthélemy, A., Benshila, R., Chanut, J., Levy, C., Masson, S., and Vivier, F. (2015). The louvain-la-neuve sea ice model lim3.6: global and regional capabilities. *Geosci. Model Dev.*, 8:2991–3005.

Shine, K. and Henderson-Sellers, A. (1985). The sensitivity of a thermodynamic sea ice model to changes in surface albedo parameterization. *J. Geophy. Res.*, 90:2243–2250.

Stull, R. (1988). *An Introduction to Boundary Layer Meteorology*. Dordrecht: Kluwer Academic Publisher.

Tartinville, B., Campin, J.-M., Fichefet, T., and Goosse, H. (2001). Realistic representation of the surface freshwater flux in an ice-ocean general circulation model. *Ocean Modelling*, 3:95–108.

Thorndike, A., Rothrock, D., Maykut, G., and Colony, R. (1975). The thickness distribution of sea ice. *J. Geophys. Res.*, 80(33):4501–4513.

Vancoppenolle, M., Fichefet, T., and Bitz, C. (2005). On the sensitivity of underformed arctic sea ice to its vertical salinity profile. *Geophy. Res. Let.*, 32:L16502.

Vancoppenolle, M., Fichefet, T., and Bitz, C. (2006). Modeling the salinity profile of undeformed arctic sea ice. *Geophy. Res. Let.*, 33:L21501.

Vancoppenolle, M., Fichefet, T., Goosse, H., Bouillon, S., Madec, G., and Maqueda, M. A. M. (2009). Simulating the mass balance and salinity of arctic and antarctic sea ice. 1. model description and validation. *Ocean Modelling*, 27(1):33–53.

Wadhams, P., Hughes, N., and Rodrigues, J. (2011). Arctic sea ice thickness characteristics in winter 2004 and 2007 from submarine sonar transects. *J. Geophy. Res.*, 116.

Chapter 3

Arctic and northern Baffin Bay sensitivity experiments with the LIM3 sea ice model

Chapter 3 of this thesis is being prepared for publication with the following authorship:

L. Buchart and P.G. Myers. I was responsible for preparing, carrying out experiments, analysis and writing. P.G. Myers provided computational resources and observational datasets as well as provided insight and manuscripts edits.

Abstract

Sensitivity experiments with the Louvain-la-Neuve (LIM3) sea ice model test the sensitivity of ice concentration, ice thickness, and the Nares Strait ice arch to ice density, the inclusion of tidal constituents, the eccentricity of the elliptical yield curve, ice strength, and the number of ice thickness categories. Arctic ice extent is relatively insensitive, except to increasing the number of ice thickness categories from five to eight which lowers the summer minimum extent. Basin averaged ice thickness shows greater sensitivity. Decreasing the eccentricity of the elliptical yield curve increases ice thickness and increasing the ice strength thins Arctic sea ice. LIM2 maintains a greater thickness than any of the sensitivity experiments and does not capture the summer minimum ice extent. The selected parameters do not change the spatial distribution of ice though decreasing the eccentricity of the elliptical yield enhances the ice thickness along the west coast of the Canadian Arctic Archipelago. There is a ~ 0.25 freshening of the top $50m$ of the ocean when using LIM3 compared to the LIM2 Control. Increasing the ice strength further freshens this layer by $0.1 - 0.15$. In the Pikialasorsuaq (North Water Polynya) region, thickness and concentration sensitivities are smaller than Arctic Ocean averages. Experiments compare well to observed concentration in Pikialasorsuaq, though have too much ice in months when the polynya is typically present. Monthly velocities show that decreasing the eccentricity of the elliptical yield curve and increasing the ice strength better simulate the Nares Strait ice arch. Ice volume flux timeseries highlight that LIM2 is not able to produce critical ice arches across the Arctic, whereas through parameter adjustment, the LIM3 model produces ice arches more consistently. Sea ice horizontal divergence is most sensitive to increasing the ice strength and cannot explain ice volume flux sensitivities across the Arctic. Ice density does not impact the ice thickness distribution, decreasing the eccentricity of the elliptical yield curve increases maximum thickness, increasing strength thins ice, decreasing the number of ice thickness categories increases the amount of thin ice, and increasing the number of ice categories has a similar ice thickness distribution to the LIM3 Control.

Changes to sea ice thickness, concentration and circulation, on a variety of timescales ranging from days to years, impact the planetary albedo, as well as the air-sea heat, momentum, mass and gas fluxes. As sea ice is significantly impacted by both ocean circulation (e.g., McGeehan and Maslowski (2012)) and atmospheric circulation (e.g., Comiso (2012)) it is a first-order indicator to changes in the Arctic system. The modelling of these process is a difficult undertaking due to the variety of length and time-scales in which ice responds to atmospheric and oceanic changes. This can lead to a misrepresentation of changes in the sea ice system (e.g., Stroeve et al. (2007)). On smaller scales, the formation of polynyas (regions of open water surrounded by pack ice) in models is difficult as they depend on several processes such as ice growth, ice shear strength, and atmospheric circulation (e.g., Dumont et al. (2009), Yao and Tang (2003)). In recent decades there have been significant losses to sea ice thickness and volume (e.g., Cavelieri and Parkinson (2012)), an increase in ice drift speed (e.g., Kwok et al. (2013)) and a large increase in the amount of open water in the Arctic Ocean. Correct modelling of sea ice is critical to understand and predict future sea ice states and model the evolution of the climate system, as well as to accurately model current sea ice conditions on a variety of scales pertaining to numerous uses, ranging from scientific research, to shipping, to transportation for northern communities.

Sea ice reaches its maximum extent in the late-winter and a minimum in the late-summer. During the summer, sea ice melt releases freshwater to the upper ocean, increasing stratification. In the fall growth season, ice formation takes up freshwater and releases brine into the upper ocean. In general, sea ice thickness is greatest on the west coast of the Canadian Arctic Archipelago (CAA) and to the north of Greenland. This is due to the large scale ocean and atmosphere circulation of the Beaufort Gyre and the subsequent Ekman transport towards the coast (McGeehan and Maslowski, 2012). Thickness is found to decrease towards the Siberian coast (Kwok and Rothrock, 2009). The Beaufort Sea is known as a location where sea ice thickens and ages before recirculating across the Arctic (Howell et al., 2016). Outside the Beaufort Gyre, there is a persistent linear drift of sea ice from the Siberian coast towards Fram Strait, i.e. the Transpolar Drift. The mean ice circulation is comparable to geostrophic currents from satellite dynamic topography (Kwok et al., 2013). In the CAA, narrow channels, an influx of ice from the Arctic Ocean, and a continental climate minimize ice losses in this region, giving the CAA a thicker ice cover than the adjacent Baffin Bay. Northern Baffin Bay and Pikialasorsuaq (also known as the North Water polynya) receive a small amount of ice from the Arctic Ocean via Nares Strait. An ice bridge, composed of thick, multi-year ice (MYI), forms in the fall or winter and persistent northerly winds, latent heat release of warm water, and vertical mixing of warm waters maintain the polynya (Ingram et al. (2002), Dumont et al. (2009), Vincent (2019), Yao and Tang (2003)). In the late spring, the ice arch breaks down, ice flows into northern Baffin Bay, dissolving the polynya.

Many modern sea ice models are based on the pioneering study of Hibler (1979) who used a simple two-layer ice thickness distribution with a viscous-plastic rheology, geostrophic winds and ocean currents to produce ice thickness, concentration, and drift fields which matched the observed well. This model was able to produce key circulation fields of the Beaufort Gyre and the Transpolar

Drift, as well as the thickening of ice to the west of the CAA and north of Greenland. The CORE-(2) set of ocean-ice models analyzed by Wang et al. (2016) found that ocean-ice models showed good agreement with the mean panarctic ice thickness of $2.5 - 3.0m$. These models do well to reproduce the shape of ice between the CAA and Siberia, with thicker ice towards the CAA. However, these models underestimated the rate of ice thinning by a factor of two and have more ice in the southern CAA than was observed. Further, the mean September sea ice extent from these models was $6.17 \times 10^6 km^2$ which was 11% less than that observed.

Other sea ice model studies by Hu and Myers (2014), Hu et al. (2018), and Sou and Flato (2009) all did well to capture the spatial distribution of ice thickness in the CAA. Specifically, Hu and Myers (2014) were able to capture the seasonality of ice thickness in the CAA. The study of Hu et al. (2018) was able to capture the thick ice in the northern CAA, the $2.5 - 3m$ thick ice in Parry and M'Clintock Channel, and thinner ice in the eastern CAA. Sou and Flato (2009) were able to resolve critical polynya across the Canadian Arctic: the North Water in Smith Sound, the Bathurst in Admunsden Gulf, and smaller polynyas in Jones and Lancaster Sounds. However, this model underestimated the amount of ice in Nares Strait. The model of Hu et al. (2018) did well to simulate the motion of ice along the coast of the CAA and the transition of thickness from the Arctic ocean into the CAA. In general, global-scale sea ice models have done well in producing the mean state of ice thickness and concentration, though improvements are necessary.

Sensitivity experiments have been focused on both assessing parameters which are critical to sea ice output and to optimize or tune models. Additionally, sea ice models utilize a range of parameterizations, configurations, and thermodynamics, making knowledge of critical parameters of high importance to ensure consistency of output. Common parameters of interest are ice albedo, density, strength, and more recently, ice thickness categories, and horizontal model resolution. Holland et al. (1993) looked at a range of numerical conditions, parameter values, and physical processes to judge the relative sensitivity of a global sea ice model. Flato and Hibler (1995) ran several sensitivity experiments testing ridge redistribution and shear ridging parameters. Parameters were selected with an emphasis on parameterizations which had not previously been tested and their relative impact on simulated sea ice unknown. Kim et al. (2006) found that ice conductivity, ice-ocean drag, maximum ice salinity, and ridging parameters significantly impact their simulations. Additionally, snow density has a larger impact on winter season output whereas the albedo and emissivity sensitivities dominate in the summer. Recently, Hu et al. (2019) looked at the impact of model resolution on simulated sea ice in the CAA. This study found that model resolution had little impact on the resulting sea ice conditions.

The majority of modern sea ice models have an ice thickness distribution (Thorndike et al., 1975). Enhanced vertical resolution of sea ice helps to resolve processes such as open water ice growth and enhanced melt of thick ice. Vancoppenolle et al. (2009), who described the LIM3 sea ice model, found good agreement in the amount of MYI and first-year ice (FYI) present in the Arctic. This model also had a realistic distribution of ice thickness and concentration though produced a too thick ice pack in the Beaufort Gyre. The LIM3 models was found to have an improved geographical distribution of ice thickness and concentration compared to previous versions of LIM. Dupont et al. (2015), who used a high-resolution sea ice model as part of the Canadian Operational Network of Coupled Environmental PredicTion System developed for short-term ice predictions found solid agreement between observations and the ice thickness distribution, and volume, though the model overestimated ice drift and thickness in the Beaufort Gyre.

Modern sea ice models which use an ice thickness distribution have a greater number of parameters than the previous single-ice-category models. Hunke (2010) tested lesser known parameters, rather than ice albedo, of which sea ice conductivity, mechanical redistribution, and ocean heat flux, ice-ocean dynamic stress, and shortwave radiation produced the greatest sensitivities. Further, a tuned set of parameters were unable to match observed ridged ice thickness and area simultaneously. Moreno-Chamarro et al. (2020) looked at the sensitivity of the number of ice thickness categories. In the Arctic, a single thickness layer shows the worst model-observation agreement, while too many categories also has a poor agreement. However, Massonnet et al. (2019) found that the number of ice categories has an impact on the Arctic winter sea ice volume. Like Hu et al. (2019), Zhang (2020) looked at the impact of resolution on a simulated sea ice, though using a multi-category model. This study found that model resolution does not change key sea ice output though a higher resolution produces more leads.

In an effort to resolve the ice arch which forms the Nares Strait ice bridge, Dumont et al. (2009) modified the eccentricity of the elliptical yield curve to change the ice cohesion and stiffness of the ice moving through the narrow channel of Nares Strait. This study, which used an idealized domain, found a greater cohesion (smaller eccentricity) of ice moving through Nares Strait than was typical for climate scale models was necessary to produce stable ice arches.

The sea ice thickness sensitivity experiments of Hunke (2010) highlight that many modern sea ice models require accurate values of various parameters to represent sea ice, many of which are not bound by physical observations. Further, Mellor and Hakkinen (1994) show that the snow-ice system has the largest sensitivity to surface albedo, once albedo is defined, all other model parameters become critical to accurately representing Arctic sea ice. Hunke (2010) highlighted that tuning the albedo can lead to unknown feedbacks and is not an ideal way to optimize sea ice models. Many modern sensitivity studies have only focused on basin scale sensitivities and modifying larger model components such as the resolution and thickness categories. Judging the impact of key model parameters is a necessary requirement to have a well functioning sea ice model in solid agreement with observations. In this study, we assess the relative impact of variables related to the dynamics and mechanical redistribution parameterizations of the LIM3 sea ice model. Further, we aim to define a set of parameters which generate model output which best matches observed ice concentration and thickness in terms of both mean values, seasonal cycles, and spatial distribution on two different scales, for the Arctic Basin and for northern Baffin Bay. In section 2 we provide a model description and outline the sensitivity experiments, section 3 outlines key results. Results are presented in terms of seasonal cycles and two different case studies: autumn 2016 is used to look at the basin-scale ice sensitivities and April 2015 is used to analyze the Pikialasorsuaq sensitivities.

Autumn 2016 is selected as it represents the general sensitivities found throughout the year. April 2015 is selected to look at Pikialasorsuaq as the polynya is present at this time. Section 4 discusses the relative impact and causes of different sensitivities, finally in section 5 we present key findings and an optimized set of parameters which can be used in future studies.

3.1 Experiment Set-Up and Description

3.1.1 Ocean Model

The ocean model used is the NEMO (Nucleus for European Modelling of the Ocean) numerical framework version 3.6 (Madec, 2008), which is a primitive equation model developed from the Océan PArallélisé (OPA) ocean circulation model version 8.2 (Madec and the NEMO System Team, 2016). Equations of motion are written in curvilinear, orthogonal coordinates (Madec and the NEMO System Team, 2016). Vertical mixing is parameterized using a turbulent kinetic energy closure model and lateral mixing uses a bi-laplacian operator with an eddy viscosity of $1.5 \times 10^{11} m^4 s^{-1}$. A baroclinic timestep of $1080s$ is used. No salinity or temperature restoring is applied.

3.1.2 ANHA

All experiments are run on the Arctic and Northern Hemisphere Atlantic (ANHA) configuration, with a quarter degree resolution (ANHA4). The mesh for ANHA4 is extracted form the $(1/4)^\circ$ global tripolar grid, ORCA25 (Barnier et al., 2007). The ANHA4 configuration yields a horizontal grid resolution of $\sim 12km$ in the Arctic. This configuration covers the Arctic ocean, and north Atlantic, with two open boundaries: one just south of Bering Strait in the north Pacific Ocean and the other at $20^\circ S$ in the Atlantic Ocean. In the vertical, there are 50 non-uniform, levels with layer thickness smoothly varying from $1.05m$ at the surface to $453.15m$ in the bottom layer.

3.1.3 Sea Ice Model

The sea ice model used is the C-grid, dynamic-thermodynamic, Louvain-la-Neuve sea ice model (LIM, Fichefet and Morales-Maqueda (1997), Vancoppenolle et al. (2009), Rousset et al. (2015)). Ice is considered a two-dimensional visous-plastic continuum (Hibler, 1979) where the stress tensor, σ is formulated using the Elastic-Viscous-Plastic (EVP) rheology of Hunke and Dukowicz (1997). In the model, sea ice sits on top of the ocean surface. The sea ice model is coupled to the ocean model at every timestep. Both the LIM2 (Fichefet and Morales-Maqueda, 1997) and LIM3 (Rousset et al., 2015; Vancoppenolle et al., 2009) versions are used. LIM2 includes one snow and two ice layers. LIM3 includes an ice-thickness distribution which uses a series of ice categories to represent a heterogeneous ice pack. The ice thickness distribution additionally results in a distribution of enthalpy, salinity and ice age. LIM3 parameterizes changes in ice salinity through brine entrapment, drainage, and flushing terms. Ice thermodynamics includes salinity in the ice internal energy calculations. Ice thermodynamics is assumed to take place solely in the vertical. Dynamical processes result in mechanical redistribution of ice thickness through ridging (piling up of broken ice pieces), rafting (piling of two ice sheets on one another), or opening up the ice pack to reveal open water. Mechanical redistribution functions follow Thorndike et al. (1975). LIM3 exchanges momentum, heat, water, and salt with the ocean model and coupling follows Goosse and Fichefet (1999). Surface albedo follows that of Shine and Henderson-Sellers (1985).

3.1.4 Initial and Boundary Conditions

All experiments are initialized at the start of 2002 and run through 2018. Initial and boundary values of temperature, salinity, horizontal velocity, and sea surface height come from the 0.25° Global Ocean Reanalysis and Simulations (GLORYS2V3) product (Ferry et al., 2008). The inital ice field is a combination of GLORYS2V3 simulation and satellite observations. GLORYS2V3 further provides lateral open boundary conditions at the locations mentioned in the ANHA4 grid description.

3.1.5 External Forcings

Atmospheric forcing ($2m$ temperature and humidity, $10m$ horizontal winds, precipitation, incoming shortwave and longwave radiation) comes from the Canadian Meteorological Centres Global Deterministic Prediction System Reforecasts (GDPS), provided from Environment and Climate Change Canada (Smith et al., 2014). The atmospheric product has a horizontal resolution of $33km$, the temporal resolution is $1hour$.

Greenland runoff comes from Bamber et al. (2012). Liquid discharge extents out to 2010, henceforth the 2010 runoff is repeated out to the end of the study. Arctic river discharge comes from the 1° Global River Flow and Continental Discharge Dataset (Dai and Trenberth (2002), Dai et al. (2009)). This product is volume-conserved, remapped onto the ANHA4 grid. This dataset extents through 2007, subsequent years use a repeated 2007 river discharge.

3.1.6 Sensitivity Experiments

Five different sets of sensitivity experiments were conducted from a single control experiment. There is an emphasis on analyzing the dynamic and mechanical redistribution properties of the sea ice model on the key sea ice output variables. The following paragraph is summarized in Figure 3.1. The five experiments are: 1. tides, nine tidal constituents are included (K1, K2, M2, M4, N2, O1, P1, Q1, and S2) to asses to impact of tidal mixing and velocities. Additionally, many modern ocean models use tides, understanding their role is critical to conduct other sensitivity experiments. The role of tides on modelled sea ice has also found to be substantial, increasing the Baffin Bay ice volume by 8.5% and decreases the CAA ice volume by 17.8% (Kwon and Lee, 2016). Finally, the tides experiment necessitated raising the ice strength constant (experiment 4) to $40000Nm^{-1}$. The LIM2 Control experiment does not include tides, direct comparison with the previous version is not possible when including tides and the LIM3 Control is used for direct comparison with LIM2 2. ice density, sea ice density, considered a constant value ($917kg/m^3$), is raised to $930kg/m^3$ and lowered

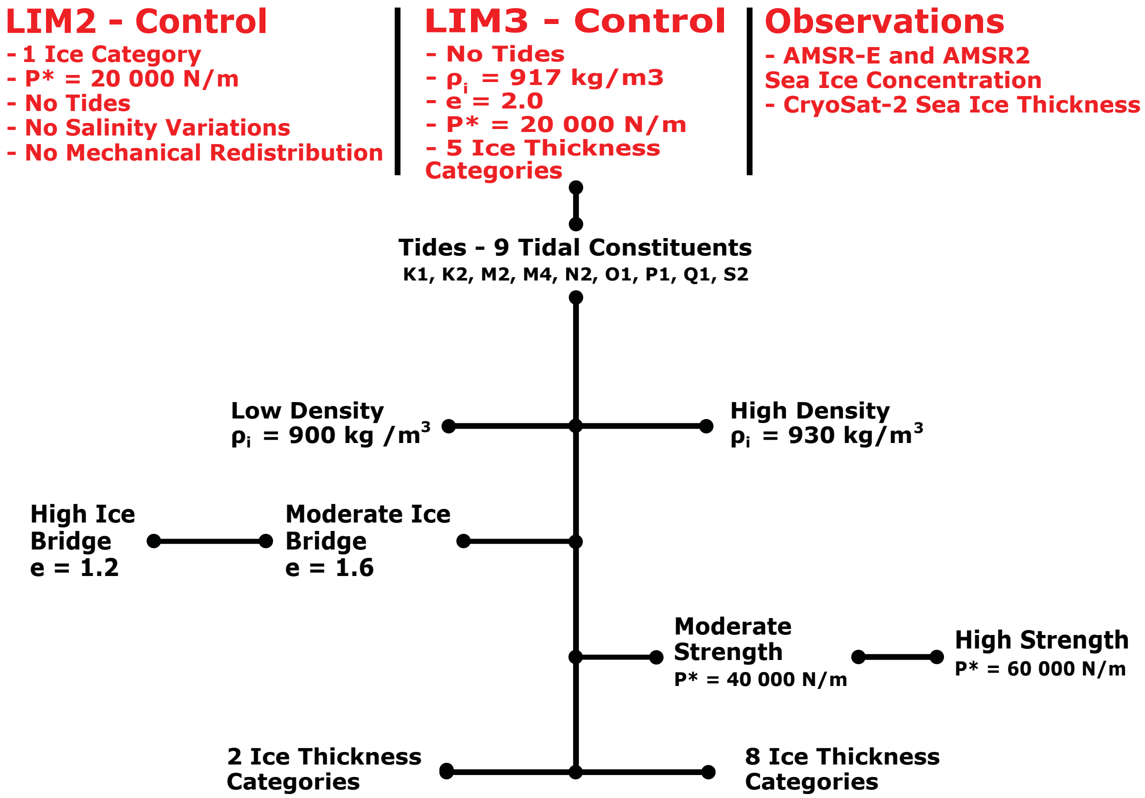

Figure 3.1: Schematic outlining the sensitivity experiments. Bolded names indicate each sensitivity experiment name.

to $900 kg/m^3$. Ice density is modified to asses to relative impact of winds and ocean currents on sea ice, specifically ice motion. These values follow the experiment of Hunke (2010) which looks at the sensitivity of sea ice model parameters in the CICE sea ice model. 3. ice shear strength and stiffness, the eccentricity of the elliptical yield curve was twice lowered from a control value of 2.0 to 1.6 and 1.2. This experiment follows that of Dumont et al. (2009) and aims to look at the ability of LIM3 to resolve ice arches in the Canadian Arctic Archipelago, particularly the Nares Strait ice bridge. 4. Ice compressive strength, the ice strength constant which determines ice strength ($P = P^{*}He^{-C(1-A)}$) is raised from a control value of $20000 Nm^{-1}$ to $40000 Nm^{-1}$ and $60000 Nm^{-1}$. This experiment raises the ice compressive strength towards the satellite range of Tremblay and Hakkinen (2007) ($30000 - 45000 Nm^{-1}$) and then further increases compressive strength to gain insight on decreases in ridging and rafting with a stronger ice pack, 5. Ice thickness categories, the control run uses five thickness categories, experiments have 2 and 8 thickness categories to analyze the impact the resolving or not resolving different ice thickness categories. Outcomes of this experiment include the importance of thin ice on mechanical redistribution, enhanced growth of thin ice, and resolving the thick ridged ice to the west of the Canadian Arctic Archipelago. In addition to the control experiment, an experiment using the previous version LIM2 is also run (one ice category, no ice salinity variations or mechanical redistribution) to gauge the improvements of LIM3 and to further aid in tuning of the model.

3.1.7 Observational Datasets

AMSR-E and AMSR2 Sea Ice Concentration

Arctic sea ice concentration values come from the AMSR-E and AMSR2 (henceforth AMSR) satellite products and the ASI sea ice concentration algorithm (Spreen et al. (2008), Melsheimer and Spreen (2019), Melsheimer and Spreen (2020)). AMSR-E observations extend from 2002-2011 and AMSR2 extends from 2012 to the present. Reprocessed data has a horizontal resolution of $6.25 km$ and a temporal resolution of one day. Measurements are taken year-round.

CryoSat-2 Sea Ice Thickness

Arctic sea ice thickness is from the National Snow and Ice Data Center CryoSat-2 Level-4 sea ice elevation, freeboard, and thickness, Version 1 (Kurtz and Harbeck, 2017, https://nsidc.org/data/RDEFT4/). Measurements extend from September 2011 to the present. The horizontal resolution is $25 km$, the temporal resolution is monthly. CryoSat-2 thickness is projected a polar stereographic SSM/I Grid and references to the WGS-84 ellipsoid. The CryoSat-2 domain covers regions north of the Canadian Arctic Archipelago, Bering Strait, and regions north of Fram Strait and the Barents Sea Opening. CryoSat-2 measurements are taken from January to May and September to December of each year.

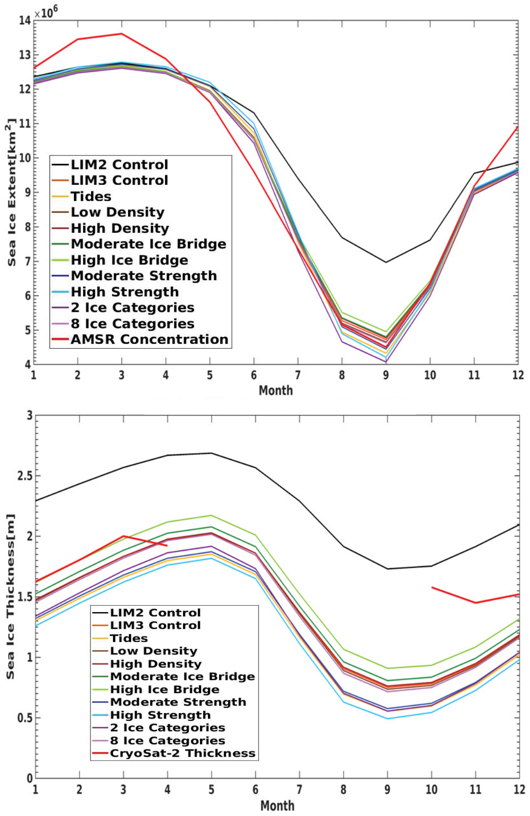

Figure 3.2: Panarctic sea ice a) concentration and b) thickness seasonal cycles averaged from 2014-2018.

3.2 Results

3.2.1 PanArctic

Arctic Ocean sea ice extent (extent does not include ice south of Bering Strait in the North Pacific on the ANHA4 domain) is relatively insensitive to the sensitivity experiments. Here, sea ice extent is defined as the areal coverage of ice with a concentration greater than 15%. The LIM3 Control reaches a maximum extent in March of $12.3 \times 10^6 km^2$ and reaches minimum extent of $5.1 \times 10^6 km^2$ in September. Trimming AMSR2 domain to match the ANHA4, the AMSR2 maximum also occurs in March, though is $14.6 \times 10^6 km^2$. The minimum observed ice extent is $4.8 \times 10^6 km^2$ in September. The LIM3 Control closely follows the autmn and winter sea ice extent growth, though has too little ice in the late-winter and early spring and too much ice from May to July. The LIM2 Control does not show same seasonal cycle as the LIM3 Control. The LIM2 Control has a similar winter and spring maximum extent period, though only reaches a minimum of $7.2 \times 10^6 km^2$ in September. A difference of $2.5 \times 10^6 km^2$ compared to the LIM3 Control. The LIM2 Control maintains a greater extent than the LIM3 Control from June to December. From January to April and October to December, sensitivity experiment sea ice extent does not change by more than $0.3 \times$

Table 3.1: 2014 - 2018 Annual, regional mean ice concentrations [%]. CAA = Canadian Arctic Archipelago, BB = Baffin Bay, BaS = Barents Sea, GNS = Greenland and Norway Seas

Experiment	Central Arctic	CAA	BB	BaS	GNS
LIM2 Control	85.1	82.2	55.9	31.3	15.9
LIM3 Control	81.7	82.0	56.8	29.8	12.7
Tides	80.8	81.2	55.2	31.0	11.8
Low Density	81.5	81.9	57.2	29.8	12.6
High Density	81.7	82.1	56.9	29.8	12.9
Moderate Ice Bridge	81.9	81.8	56.6	30.0	12.8
High Ice Bridge	82.3	82.6	57.3	30.6	12.7
Moderate Strength	81.3	82.3	57.7	32.0	12.2
High Strength	80.6	82.4	58.1	33.3	12.4
2 Ice Category	78.2	80.3	56.0	28.5	12.0
8 Ice Category	81.4	81.8	56.7	29.7	12.5
AMSR2	81.5	72.6	52.9	27.7	10.8

$10^6 km^2$. The greatest differences come during the late-summer ice extent minimum, where the High Ice Bridge experiment has a $0.2 \times 10^6 km^2$ greater minimum and the 2 Ice Category experiment has a $1.0 \times 10^6 km^2$ smaller minimum extent. The Tides and Moderate Strength experiments have both the minimum ice extent which best matches observations. These experiments are $\sim 0.2 \times 10^6 km^2$ lower than the LIM3 Control. The 8 Ice Category maintains the lowest summer minimum extent at $4.0 \times 10^6 km^2$, $0.8 \times 10^6 km^2$ lower than the LIM3 Control. The two Ice Bridge experiments act to increase the minimum ice extent by $\sim 0.1 \times 10^6 km^2$ compared to the LIM3 Control. Changing the ice density and increasing the number of ice categories do not change the seasonal cycle of Arctic ice extent.

Annual mean values in sub-regions of the Arctic paint a similar picture, with the LIM2 Control having the highest concentration of ice in the Central Arctic, CAA Barents Sea and in the Greenland-Norwegian Sea region. The LIM2 Control does have the lowest Baffin Bay annual ice concentration, though this is likely due to this experiment having the lowest autumn concentration (not shown). Changing the ice density does not fluctuate the mean concentration by more than 0.2% in any region with the exception of the Barents Sea which has 0.4% more ice. The inclusion of tides lowers ice in all regions by $\sim 1\%$ with the exception coming in the Barents Sea where there is 1.2% more ice. The 2 Ice Category experiment also has $\sim 1\%$ lower ice concentration in all regions. The Moderate and High Ice Bridge experiment is the only experiment which raises concentrations by as much as 1.3% in Baffin Bay, though results in a 0.5% lower Greenland-Norwegian Sea concentration.

Thickness variability is more pronounced (Figure 3.2b). The LIM3 Control reaches a maximum mean thickness of $2m$ in May and a minimum thickness of $0.8m$ in September. The LIM2 Control experiment generally has a $\sim 0.8m$ thicker ice cover than the LIM3 Control. Reaching a maximum thickness in May of $2.7m$ and a minimum thickness of $1.8m$ in September. The LIM2 Control ice thickness is $\approx 0.6m$ greater than the greatest sensitivity experiment, High Ice Bridge. The Moderate Ice Bridge ice cover is $\approx 0.1m$ thicker and High Ice Bridge experiment is $\approx 0.2m$ thicker than the

Table 3.2: 2014 - 2018 Annual, regional mean ice thickness [m]. CAA = Canadian Arctic Archipelago, BB = Baffin Bay, BaS = Barents Sea, GNS = Greenland and Norway Seas

Experiment	Central Arctic	CAA	BB	BaS	GNS
LIM2 Control	2.14	2.24	0.69	0.34	0.36
LIM3 Control	1.35	1.59	0.58	0.25	0.16
Tides	1.17	1.40	0.53	0.25	0.12
Low Density	1.34	1.59	0.59	0.25	0.16
High Density	1.35	1.60	0.59	0.25	0.17
Moderate Ice Bridge	1.41	1.60	0.58	0.26	0.17
High Ice Bridge	1.50	1.64	0.59	0.28	0.17
Moderate Strength	1.29	1.45	0.56	0.26	0.17
High Strength	1.13	1.45	0.56	0.27	0.12
2 Ice Category	1.21	1.50	0.58	0.24	0.14
8 Ice Category	1.33	1.58	0.58	0.25	0.15

LIM3 Control and bring values closer to observations. Changing the ice density and decreasing the number of ice categories do not impact panarctic average, ice thickness. The Moderate Strength, Tides, and 8 Ice Category experiments all have ice that is $0.1m$ thinner than the LIM3 Control. Finally, the High Strength experiment produces a $0.15m$ smaller thickness than the LIM3 Control. When considering the annual average (not shown), thickness sensitivities are even larger.

Sub-regional ice thickness have similar sensitivities to the basin-average. The LIM2 Control has maintains the greatest thickness. The LIM2 Control is $0.79m$ thicker than the LIM3 Control on the Central Arctic and $0.65m$ thicker in the CAA. The High Strength experiment maintains the thinnest ice cover, $0.23m$ thinner than the LIM3 Control in the central Arctic and $0.14m$ thinner in the CAA. The High Ice Bridge experiment has the thickest ice of any LIM3 experiment, $0.15m$ thicker than the LIM3 Control in the central Arctic, and $0.05m$ thicker in the CAA. In Baffin Bay, the Barents Sea and the Greenland-Norway Sea regions sensitivities are smaller as these region have a more seasonal ice cover.

Autumn 2016

Difference plots (Figure 3.3), between observed and modelled sea ice concentration display only small sensitivities in the spatial coverage of ice. Parameter changes do not appear to impact the distribution of ice concentration, only the magnitude of these differences. In general, modelled sea ice compares to observations better in the central Arctic, while the marginal ice zones and coastal regions have greater discrepancies. In autumn 2016, LIM3 sensitivity experiments outperform the LIM2 Control experiment. The LIM3 Control is missing $10-20\%$ of ice compared to the observed ice concentration in the Central Arctic, and has to $10-50\%$ too much ice in the north Atlantic ice edge, central CAA, and along the Beaufort Shelf extending to the Bering Strait region. LIM3 Control northern CAA concentrations compare more favourably to the observed. In the LIM2 Control, regions of 50% too much ice are widespread on the Beaufort Shelf extending across the East Siberian sea. Similar to the LIM3 Control, the LIM2 Control does not have enough ice in Baffin

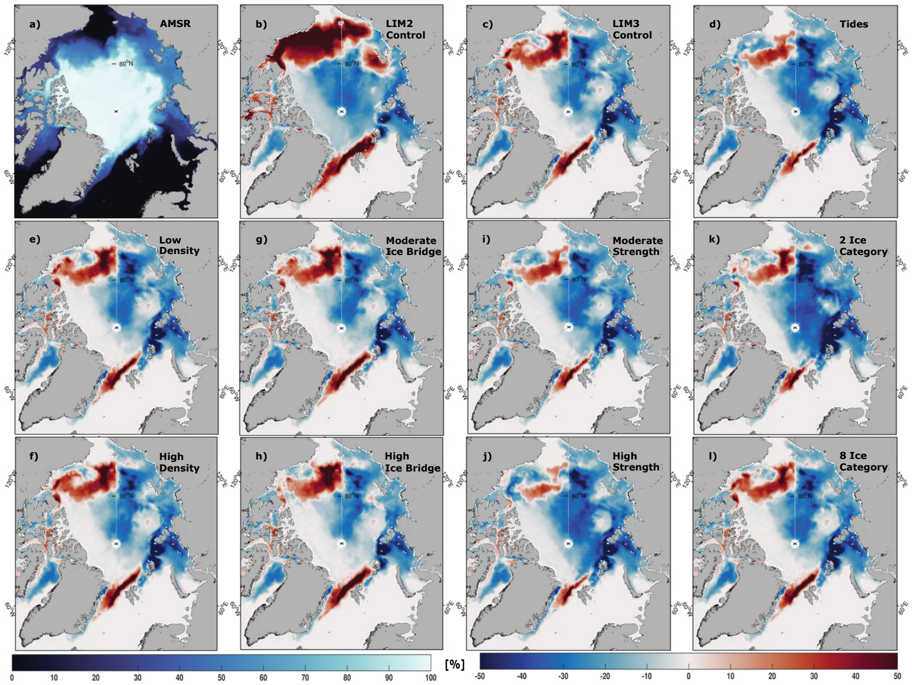

Figure 3.3: Autumn (September-November) 2016, Panarctic sea ice concentration differences. a) Observed AMSR2 concentration b) LIM2 Control c) LIM3 Control d) Tides e) Low Density f) High Density g) Moderate Ice Bridge h) High Ice Bridge i) Moderate Strength j) High Strength k) 2 Ice Category l) 8 Ice Category

Bay, the southern CAA, Kara and Laptev Seas by $10-20\%$. However, the LIM2 Control is lacking $\sim 10\%$ of the ice cover to the west of the CAA, whereas the LIM3 Control compared favorably. Sensitivity experiments are generally similar to the LIM3 Control in their spatial coverage of ice. All LIM3 sensitivity experiments do well to simulate the high concentration of sea ice along the west coast of the CAA and to the north of Greenland. In all experiments the southern half of the CAA has $10-20\%$ to little ice and the northern half compares well, with a smaller region of $\sim 10\%$ too much ice. On the Beaufort Shelf and along the North Atlantic ice edge, the Tides, Moderate and High Strength, and 2 Ice Category experiments all reduce the amount of ice, bringing these experiments closer to the observed. However, the 2 Ice Category and the High Strength significantly reduce the region of high agreement with observations along the west coast of the CAA. The Tides and Moderate Strength experiments also shrink this area, though by a lesser amount. The High Strength experiment has done best to reduce the regions of enhanced concentrations on the Beaufort Shelf and near Fram Strait. In the central Arctic and in the Kara Sea experiments consistently are missing ice by $\sim 10-20\%$, though the 2 Ice Category and High Strength have significant regions missing 50% of the ice cover. All experiments do not have enough ice in Baffin Bay by $10-20\%$ during this season.

Autumn, thickness difference plots (Figure 3.4) have greater spatial changes than that for ice concentration. The LIM3 Control autumn ice cover is generally $1-2m$ thinner than the observed.

There is a small region restricted along the western CAA coast, extending to northern Greenland where ice is $\sim 1m$ thicker than observed. The LIM2 Control has an area of ice thickness $1-2.5m$ greater than observed to the north of Greenland, extending along the west of the CAA into the central Beaufort Sea. The rest of the domain is covered by ice $\sim 1m$ thinner than the CryoSat-2 observed. Parameter modifications primarily impact the region of thick ice along the west coast of the CAA. Ice density appears to play an insignificant role in modifying the spatial distribution and magnitude of the Arctic ice thickness. The two Ice Bridge experiments increase the region of thick ice. The Moderate Ice Bridge experiment extents the region of thick ice south along the CAA, with ice thickness remaining $\sim 1m$ thicker than observed. The High Ice Bridge experiment pushes this region of thick ice south and further from the coast reaching $\sim 2m$ thicker than observed to the north of Greenland at the mouth of Nares Strait. This experiment also brings ice thickness closer to the observed in the Beaufort Sea. The two ice Strength and Tides experiments have an ice cover thinner than the observed over the entire observational domain. The Moderate Strength and Tides experiments thin ice by an additional $0.25-0.5m$ over the entire domain and the High Strength experiment thins ice by $0.5-1m$. The 2 Ice Category experiment has a thinner ice than the LIM3 Control. In this experiment, along the CAA and Greenland ice is $0.5m$ thicker than the observed. Across the rest of the Arctic, 2 Ice Category ice thickness is comparable to the High Strength experiment. The 8 Ice Category experiment has a similar thickness cover to the LIM3 Control, though thickness compares better to the observed in the Beaufort Sea.

Ocean Response

On a panarctic scale, the top $50m$ ocean temperature sensitivity to the chosen parameters is small. The LIM3 Control reaches a maximum temperature of $5°C$ in September and a minimum of $1.6°C$ in March. Only the LIM2 experiment has a $\approx 0.1°C$ higher temperature in the winter months and a $\approx 0.1°C$ lower temperature during the summer maximum. The 2 Ice Category experiment also has a $0.1°C$ higher temperature than the LIM3 Control in August and September.

Sensitivity of the top $50m$ Arctic-basin, ocean salinity is significant, with differences as great as 0.35 between experiments. The LIM3 control reaches a maximum salinity in April of 32.64 and a September minimum of 32.15. Throughout the year, the LIM2 Control has a 0.2 greater salinity than the greatest LIM3 experiment (2 Ice Category) , which is ~ 0.3 greater than the LIM3 Control. This is consistent with a greater overall volume of ice in the LIM2 Control. The LIM2 Control reaches a maximum salinity of 32.88 April and a minimum of 32.38 in September. The Tides, 2 Ice Category and Density experiments all maintain salinities within 0.05 of the LIM3 Control throughout the year. The 8 Ice Category experiment salinity is consistently 0.05 greater than the LIM3 Control. The Tides experiment closely follows the 8 Ice Category experiment in summer and autumn months. Both the Ice Bridge and Strength experiments act to lower the salinity. The Moderate Ice Bridge experiment maintains a 0.05 lower salinity and the High Ice Bridge experiment has a 0.1 lower salinity compared to the LIM3 Control. Both the Moderate and High Strength experiments have salinities which range from $0.1-0.15$ lower than the LIM3 Control.

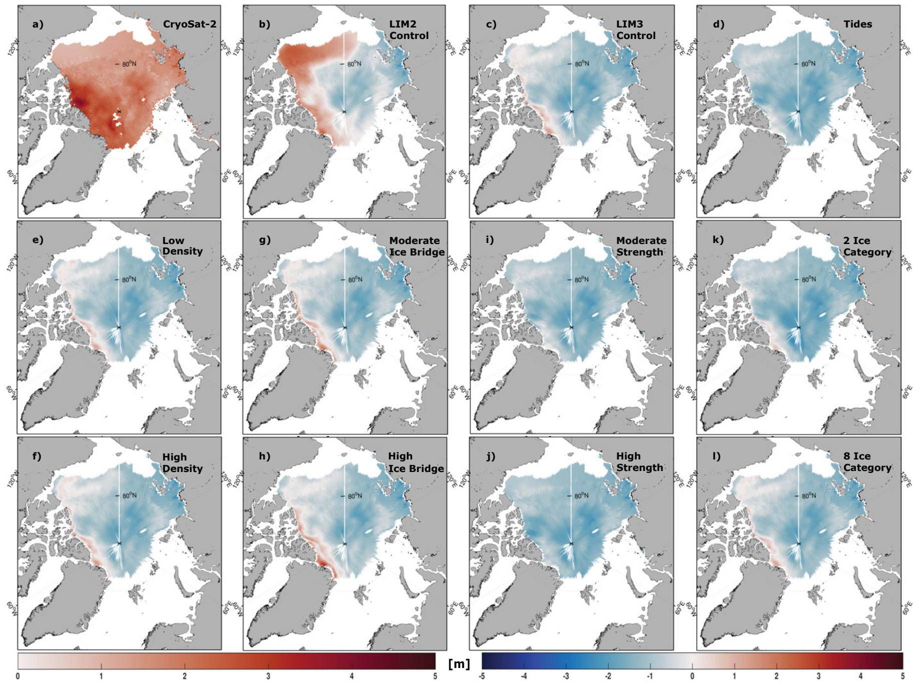

Figure 3.4: Autumn (September-November) 2016 ice thickness difference domain a) Observed CryoSat-2 thickness b) LIM2 Control c) LIM3 Control d) Tides e) Low Density f) High Density g) Moderate Ice Bridge h) High Ice Bridge i) Moderate Strength j) High Strength k) 2 Ice Category l) 8 Ice Category

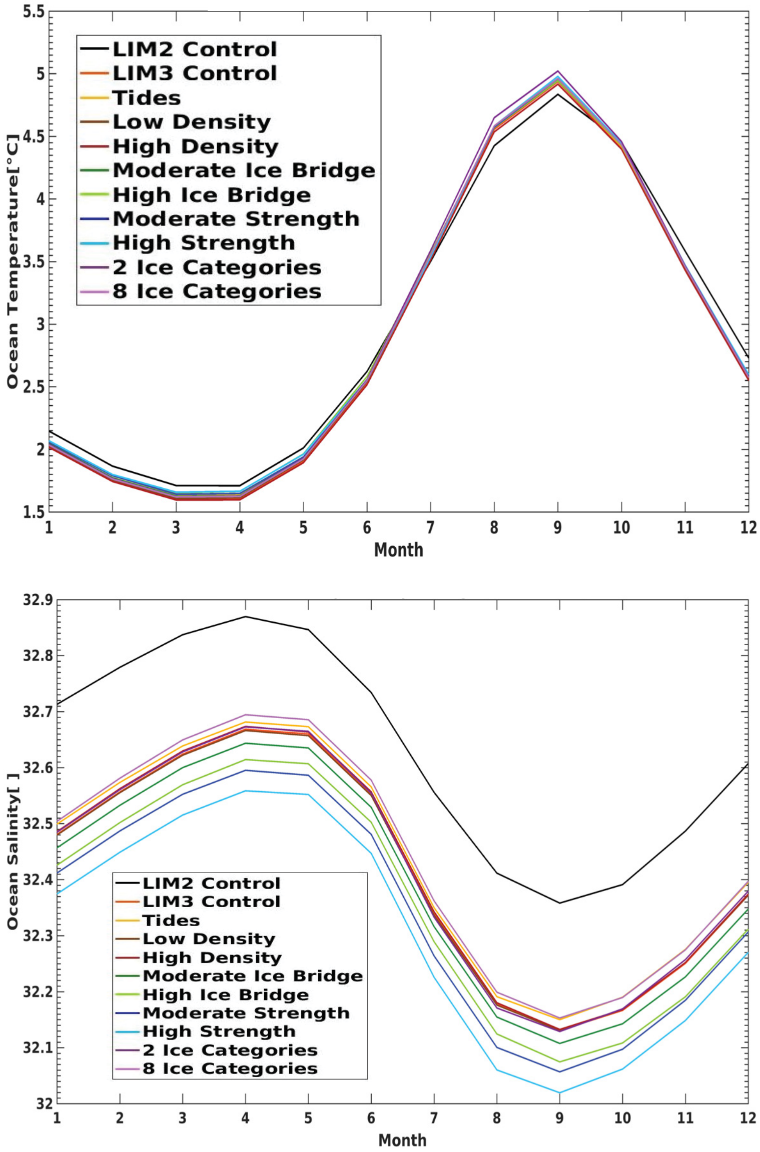

Figure 3.5: Arctic Ocean 2014-2018 monthly, top 50m, a) temperature and b) salinity timeseries

Table 3.3: 2014 - 2018, Annual mean, Pikialasorsuaq sea ice concentration and thickness

Experiment	Concentration [%]	Thickness [m]
LIM2 Control	63.9	0.92
LIM3 Control	65.3	0.70
Tides	65.1	0.67
Low Density	65.5	0.71
High Density	65.4	0.70
Moderate Ice Bridge	64.4	0.68
High Ice Bridge	64.9	0.69
Moderate Strength	65.9	0.67
High Strength	66.5	0.68
2 Ice Category	64.7	0.69
8 Ice Category	65.3	0.70

3.2.2 Pikialasorsuaq

In the Pikialasorsuaq region ice concentration is less sensitive to the selected parameters than on the basin-scale. The LIM3 Control reaches a maximum concentration of 98% ice coverage during the later winter and early spring and a minimum concentration of 8% is reached in August. This experiment maintains a greater than observed concentration from winter to early summer, then closely follows the observed from late summer through autumn. Only the LIM2 Control experiment has a concentration difference from the LIM3 Control greater than $3-4\%$. This experiment has a January to May concentration which is 8% lower than the LIM3 Control, reaching a maximum of 91%. From July to August the LIM2 Control concentration is $5-10\%$ greater than the LIM3 Control. Sensitivity experiments do well to simulate the autumn ice growth period. However, in spring, when the polynya is typically present, is not well simulated. From April to July, all experiments have a $\sim 15\%$ greater than observed ice concentration. Sensitivity experiments do not produce any concentration discrepancies $> 5\%$ at any point of the year.

Pikialasorsuaq region thickness sensitivities are smaller than those for the basin-scale. The LIM3 Control reaches a maximum thickness in April of $1.2m$ and a minimum thickness of $0.15m$ in August. The LIM2 Control reaches a maximum thickness of $1.4m$ in April and a minimum thickness of $0.3m$ in August. The LIM2 Control maintains a thickness which is $\sim 0.2m$ greater than any other experiment throughout the year. From May to July and November to March thickness differences between sensitivity experiments are $< 0.05m$. There is some discrepancy in the March to May maximum thickness, with the Moderate Ice Bridge and the Moderate Strength Experiments having ice that is $0.1m$ greater than the LIM3 Control. All other experiments are within $0.05m$ of the LIM3 Control. During the summer-autumn thickness minimun, the High Ice Bridge, Moderate and High Strength Experiments have ice that is $0.1m$ thinner than the LIM3 Control and the rest of experiments. The High Ice Bridge experiment also reaches an annual minimum in September and not August like all other experiments. Notably, the Moderate Strength Experiment has a greater maximum thickness than the control.

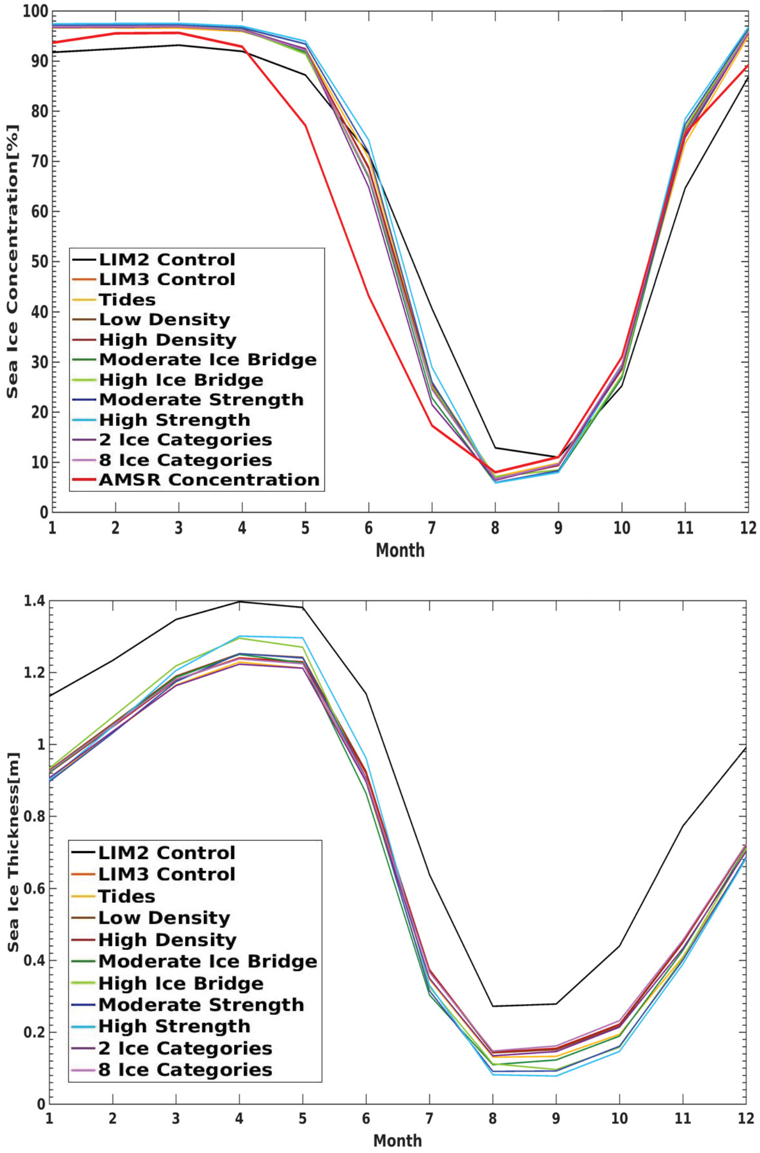

Figure 3.6: Pikialasorsuaq region 2014-2018 average sea ice a) concentration and b) thickness seasonal cycles.

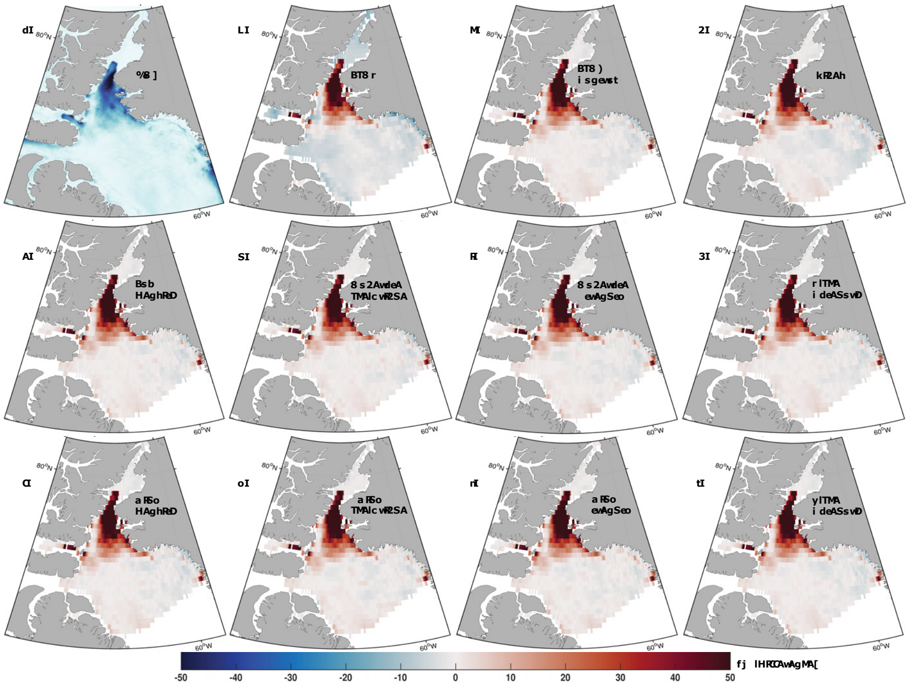

Figure 3.7: April 2015 northern Baffin Bay sea ice concentration. a) Observed AMSR2 concentration b) LIM2 c) LIM3 Control d) Tides e) Low Density f) High Density g) Moderate Ice Bridge h) High Ice Bridge i) Moderate Strength j) High Strength k) 2 Ice Category l) 8 Ice Category

The LIM2 Control maintains a 1.4% lower annual ice concentration and a 0.22m thicker ice cover compared to the LIM3 Control. The Moderate Ice Bridge experiment has a 0.9% lower ice concentration than the LIM3 Control and a 0.02m thinner ice cover. The experiment with the greatest ice concentration is the High Ice Strength, 1.2% larger than the LIM3 Control. The Tides and Moderate Strength experiments have the thinnest ice cover, 0.3m thinner than the LIM3 Control.

3.2.3 April 2015

Spatial differences in ice concentration in the Pikialasorsuaq region show that the distribution of ice changes by only a small percentage between sensitivity experiments. The LIM3 Control has $> 50\%$ too much ice in the polynya itself, though compares well to the observed in Kane Basin, Nares Strait and throughout northern Baffin Bay. The LIM2 Control also has a similar pattern of greater than observed concentrentration. However, outside of the polynya itself the LIM2 Control has $\sim 5\%$ lower concentrations than observed across the domain. Outside of the polynya, sensitivity experiment concentrations are close to observed with typically $< 5\%$ deviation from the AMSR output. No experiment changes the shape of the polynya or concentration by a significant amount.

Spatial plots of ice thickness in the Pikialasorsuaq region highlight that mean thickness changes are primarily the product of changes in ice thickness in Nares Strait. The LIM3 Control has a relatively uniform ice thickness that is 1.5m thick across the region and thick ice of $2.5 - 3m$ in Jones Sound. The LIM2 Control has ice that is $2.5 - 3.5m$ thick in Nares Strait and a distinct

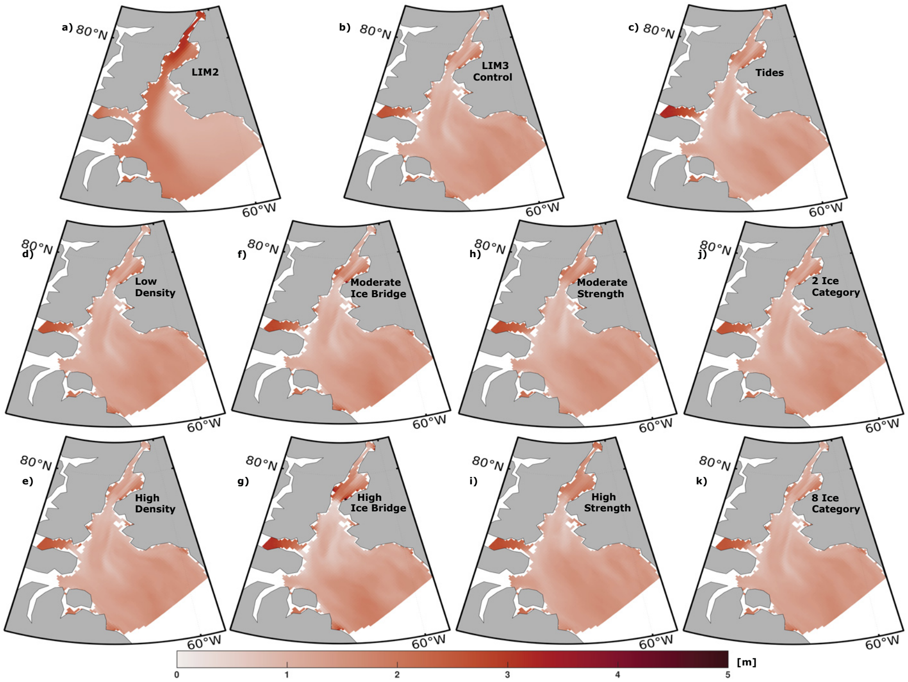

Figure 3.8: April 2015 northern Baffin Bay sea ice thickness. a) LIM2 b) LIM3 Control c) Tides d) Low Density e) High Density f) Moderate Ice Bridge g) High Ice Bridge h) Moderate Strength i) High Strength j) 2 Ice Category k) 8 Ice Category

region of thicker ice on the western half northern Baffin Bay at $\sim 2m$, the eastern side has ice that is $1 - 1.5m$ thick. Sensitivity experiments maintain similar thicknesses across Pikialasorsuaq and northern Baffin Bay, discrepancies occur in Jones Sound and Nares Strait. The Tides experiment increases the thickness of ice in Jones Sound to $\sim 3m$, though the rest of the domain is similar to the LIM3 Control. In the two Ice Bridge experiments there is a net thickening of ice in Kane Basin, particularly at the southern end where the ice bridge typically forms. The High Ice Bridge experiment increases thickness in Kane Basin to $\sim 2.5m$. In the High Ice Bridge experiments there is also an increase in the Jones Sound ice thickness similar to the Tides experiment. In the two ice Strength experiments there is a small increase in ice thickness in the southern end of Kane Basin, though by a smaller amount than in the High Ice Bridge Experiment (reaching a thickness of $\sim 2m$).

Nares Strait Ice Bridge

An ice arch is characterized by a blockage of ice in a region of topographic constriction, behind which ice is stagnant. Ice in front of the ice arch is free to move. Regions of zero ice velocities behind the topographic constriction at the south of Kane Basin with greater ice velocities to the south indicate the presence of an ice arch.

April 2015 velocity sensitivities are most significant in Robeson Channel and Kane Basin. All experiments do well to produce southward flow through Nares Strait which continues into Baffin Bay. In the LIM3 Control there is a persistent flow southward from the Arctic Ocean south through

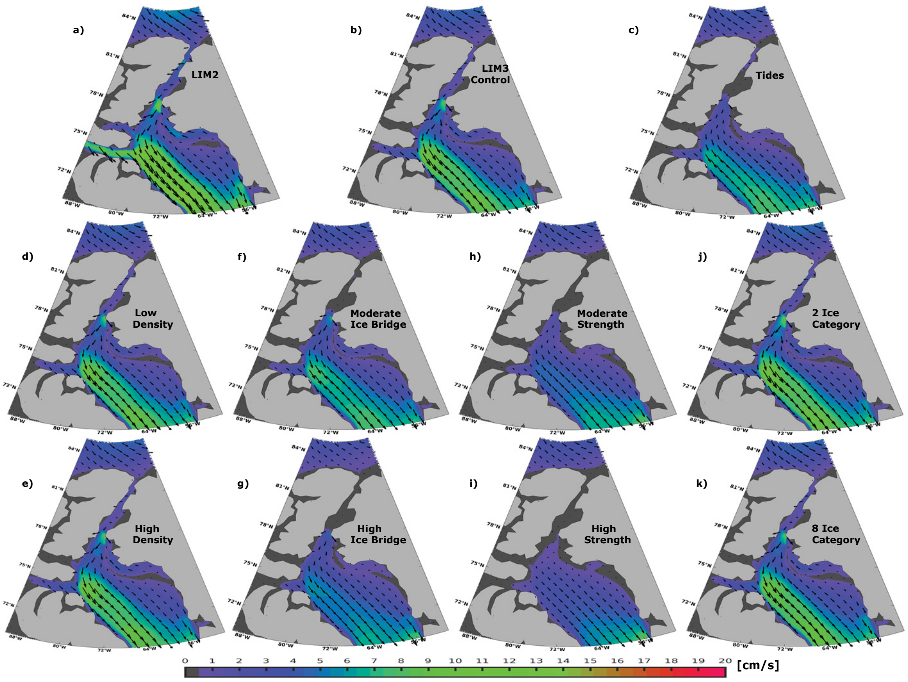

Figure 3.9: April 2015 northern Baffin Bay sea ice velocity vectors. a) LIM2 b) LIM3 Control c) Tides d) Low Density e) High Density f) Moderate Ice Bridge g) High Ice Bridge h) Moderate Strength i) High Strength j) 2 Ice Category k) 8 Ice Category

Nares Strait at $2cm/s$. There is an increases in speed entering Smith Sound, though these velocities slow until entering Baffin Bay where ice continues to move southward. The LIM2 Control has $2-4cm/s$ larger velocities throughout the domain. Nares Strait ice velocities reach $8cm/s$ in the LIM2 Control. The LIM2 Control is the only experiment with a velocity core in Lancaster Sound, with velocities reaching $10-12cm/s$.

From April 2015 velocities it is clear that the Nares Strait ice Bridge is forming only when modifying certain parameters. Both the Ice Bridge and ice Strength experiment sets improve the ice velocities in terms of the formation of the ice bridge in Nares Strait. Near-zero sea ice velocities from the south end of Kane Basin extending through Robeson Channel are only produced in the Tides, Ice Bridge, and ice Strength experiments. These experiments also have a $2-3cm/s$ decrease in the Baffin Island Current vicinity. The High Strength experiment has near-zero velocities extending along the coast of Baffin Bay. In the Moderate and High Strength experiments, ice motion is more uniformly directed to the southeast. Finally, the April 2015 velocity fields in northern Baffin Bay appear insensitive to changes in ice density and the number of ice thickness categories.

3.3 Discussion

The transition from the LIM2 to LIM3 sea ice model plays a greater role in impacting ice thickness and concentration than any of the sensitivity experiments. Though, sensitivity experiments

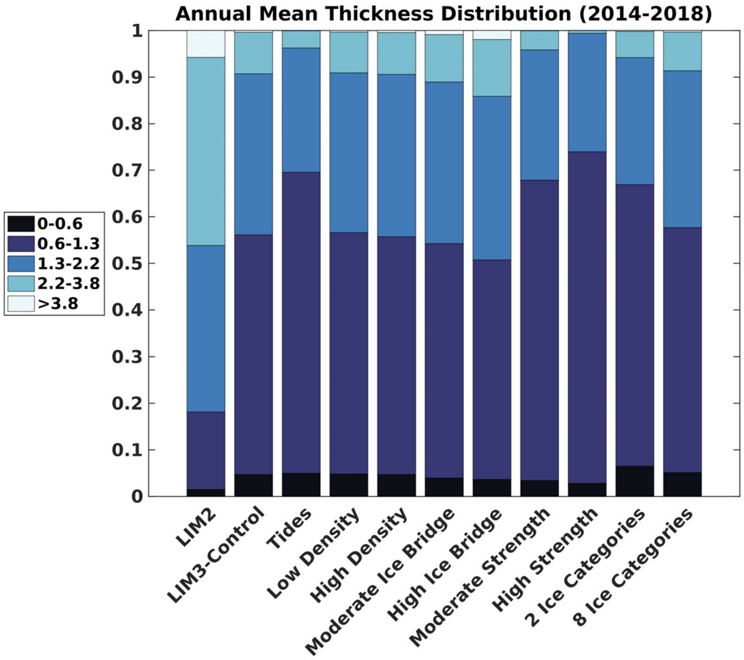

Figure 3.10: Panarctic Ice Thickness Distribution. The 2014-2018 average percentage of the CryoSat-2 domain ice thickness distribution. Bins are defined as the 5 thickness bins used by the LIM3, 5 ice cateogry thickness distribution

do produce non-negligible changes to the ice extent, thickness, and concentration on basin-scales and in the Pikialasorsuaq region.

3.3.1 Ice Thickness Distribution

On long time scales, the ice thickness distribution is an expression of the time-integral of interactions between the thermodynamic and dynamic responses of the ice cover to atmospheric and oceanic forcings (Thorndike et al., 1975). In the context of sensitivity experiments, changes to the ice thickness distribution are a response to parameter perturbations. Changes to the ice thickness distribution result in changes to the mean ice thickness by a net thickening and thinning of ice and changes to the ice concentration, where a thinning of ice can result in more open water.

Figure 3.10 shows the areal extent of the annual average from 2014-2018 of the five ice thickness categories. The Tides and ice Strength experiments produce a net thinning of ice and the Ice Bridge experiments produce a net thickening of ice. There are different portions of the ice thickness distribution which are impacted by the sensitivity experiments. The LIM3 Control, High Density, Moderate and High Ice Bridge experiments all have some portion of the Arctic covered by the thickest ice category ($h > 3.8m$). The LIM2 Control has 5% of the region covered by ice of this thickness. While the LIM3 Control experiment has a $\sim 1\%$ coverage of thick ice and the High Ice Bridge experiment has a $\sim 2\%$ coverage. Ice density does not impact the ice thickness distribution by a significant amount. Increasing the ice strength and including tides diminishes the region of thick ice. Also note, that in order to include tides, there was a necessary increase in the ice strength to the Moderate Strength Value ($40000 N/m$). Hence, an increased ice strength and the subsequent decrease in ridging and rafting thins ice and removes all ice from the maximum thickness category. Since the LIM2 Control has no processes to represent ridging or rafting, the larger areal extent of ice with thickness $> 3.8m$ must come from enhanced ice growth process and less melting of thick ice. LIM3 includes mechanical redistribution of ice thickness due to ridging and rafting, though no LIM3 experiment have as large an area of thick ice than the LIM2 experiment. Holland et al. (006a), show that an ice thickness distribution can lead to enhanced growth rates and a greater ice-albedo feedback. Thus, the LIM3 has two processes which would be expected to generate thicker ice, though this is not the case. It is also clear that, in LIM3, it is mechanical redistribution which puts ice into the maximum thickness categories and not thickness growth through thermodynamics such as the case in the LIM2 Control.

The thinnest ice category has ice of thickness, $h < 0.6$. Changes in the areal extent of the thinnest ice are most notable between the LIM2 Control and LIM3 experiments. As the LIM2 Control is a single category sea ice model, resolving regions of thin, newly formed ice are difficult on a coarser resolution such as the $1/4^\circ$ used in this study. This also could represent enhanced growth rates such as was mentioned by Holland et al. (006a) and there is more ice forming in leads and cracks that LIM2 does not resolve. The Moderate and High Strength experiments have $\approx 2\%$ less ice in the smallest thickness category and the 2 Ice Category has 2% more ice in this category than the LIM3 Control. In the 2 Ice Category experiment, ice is readily put into the larger of the two categories through thermodynamic growth and mechanical redistribution and the smaller category is free to have a thinner ice thickness in it, leaving more grid cells with ice in the minimum thickness category. The 2 Ice Category experiment does not resolve the thin ice as well as the nominal five and has the greatest areal extent of ice with thickness $0.6 - 1.3m$. This indicates that a poor resolution of ice slightly increases the mean thickness of ice. Fewer ice thickness categories would also act to reduce the amount of riding and rafting which occurs. Since the thinnest ice category has a greater maximum than with five categories, it would take a greater amount of energy to ridge or raft ice. Thus, ice in the lowest category predominantly grows in thickness space through thermodynamic processes rather than through mechanical redistribution, creating a larger region of thin ice. The opposite can be said for increasing the ice strength, as ice does not grow in thickness space due to ridging and rafting at the same rate, each grid cell is dominated by ice which thickens through thermodynamics leaving little room for the thinnest ice category and ice growth. The High Strength experiment again has fewer instances of ridging and rafting processes and thus it is observed that most ice lies in the thickness category $1.3 - 2.2m$, and reaches this thickness due to thermodynamic growth. The High Ice Bridge experiment has an overall increase in thickness due to enhanced build-up of ice in narrow channels across the Arctic. The 8 ice category thickness distribution is similar to the LIM3 control though includes a higher resolution of thin ice. Enhanced resolution of ice thickness has little impact on the overall thickness distribution, though this change is observed in the panarctic averaged ice concentration through a lower summer minimum ice concentration than the LIM3 Control. More thin ice categories appears to enhance the summer melt. Though enhanced growth makes up for this and produces a similar ice cover.

The same trends in the ice thickness distribution changes are observed in each season. Highlighting that the selected parameters produce consistent changes to the thickness distribution and the subsequent mean thickness and concentration.

In northern Baffin Bay spatial sensitivities are minimal. All experiments have too much ice in the polynya extending down into Jones Sound. Sensitivity experiments do not significantly impact the mean thickness in the region and concentrations remain high in the polynya regardless of the parameter modifications. The LIM2 Control experiment does not have the velocity signature associated with an ice arch in Nares Strait. Thus, it is expected that the polynya is not well resolved and a large volume of ice moves through the strait into Baffin Bay throughout the year. The Ice Bridge, ice Strength, and Tides experiments do have this velocity signature. Though these experiments have similar concentrations as both the LIM2 and LIM3 Control, possibly indicating that the ice bridge is not forming for long enough, ice is not moving out of the region, or ice is readily forming in the open water at rates which are greater than the what is physically occurring. However, model ice growth rates (not shown) in the region do not exceed the $1.2 m/month$ value discussed by Yao and Tang (2003) on large scales, only in a small localized region adjacent to the ice arch. Values of $1.5 m/month$ were only found in the Ice Bridge experiments which best form the ice arch. Ice velocities next to the ice arch are significant enough ($2-5 cm/s$) to move ice south and away from the arch. Thus, the ice arch must be forming and breaking down and letting ice pass through in timescales finer than a monthly average. This highlights the need for further model improvement such as a parameterization of landfast ice to help better represent the ice arch in the shallow water of Nares Strait.

3.3.2 Ice Velocity Divergence

Arctic sea ice velocity divergence sensitivities aid in explaining of basin-scale thickness and extent sensitivities. A larger convergence induces ridging and rafting which consumes ice area, diverging conditions decrease local thickness by creating open water and spread ice out over a greater area. Additionally, ice divergence is conducive ice growth in the open water it generates. As all experiments are subject to the same atmospheric forcing and changes to divergence are primarily the product of changes to ice strength (i.e. thickness) in sensitivity experiments.

In general, the 2015 annual mean ice velocity divergence fields are similar (Figure 3.11), this is the case for all years in which experiments were run. The CAA is characterized by generally convergent motion in the central and eastern portion, whereas the western half has a significant divergent region. Thus, concentrations are similar between all experiments. The LIM2 Control has a significantly greater thickness in the region, which is then expected to be caused by enhanced import of ice from the Arctic. This idea is discussed in the coming section: *Ice Volume Fluxes*. The central Arctic generally has similar convergence rates across sensitivity experiments. This convergent motion is caused by Ekman transport pushing ice towards the west coast of the CAA, creating

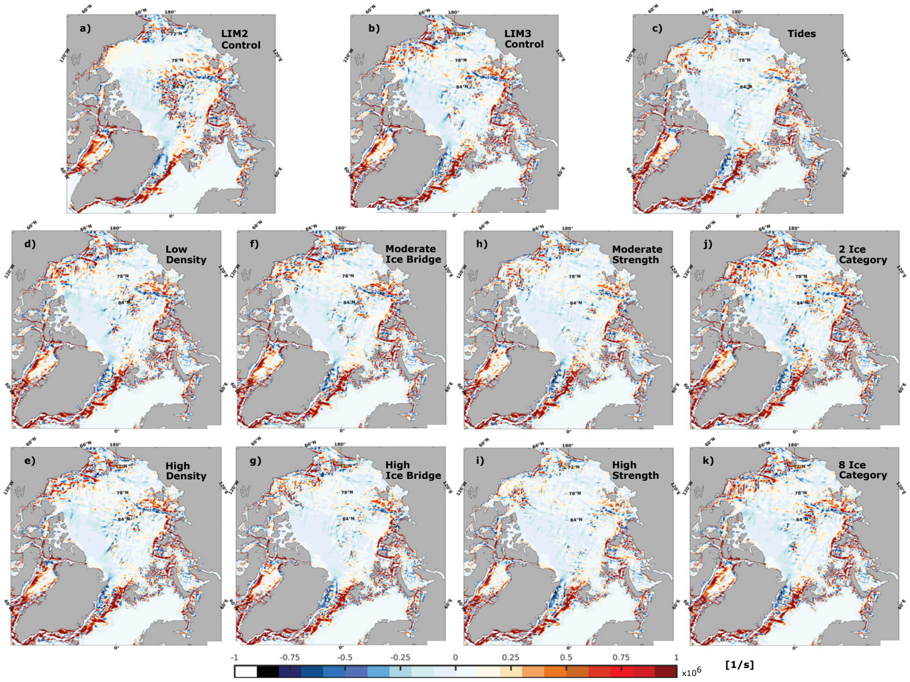

Figure 3.11: 2015 Panarctic annual mean ice divergence. a) LIM2 Control b) LIM3 Control c) Tides d) Low Density e) High Density f) Moderate Ice Bridge g) High Ice Bridge h) Moderate Strength i) High Strength j) 2 Ice Category k) 8 Ice Category

the largest ice thicknesses in the Arctic. However, there is a notable decrease in the convergent rate in both the Moderate and High Strength experiments, largely due to enhanced ice strength creating a more rigid ice pack. This explains a thinner ice cover in the region as less ice is building up on the coast. A decrease in the convergence rate is also observed in the Moderate and High Ice Bridge experiments, though by a lesser amount. This is in contrast to the thicker ice observed in the region. The Ice Bridge experiments are thickening ice over a broader region to the west of the CAA as ice jams in the narrow channels, and thus ridging occurs over a greater region. In the north pole vicinity, the LIM2 Control has a more active divergence field than any of the LIM3 experiments. The LIM3 Control and Low Density, 2 Ice Category, and 8 Ice Category experiments are comparable, while the Tides, ice Strength, and Ice Bridge experiments have slightly converging ice conditions near the North Pole. All experiments have lower concentrations than observed and are thinner than observed ice covers in this region. A too active or too stagnant ice pack may be contributing to these discrepancies. The divergence field on the Beaufort Shelf also has discrepancies. This a region where the LIM2 Control has significantly too much ice and LIM3 is performing better. The LIM2 Control ice cover is weakly diverging with minimal changes extending west to Bering Strait. LIM3 experiments however, have a more active ice velocity field which is more indicative of the variable ice motion in the region (e.g. Asplin et al. (2009)). The lack of diverging conditions on the Beaufort Shelf in the LIM2 Control helps to explain the large ice concentration and in the region. Diverging conditions generate more open water, conducive to ice growth. More ice is expected to form in the region, unlike what is occurring in any of the LIM3 experiments. The LIM3 ice cover is much more dynamic and is similar across all experiments and the balance of converging and diverging motion creates non-obvious changes to the ice cover. The Russian shelf seas and the North Atlantic display the smallest sensitivity, with diverging conditions to the east of Greenland. The Barents and Kara seas both have an active ice cover in all experiments.

3.3.3 Ocean Response

The basin averaged, top 50m ocean temperature is quite insensitive to sea ice model parameter changes, while top 50m ocean salinity has responses as great as 0.35. Temperature sensitivities, or there lack of, can be traced back to the small changes in ice concentration and extent produced between each experiment. As the selected parameters only play a small role in modifying the sea ice concentration and extent, subsequently there is minimal changes to the amount of incoming solar radiation which reaches the ocean surface. Further, both models do not allow any solar radiation to enter the ice system through snow, and thus inhibiting solar radiation transfer at these location. Only regions of thin, bare ice or open water contribute to ocean temperature discrepancies in the top 50m and these are small between each experiment as shown in the concentration timeseries and spatial plots (Figure 3.2a and 3.3).

Top 50m ocean salinity sensitivities are significant, with a range of ~ 0.35 between the summer minimum of the High Strength Experiment (32.05) and the LIM2 Control (32.4) experiments. The large discrepancy between LIM2 and LIM3 can be attributed to the difference in overall volume of ice. The LIM2 Control is found to have a thicker ice cover than any of the LIM3 experiments and a similar concentration, indicating a greater volume and therefore a greater volume of freshwater in the sea ice system. With more freshwater trapped in sea ice, the LIM2 Control ocean salinity must then be greater than any of the LIM3 experiments which have a lesser ice volumes. The lowering of ocean salinity from the LIM3 Control value in the ice Strength experiments is due an absence of ridging and rafting. The process of mechanical redistribution in thickness space due to ridging and rafting brings ocean water into the sea ice system, making this ice more saline. This process is parameterized in LIM3 by making newly formed ridges slightly porous to make room for added ocean water (Vancoppenolle et al., 2009). In the Moderate and High Strength experiments less ridges are being formed and thus less saline waters are moving into the sea ice system. Finally, there is less overall sea ice volume with a thinner cover. The two Ice Bridge experiments also lower the top 50m ocean salinity by ~ 0.05 compared to the LIM3 Control, though the reasoning for this appears to be more complex. Decreasing the eccentricity of the elliptical yield curve and increasing the ice shear strength results in a net thickening of ice in both experiments. This process occurs primarily along the west coast of the CAA as ice builds up along narrow straits. This build-up of ice is the result of greater ridging and rafting as these locations since the ice is more stiff and less likely to move through the channels. As discussed in the ice Strength experiments, greater ridging and rafting would be expected to take more saline waters from the ocean into the ice system, thereby raising the ocean salinity as salts are flushed from the ice back into the ocean. Additionally, as the

Ice Bridge experiments increase ice thickness, this is conducive to a greater longevity of ice. LIM3 includes brine drainage and flushing as ice ages, (Vancoppenolle et al., 2009), thus putting more salt back into the ocean, raising salinity. However, both the Moderate and High Ice Bridge experiments have a net freshening effect. A more in-depth response of the EVP rheology to changes in the eccentricity of the elliptical yield curve are necessary to understand the cause of this freshening.

3.3.4 Ice Volume Fluxes

The monthly ice volume fluxes are plotted for four key straits in the Arctic; Nares, Davis, Bering, and Fram Straits. These straits represent critical ice pathways in the Arctic. The width of these straits varies greatly and thus the physics governing ice motion through them are different. Nares and Bering Straits are narrow and thus ice strength and thickness play significant roles, while Davis and Fram Straits are wide and large-scale circulation of the ocean and atmosphere play leading roles.

In Nares Strait, the LIM2 Control is not able to produce an ice arch and therefore has a negative (positive is directed into the Arctic) volume flux at all times. All sensitivity experiment maintain an ice volume flux (Figure 3.12a) lower than the LIM3 Control regardless of the parameter perturbation. Though, the Ice Bridge and High Strength experiments have volume fluxes which are most consistent with the presence of an ice arch. That is, significant periods of zero flux when ice arch is expected to be present. The annual mean from 2014 - 2018 of the Moderate Ice Bridge experiment is $106.1km^3$ and the High Ice Bridge annual average is is $94.6km^3$. The two Ice Bridge experiments decrease the eccentricity of the elliptical yield curve thereby increasing the shear strength of the ice, making it more cohesive and stiff (Dumont et al., 2009). In these experiments, ice is more prone to jamming in narrow straits. Increasing the ice strength in the two Strength experiment makes the ice pack more resistant to convergent motion and thus less ridging and rafting. As the ice pack is more resistant to convergent motion it is less prone to being pushed through narrow straits such as Nares Strait. The High Strength experiment has the lowest annual ice volume flux at 83.9 km^3, as much of the ice in the ice in Nares Strait is stagnant (Figure 3.9). Thus, an ice pack which is more resistant to convergent motion is less susceptible to being pushed through narrow channels. The Tides experiment does not reach the same maximum values and does not reach a zero ice volume flux at any time of the year. Thus tidal velocities are keeping ice mobile throughout the year, regardless of the increased strength (the same value as the Moderate Strength experiment), and lowers the annual maximum value compared to the LIM3 Control. The Tides experiment mean is $20.6km^3/yr$ larger than the Moderate Strength experiment and thus are playing a significant role in pushing ice through the strait. The two ice Density experiments have the same annual ice volume fluxes which are lower than the LIM3 Control with similar monthly timeseries. This indicates that increasing or decreasing ice density, thereby makes ice less or more receptive to wind forcing, respectively. Subsequently, changes to this balance of wind and oceanic forcing makes ice less prone to moving through Nares Strait. This could indicate that a correct balance between atmospheric and oceanic forcing pushes ice into the Strait. Modifying the number of ice categories also acts to significantly lower the amount

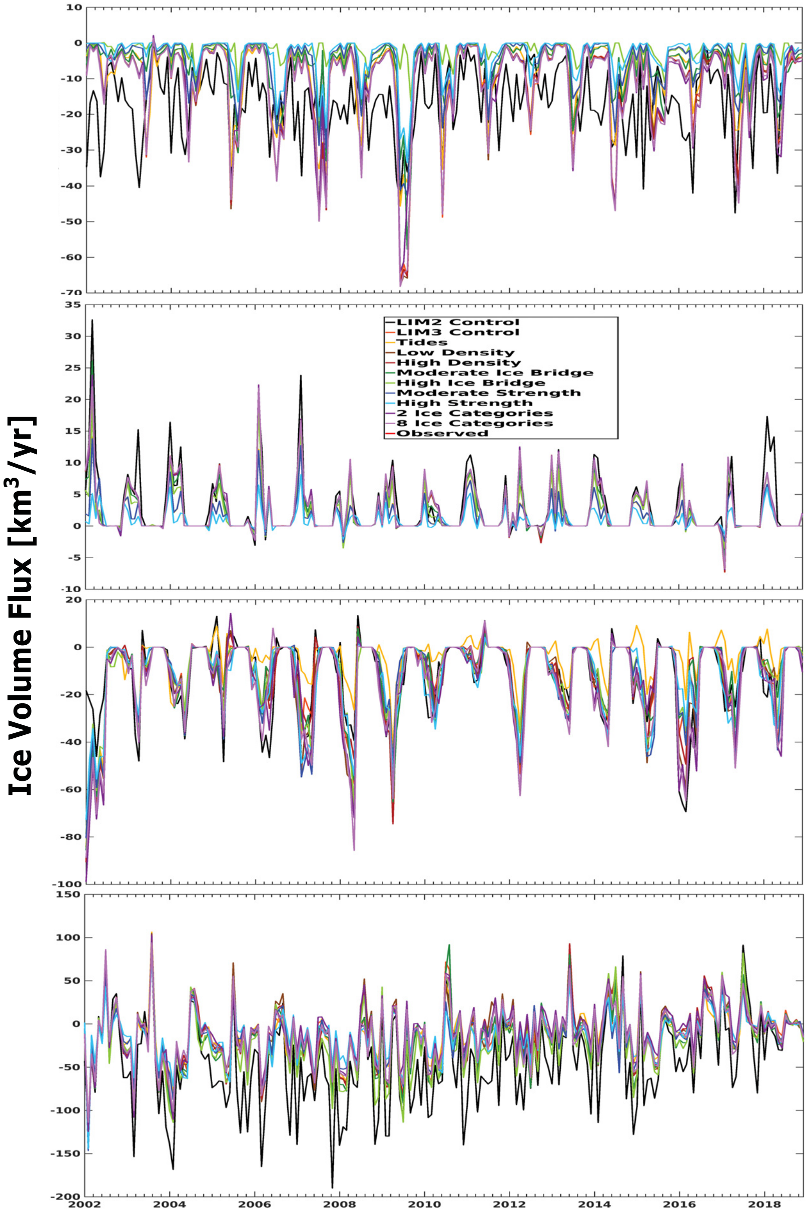

Figure 3.12: Monthly Ice Volume Fluxes of key Strait in the Arctic. a) Nares Strait b) Bering Strait c) Davis Strait d) Fram Strait

Table 3.4: 2014 - 2018 Annual, mean, ice volume fluxes [km^3/yr], magnitude of ice volume fluxes, directional changes can be found in Figure 3.12.

Experiment	Bering	Davis	Fram	Nares
LIM2 Control	52.2	95.3	88.3	136.4
LIM3 Control	36.5	108.6	30.3	120.7
Tides	29.8	76.8	19.1	112.0
Low Density	27.6	83.6	17.1	110.1
High Density	26.3	89.1	13.8	110.0
Moderate Ice Bridge	25.2	87.0	15.0	106.1
High Ice Bridge	24.5	86.8	15.6	94.6
Moderate Strength	23.5	93.7	13.5	89.6
High Strength	22.5	98.1	11.7	83.9
2 Ice Category	22.4	103.6	14.7	87.7
8 Ice Category	22.3	108.1	13.3	89.9

of ice moving though Nares Strait on an annual basis, though the monthly timeseries is comparable to the LIM3 Control, indicating a systematic thinning of the ice moving through the Strait and not a change in seasonality. The 8 Ice Category experiment has a high resolution of thin ice, which is more readily pushed through narrow channels due to its lower strength. More thin ice moving through the channel itself may be responsible for the lower 8 Ice Category volume flux in Nares Strait. The 2 Ice Category does not have the same thickness resolution as the LIM3 Control, having only a single category for thinner ice and one for thicker. The thinner of the two categories is again preferentially pushed through the narrow channel due to its lower strength. The 2 Ice Category experiment has the largest areal extent of ice with thickness $h < 0.6m$ and thus this ice is most readily pushed through the Strait.

The estimate of Kwok (2005) of $\sim 100km^3$ is comparable to all sensitivity experiments. However, Kwok (2005) estimated the ice thickness to be $4m$, greater than the regional thickness found in any experiment. The real value is expected to be lower than the estimate. The LIM2 Control annual volume flux is significantly higher at $136.4km^3$. The High Strength has the lowest flux at $83.9km^3$. The 2 and 8 Ice Category values are $87.7km^3$ and $89.9km^3$, respectively which are both more realistic than the LIM3 Control. Volume fluxes combined with the Nares Strait ice velocity sensitivities show that parameter modifications are necessary to best simulate Pikialasorsuaq. As the polynya is a critical ocean ecosystem, it is desirable to accurately represent the dynamic processes which form it. Correct modelling of these processes opens the door for climate studies which predict the future of the polynya. Further, as these ice arches are found to be forming at Nares Strait, it can likely be assumed that they are forming in other narrow channels across the Arctic, providing more realistic ice-ocean-atmospheric heat, momentum, and freshwater exchanges.

All experiments have similar period of zero volume flux as this is the period where no ice is present in summer months. Both the increasing the strength and decreasing the eccentricity of the elliptical yield curve lower the monthly mean. The High Strength and Ice Category experiments maintain the lowest annual mean fluxes of $22.5, 22.4$, and $22.3km^3$, respectively. The reasoning for the High Strength experiment and Ice Category experiments lowering ice volume fluxes are similar to that discussed for Nares Strait in the previous paragraph. The LIM2 Control annual mean flux is more than double the lowest values at $52.2km^3$ as ice motion is greater in this experiment than any experiments which use LIM3 and the ice thickness is larger. The Tides experiment has an annual mean of $36.5km^3$, greater than the Moderate Strength value of $23.5km^3$, thus tidal velocities are enhancing ice motion through the narrow Bering Strait. All other experiments maintain similar monthly timeseries and annual mean values. All LIM3 experiment annual means are lower than the LIM2 Control. Travers (2012) gave an estimate to the Bering Strait ice volume flux of $190 \pm 50km^3/yr$, significantly higher than any of the experiments in this study. The large discrepancy likely is due Bering Strait being located near the edge of the Bering Strait mesh. Boundary conditions are playing a larger role in discrepancies than model shortcomings.

Davis Strait does not experience ice bridge formation and, thus the response of the ice volume flux to the chosen parameters is different. Additionally, at Davis Strait there is two directional ocean velocity, though the vast majority of ice exits via Baffin Bay on the western half of the strait (negative flux) and a smaller volume enters Baffin Bay in the eastern half of the strait (positive flux). The LIM2 Control has an annual mean of $95.3km^3$ and the LIM3 Control has a mean of $108.6km^3$. The Tides experiment maintains the lowest ice volume flux throughout the has an annual flux of $76.1km^3$. A potential mechanism for this could be enhanced tidal mixing is bringing more warm water to the surface, melting ice. Changing the number of ice categories does not significantly change the monthly timeseries or annual mean ice volume flux at Davis Strait. Modifying the ice density, strength and eccentricity of the elliptical yield curve lower the volume flux compared to the LIM3 Control. Over the 2014-2018 averaging period the ice Strength experiments do not have as large an annual maximum flux as the LIM3 Control or Ice Category experiments, this is likely tied to a smaller volume of ice entering Baffin Bay through the CAA and Nares Strait. A similar argument can be made for the two Ice Bridge experiments. The reasoning the two ice Density experiments have lower Davis Strait ice volume fluxes is unclear. At a wide strait such as Davis Strait is would be expected that atmospheric forcing dominates ice transports and thus the low density ice is more readily pushed by winds. The monthly timeseries indicates that both ice Density experiments have annual maximum fluxes which are lower than the LIM3 Control. It is then likely that the two directional flow and a mean wind direction which shifts throughout the year and across the wide strait are limiting significant ice transports in a single direction. Lee et al. (2014) estimated the Davis Strait ice volume flux at $-10 \pm 1mSv$ (directed out of Davis Strait), which is equal to $315.4 \pm 31.5km^3/yr$. Again this value is significantly greater than the highest experiment, the LIM3 Control. Further analysis is required to differentiate the southward flowing component from the northward. Directional fluxes would provide clarification on the mechanisms which are causing the discrepancy: not enough ice moving out of Baffin Bay, or too much ice moving northwards along the Greenland coast.

Fram Strait also has a different set of dynamics which determine the monthly ice volume flux. As this strait is wider than any of the others plotted and has two directional ocean velocities, large scale ice thickness plays a significant role in determining the ice volume flux. Therefore, the LIM2 Control, with the greatest thickness, has the greatest Fram Strait volume flux. This experiment maintains the greatest monthly volume flux directed out of the Arctic. The LIM2 Control annual flux is $136.4km^3$. The LIM3 Control annual mean is $120.7km^3$, higher than any of the sensitivity experiments. The High Ice Bridge has significantly greater maximum and minimum fluxes compared to the other LIM3 experiments. The LIM2 Control does not have significant periods of ice fluxes directed into the Arctic, where all LIM3 experiments are a more even split between periods of outflow and inflow. LIM3 experiments all maintain a thinner ice cover than the LIM2 Control and Fram Strait ice volume fluxes are expected to be lower. However, the High Ice Bridge, which maintains the greatest basin-averaged thickness of any LIM3 experiment, has a lower Fram Strait ice volume flux than the LIM3 Control. Thus the sensitivities are not straightforward as the dynamics are more complex than the other three staits looked at. A more in depth study is required to find a driver for these sensitivities at Fram Strait. Spreen et al. (2020), found the annual volume flux to be $2400 \pm 640km^3$, an order of magnitude larger than the sensitivity experiments. However, Spreen et al. (2020) calculated only the outgoing volume flux at a location south of that used here. The values presented here include the northward moving component and thus values are predicted to be lower. Lower than observed ice concentrations in all sensitivity experiments are also predicted to play a role in modifying the Fram Strait ice volume flux.

From the previous section on the ice divergence fields, the four straits analyzed all have similar divergence values. Thus changes in ice volume flux are not though to be a product of changes in the divergence field and rather the ice strength in narrow channels (Bering and Nares straits) and ice thickness and oceanic circulation on larger straits (Davis and Fram straits).

The discrepancy between the LIM2 and LIM3 models are larger than any of the sensitivity experiments when considering sea ice extent, concentration, and thickness. Though sensitivity to tidal constituents, ice density, the eccentricity of the elliptical yield curve, ice strength and the number of ice thickness categories are non-negligible. Particularly in terms of Arctic ocean average ice thickness and processes involved in the formation of the Nares Strait ice bridge.

The Arctic ice extent and northern Baffin Bay ice concentration region display only small sensitivities to the selected parameters. The panarctic and northern Baffin Bay concentrations compare well to the AMSR-E and AMSR2 ice concentrations in terms of seasonal cycles. Arctic sea ice extent is most sensitive to decreasing the number of ice thickness categories from 5 to 2 which lowers the summer minimum by $1.0 \times 10^6 km^2$ and decreasing the eccentricity of the elliptical yield curve from 2.0 to 1.2 increases the minimum extent by $0.2 \times 10^6 km^2$ from the LIM3 Control. LIM3 thickness better matches the CryoSat-2 ice thickness in all experiments. Basin-averaged ice thickness is most sensitive to increasing the ice strength from $20000N/m$ to $60000N/m$ which decreases thickness by $\approx 0.15m$, and decreasing the eccentricity of the elliptical yield curve from 2.0 to 1.2 which increases thickness by $\sim 0.1m$ compared to the LIM3 Control. The later experiment best compared to the observed Arctic ice thickness. In the Pikialasorsuaq region, thickness sensitivities are smaller, with only the High Strength and Ice Bridge experiments having a $0.1m$ greater spring maximum thickness, compared to the LIM3 Control. These two experiments also have a $0.1m$ lower summer minimum ice thickness. The LIM2 Control also maintains a thickness which is $0.2m$ greater than the LIM3 Control. Lowering the eccentricity of the elliptical yield created a velocity signature in Nares Strait consistent with the formation of an ice bridge. Increasing the ice strength has a similar impact, though regions of stagnant ice extended outside of Nares Strait along the Greenland coast.

The ice thickness distribution, horizontal divergence, and ice volume fluxes further highlight the Arctic sea ice response to parameter perturbations related to ice motion and mechanical redistribution. Horizontal divergence helps to display changes in the Arctic basin-scale extent and thickness as convergent motion consumes ice area and creates pressure ridges, where divergence creates regions of open water. Increasing the ice strength and decreasing the eccentricity of the elliptical yield curve decrease convergent motion to the west of the CAA. The LIM2 Control does not have the same dynamic ice cover on the Beaufort Shelf as the LIM3 experiments. The ice volume fluxes highlight the need for parameter modification of the ice strength and eccentricity of the elliptical yield curve to resolve Arctic ice arches. Larger straits, Fram and Davis have more complex sensitivities to the chosen parameters. The ice thickness distribution shows the improved resolution of thin ice in the LIM3 Control compared to the LIM2 Control. The two ice Strength experiments and the Tides experiments remove thick ice by limiting ridging and rafting. Decreasing the eccentricity of the elliptical yield curve increases thickness by building up ice along the narrow channels of the CAA. Decreasing the number of ice thickness categories acts to increase the area of ice with a thickness of $0.6-1.3m$ due to decreased vertical resolution of ice thickness.

The LIM3 model is shown to better simulate regions of thin ice as well as the ice extent and concentration on different scales. Further, LIM3 is able to to simulate critical ice arches across the Arctic as well as creating more realistic ice volume fluxes. In the future there is expected to be more thin ice and a more mobile ice pack, thus this model may be better suited for climate change studies.

While the LIM3 Control shows significant from the previous LIM2 model, sensitivity experiment show better agreement with observations. Specifically, including nine tidal constituents (and the necessary increase in ice strength to the Moderate Strength experiment value) improves the summer minimum ice extent and concentration. Decreasing the eccentricity of the elliptical yield curve, and thus increasing the ice shear strength better matches the observed Arctic average ice thickness and improves the formation of ice arches as does increasing the ice strength. Ice density and modifying the number of ice thickness categories did not produce significant changes to warrant future modification. Thus, a suggested set of parameters to better simulate Arctic sea ice on a basin-scale and for northern Baffin Bay is: keep the ice density at $917kg/m^3$, include nine tidal constituents (K1, K2, M2, M4, N2, O1, P1, Q1, S2), decreasing the eccentricity of the elliptical yield curve from $e=2.0$ to $e=1.2$, and increasing the ice strength from $P^*=20000N/m$ to $P^*=40000N/m$. This parameter set appears suitable for both Arctic basin-scale studies and in the Pikialasorsuaq region. Modifying the selected parameters will bring the average ice thickness closer to the observed, creating a more realistic thickness distribution, and resolve processes associated ice volume fluxes and ice bridge formation across the Arctic.

Bibliography

Asplin, M., Lukovich, J., and Barber, D. (2009). Atmsheric forcing of the beaufort sea ice gyre: Surface pressure climatology and sea ice motion. *Journal of Geophysical Research: Oceans*, 114.

Bamber, J., van den Broeke, M., Ettema, J., Lenaerts, J., and Rignot, E. (2012). Recent large increases in freshwater fluxes from greenland into the north atlantic. *Geophysical Research Letters*, 39(19).

Barnier, B., LeSommer, J., Molines, J., Pendruff, T., Treguier, S. T. A., and et al. (2007). Eddy-permitting ocean circulation hindcasts of the past decades. *CLIVAR-Exchanges*, 12:8–10.

Cavelieri, D. and Parkinson, C. (2012). Arctic sea ice variability and trends, 1979-2006. *J. Geophys. Res.*, 113.

Comiso, J. (2012). Large decadeal decline of the arctic multiyear ice cover. *Journal of Climate*, 25:1176–1193.

Dai, A., Qian, T., Trenberth, K., and Milliman, J. (2009). Changes in continental freshwater discharge from 1948 to 2004. *Journal of Climate*, 22:2773–2792.

Dai, A. and Trenberth, K. (2002). Estimates of freshwater discharge from continents: Latitudinal and seasonal veriations. *Journal of Hydrometeorology*, 3:660–687.

Dumont, D., Gratton, Y., and Arbetter, T. (2009). Modeling the dynamics of the north water polynya ice bridge. *Journal of Physical Oceanography*, 39:1448–1461.

Dupont, F., Higginson, S., Bourdallé-Badie, R., Lu, Y., Roy, F., Smith, G., Lemieux, J.-F., Garric, G., and Davidson, F. (2015). A high-resolution ocean and sea-ice modelling system for the arctic and north atlantic oceans. *Geosci. Model Dev.*, 8:1577–1594.

Ferry, N., Greiner, E., Garric, G., Penduff, T., Treiguier, A.-M., and Reverdin, G. (2008). Glorys-1 reference manual for stream 1 (2002 - 2007), glorys project report. *GLORYS project report*.

Fichefet, T. and Morales-Maqueda, M. (1997). Sensitivity of a global sea ice model to the treatment of ice thermodynamics and dynamics. *J. Geophy. Res.*, 102:12609–12646.

Flato, G. and Hibler, W. (1995). Ridging and strength is modeling the thickness distribution of arctic sea ice. *Journal of Geophysical Research: Oceans*, 100(C9):18611–18626.

Goosse, H. and Fichefet, T. (1999). Importance of ice-ocean interactions for the global ocean circulation: a model study. *J. Geophy. Res.*, 104:23337–23355.

Hibler, W. (1979). A dynamic-thermodynamic sea ice model. *Journal of Physical Oceanography*, 9:815–846.

Holland, D., Mysak, L., Manak, D., and Oberhuber, J. (1993). Sensitivity study of a dynamic thermodynamic sea ice model. *Journal of Geophysical Research: Oceans*, 98.

Holland, M., Bitz, C., Hunke, E., Lipscomb, W., and Schramm, J. (2006a). Influence of the sea ice thickness distribution on polar climate in ccdm3. *J. Clim.*, 19:2398–2414.

Howell, S., Brady, M., Derkens, C., and Kelly, R. (2016). Recent changes in the sea ice area flux through the beaufort sea during the summer. *Journal of Geophysical Research: Oceans*, 121:2659–2672.

Hu, X. and Myers, P. (2014). Changes to the canadian arctic archipelago sea ice and freshwater fluxes in the twenty-first century under the intergovernmental panel on climate change a1b climate scenario. *Atmosphere-Ocean*, 52(4):331–350.

Hu, X., Myers, P., and Lu, Y. (2019). Pacific water pathways in the arctic ocean and beaufort gyre in two simulations with different horizontal resolution. *Journal of Geophysical Research: Oceans*, 124:6414–6432.

Hu, X., Sun, J., Chan, T., and Myers, P. (2018). Thermodynamic and dynamic ice thickness contributions on the canadian arctic archipelago in nemo-lim2 numerical simulations. *The Cryosphere*, 12:1233–1247.

Hunke, E. (2010). Thickness sensitivities in the cice sea ice model. *Ocean Modelling*, 34:137–149.

Hunke, E. and Dukowicz, J. (1997). An elastic-viscous-plastic model for sea ice dynamics. *Journal of Physical Oceanography*, 27:1849–1867.

Ingram, R., Bácle, J., Barber, D., Gratton, Y., and Melling, H. (2002). An overview of physical processes in the north water.

Kim, J., Hunke, E., and Lipscomb, W. (2006). Sensitivity analysis and parameter tuning scheme for global sea-ice modeling. *Ocean Modelling*, 14:61–80.

Kurtz, N. and Harbeck, J. (2017). Cryosat-1 level-4 sea ice elevation, freeboard, and thickness, version 1. rdeft4.

Kwok, R. (2005). Variability of nares strait ice flux. *Journal of Geophysical Research Letters*, 32.

Kwok, R. and Rothrock, D. (2009). Decline in artic sea ice thickness from submarine and icesat records: 1958-2008. *Geophysical Research Letters*, 36(L15501).

Kwok, R., Spreen, G., and Pang, S. (2013). Arctic sea ice circulation and drift speed: decadal trends and ocean currents. *Journal of Geophysical Research: Oceans*, 118:2408–2425.

Kwon, M. and Lee, H. (2016). The effect of tides on the volume of sea ice in the arctic ocean. *Ocean Science Journal*, 51:183–194.

Lee, C., Curry, B., Petrie, B., Azetsu-Scott, K., and Gobat, J. (2014). Arctic outflow west of greenland: Mass and freshwater fluxes at davis strait.

Madec, G. (2008). Nemo ocean engine. *Note du Pole de modélisation*, (27).

Madec, G. and the NEMO System Team (2016). Nemo ocean engine. *Scientific Notes of Climate Modelling Center*, 27:1288–1619.

Massonnet, F., Barthélemy, A., Worou, K., Fichefet, T., Vancoppenolle, M., Rousset, C., and Moreno-Chamarro, E. (2019). On the discretization of the ice thickness distribution in the nemo3.6-lim3 global ocean-sea ice model. *Geosci. Model Dev.*, 12:3745–3758.

McGeehan, T. and Maslowski, W. (2012). Evaluation and control mechansims of volume and freshwater export through the canadian arctic archipelago in a high-resolution pan-arcitc ice-ocean model. *Journal of Geophysical Research*, 117(C00D14).

Mellor, G. and Hakkinen, S. (1994). A review of coupled ice-ocean models in the polar oceans and their role in shaping the global environment. *Geophysical Monograph, American Geophysical Union*, 85:21–31.

Melsheimer, C. and Spreen, G. (2019). Amsr2 asi sea ice concentration data, arctic, version 5.4 (netcdf) (july 2012 - december 2018). *PANGAEA*.

Melsheimer, C. and Spreen, G. (2020). Amsr-e asi sea ice concentration data, arctic version 5.4 (netcdf) (june 2002 - september 2011). *PANGAEA*.

Moreno-Chamarro, E., Ortega, P., and Massonnet, F. (2020). Impact of the ice thickness distribution discretization on the sea ice concentration variability in the nemo3.6-lim3 global ocean-sea ice model. *Geoscientific Model Development*, 13:4773–4787.

Rousset, C., Vancoppenolle, M., Madec, G., Fichefet, T., Flavoni, S., Barthélemy, A., Benshila, R., Chanut, J., Levy, C., Masson, S., and Vivier, F. (2015). The louvain-la-neuve sea ice model lim3.6: global and regional capabilities. *Geosci. Model Dev.*, 8:2991–3005.

Shine, K. and Henderson-Sellers, A. (1985). The sensitivity of a thermodynamic sea ice model to changes in surface albedo parameterization. *J. Geophy. Res.*, 90:2243–2250.

Smith, G., Roy, F., Mann, P., Dupont, F., Brasnett, B., Lemieux, J.-F., Laroche, S., and Bélair, S. (2014). A new atmospheric dataset for forcing ice-ocean models: Evaluation of reforecasts using the canadian global deterministic prediction system. *Q. J. Roy. Meteor. Soc.*, 140:881–894.

Sou, T. and Flato, G. (2009). Sea ice in the canadian arctic archipelago: Modelling the past (1950-2004) and future (2041-2060). *Journal of Climate*, 22:2181–2198.

Spreen, G., de Steur, L., Divine, D., Gerland, S., Hansen, E., and Kwok, R. (2020). Arctic sea ice volume export through fram strait from 1992 to 2014. *Journal of Geophysical Research: Oceans*, 125.

Spreen, G., Kaleschke, L., and Heygster, G. (2008). Sea ice remote sensing using amsr-e 89 ghz channels. *J. Geophys. Res.*, 113(CO2S03).

Stroeve, J., Holland, M., Meier, W., Scambos, T., and Serreze, M. (2007). Arctic sea ice decline: Faster than forecast. *Geophysical Research Letters*, 34(L09501).

Thorndike, A., Rothrock, D., Maykut, G., and Colony, R. (1975). The thickness distribution of sea ice. *J. Geophys. Res.*, 80(33):4501–4513.

Travers, C. (2012). Quantifying sea-ice volume flux using moored instrumentation in the bering strait.

Tremblay, L.-B. and Hakkinen, M. (2007). Estimating the sea-ice compressive strength from satellite derived sea-ice drift and ncep reanalysis data. *Journal of Physical Oceanography*, 36:2165–2172.

Vancoppenolle, M., Fichefet, T., Goosse, H., Bouillon, S., Madec, G., and Maqueda, M. A. M. (2009). Simulating the mass balance and salinity of arctic and antarctic sea ice. 1. model description and validation. *Ocean Modelling*, 27(1):33–53.

Vincent, R. (2019). A study of the north water polynya ice arch using four decades of satellite data. *Science Reports*, 9(20278).

Wang, Q., Ilicak, M., Gerdes, R., Drange, H., Aksenov, Y., Bailey, D. A., Bentsen, M., Biastoch, A., Bozec, A., Bóning, C., Cassou, C., Chassignet, E., Coward, A., Curry, B., Danabasoglu, G., Danilov, S., Fernandez, E., Fogli, P., Fujii, Y., Griffies, S., Iovino, D., Jahn, A., Jung, T., Large, W., Lee, C., Lique, C., Lu, J., Masina, S., Nurser, A., Rabe, B., Roth, C., Mélina, D., Samuels, B., Spence, P., Tsujino, H., Valcke, S., Voldoire, A., Wang, X., and Yeager, S. (2016). An assessment of the arctic ocean in a suite of 1239 interannual core-(2) simulations. part 1. sea ice and solid freshwater. *Ocean Modelling*, 99:110–132.

Yao, T. and Tang, C. (2003). The formation and maintenance of the north water polynya. *Atmosphere-Ocean*, 4(3):187–201.

Zhang, J. (2020). Sea ice properties in high-resolution sea ice models. *Journal of Geophysical Research: Oceans*, 126.

Chapter 4

Future Climate Scenarios for northern Baffin Bay and the Pikialsorsuaq (North Water Polynya) region

Chapter 4 of this thesis has been submitted for publication as:

Buchart, L., L. Castro de la, Guardia, Y. Xu, N. Ridenour, J.M. Marson, I. Deschepper, A.K. Hamilton, N. Grivault, and P.G. Myers (2020): Future Climate Scenarios for northern Baffin Bay and the Pikialsorsuaq (North Water Polynya) region, *Atmosphere-Ocean*.

P.G. Myers deisgned and carried out experiments. I was responsible for analyzing the physical variabiles and writing the Introduction, Methods, and Conclusion. Myself and L. Castro de la Guardia wrote the analysis and discussion. L. Castro de la Guardia carried out analysis and of the biogeochemical properties and wrote the results and discussion on this analysis. J.M. Marson and N. Ridenour provided information and analysis on the runoff product used. N. Grivault provided code for analysis. Y. Xu, I. Deschepper, and A.K. Hamilton provided insight and edits on the manuscript. P.G. Myers provided further guidance and edits.

Abstract

Northern Baffin Bay is distinct due to the presence of the North Water Polynya, a region referred to as ‘Pikialasorsuaq’ by Inuit in Greenland and ‘Sarvarjuaq’ by Inuit in Canada. Surrounding communities rely on the polynya as hunting and shipping grounds for much of the year due to its lower sea ice concentration and high primary productivity, however, Arctic warming threatens the dynamics of the region by altering the sea ice cycle, oceanic heat content, and freshwater input. The aim of this study is to examine the future of northern Baffin Bay and Pikialasorsuaq under various climate warming scenarios using the Nucleus for Modelling of the Ocean (NEMO) engine, coupled to the Louvain-la-Neuve (LIM2) sea ice model. Five experiments were run on a $1/4°$ resolution Arctic and Northern Hemispheric Atlantic (ANHA4) configuration over the period 1981-2070 forced by a range of global climate models. By 2070 there is a significant decrease in sea ice thickness and concentration, with an overall warming and salinity increase in the upper 500m of the water column. Increased freshwater input from melting Greenland glaciers results in a more muted salinity increase in the top 50m, while deeper waters are impacted by increased penetration of warm, saline Atlantic Water into Baffin Bay through Davis Strait. These physical changes impact the formation of the polynya in the future: The polynya is expected to continue to forming on the eastern side near Greenland through mixing of warm Atlantic Waters to the surface, while the western side near Ellesmere Island has an increased ice area flux through Nares Strait and increased stratification. Additionally, there is a shallowing of mixed layer depth and increase in density stratification under the greatest warming scenarios. Implications to biogeochemical properties include a 0.5% decrease in total alkalinity, a 3.4% decreased in dissolved oxygen concentration but no net change in annual phytoplankton primary production. However, there are large changes in the phytoplankton bloom dynamics, including a 50% decrease in the autumn bloom and a 20-day advance in the spring bloom. Overall, our study suggests significant oceanographic changes which could lead to a loss of the recurrent polynya in its historical state, and shifts in primary production which could have, as yet uncertain, consequences for the food web and higher trophic levels.

4.1 Introduction

Northern Baffin Bay is a unique region due to the presence of a polynya, known as 'Pikialasorsuaq' by the Greenlandic and 'Sarvarjuaq' by Inuit in Canada (otherwise known as the North Water Polynya or NOW), which is formally defined as the area between Ellesmere Island and Greenland, spanning $76^\circ\,\mathrm{N} - 78.5^\circ\,\mathrm{N}$ (Ingram et al., 2002). A polynya is a region of light ice cover or open water which is surrounded by pack ice (Melling et al., 2002). The North Water, named by the whalers who used the polynya as a hunting ground, is one of the largest reoccurring polynyas in the Arctic (Dunbar and Dunbar, 1972; Ingram et al., 2002). Local Greenlandic communities rely on the region as a hunting, fishing, and transportation ground for much of the year due to the relatively low ice cover (Ingram et al., 2002). Greater light penetration and mixing make Pikialasorsuaq a region of high phytoplankton primary production that supports a number of marine mammals and birds (Mei et al., 2003; Melling et al., 2002; Stirling, 1997; Tang et al., 2004). Maxwell (1981) describes the climate of the NOW region as unique to the Canadian Arctic islands and is often impacted by low pressure systems which move north from the Davis Strait region, stop, and dissipate in northern Baffin Bay bringing greater than normal precipitation. Pikialasorsuaq has a more maritime climate compared to the adjacent Canadian Arctic Archipelago (CAA). The maritime climate is observed in the winter mean temperature: adjacent to the polynya temperature rises to $-22^\circ\,\mathrm{C}$, over northern Baffin Bay the mean temperature ranges between $-33^\circ\,\mathrm{C}$ and $-36^\circ\,\mathrm{C}$. Pikialasorsuaq and adjacent regions are influenced by the circulation of Baffin Bay and the two main water masses: Atlantic and Arctic Waters.

Baffin Bay is connected to the Arctic Ocean through three shallow straits; Lancaster Sound, Jones Sound, and Smith Sound, and Davis Strait connects the bay to the Labrador Sea. Davis Strait provides the largest volume and freshwater flux to Baffin Bay, followed by Lancaster Sound and Nares Strait (Curry et al., 2011, 2014; McGeehan and Maslowski, 2012; Münchow, 2016; Münchow et al., 2015). Baffin Bay's surface circulation (Figure 1) is the product of wind stress over the region (Yao and Tang, 2003). The West Greenland Current (WGC) and Baffin Island Current (BIC) are the two main currents within Baffin Bay (Curry et al., 2011). Circulation, described by Melling et al. (2002) is summarized in the following sentences. At depth, the WGC flows northward, carrying warm, saline Irminger Water along the coast of Greenland to approximately $75^\circ\,\mathrm{N}$, where it crosses northern Baffin Bay and joins the southward flowing, BIC which is cool and fresh. This pattern is observed at both the surface and at 500 m. Therefore, water masses at the surface and around 500 m moving along the western Greenland coast play significant roles in bringing heat and salt to northern Baffin Bay. The vertical structure is largely controlled by salinity, with cold, low salinity waters at the surface and warm, more saline waters at depth. Northern Baffin Bay is highly stratified and the mixed layer depth (MLD) is not uniform (Melling et al., 2002). Deeper MLDs are found on the eastern side of the region because the stratification is weaker than the western side, where Arctic Waters occupy the majority of the water column (Melling et al., 2002). A reduced ice cover in the polynya, decreases surface stratification and promotes mixing of heat and nutrients to the surface during winter, when the polynya is present (Melling et al., 2002).

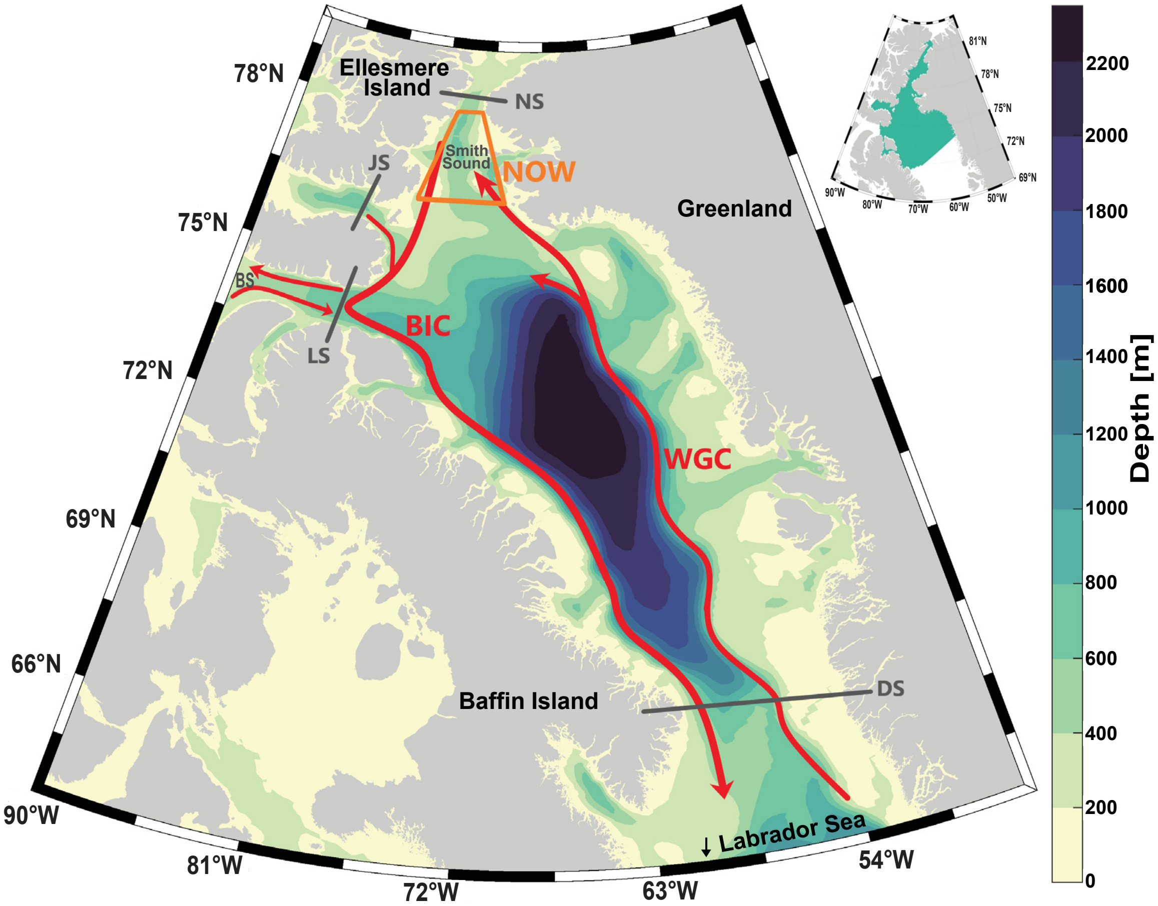

Figure 4.1: a) Baffin Bay general, surface circulation. WGC - West Greenland Current, BIC - Baffin Island Current, DS - Davis Strait, LS - Lancaster Sound, BS - Barrow Strait, JS - Jones Sound, NS - Nares Strait, NOW - Pikialasorsuaq (North Water Polynya). Note that Barrow Strait is formally located to the west of the schematic in western Lancaster Sound. The inset figure at top right is the model averaging mask. The domain extends farther north than the circulation schematic to encompass the length of Nares Strait.

Pikialasorsuaq is formed when an ice bridge develops in Nares Strait during late fall and early winter. The formation of this bridge is dependent on the multi-year ice entering the channel from the Arctic Ocean (Dumont et al., 2009; Ingram et al., 2002). Pikialasorsuaq differs in shape and size from year to year, with changes determined by the stability of the ice bridge (Vincent, 2019). Ice growth rates can exceed 1.2 m/month in some regions of Pikialasorsuaq and contributes significantly to the large surface heat fluxes in the region which are proposed to maintain the polynya (Vincent, 2019; Yao and Tang, 2003). Upwelling generated by Ekman transport off the coast of Greenland is thought to aid in maintaining the eastern part of the polynya, particularly during the winter (Melling et al., 2002). In the early summer, when the ice bridge breaks down, sea ice floes move south through Nares Strait, dissolving the polynya (Vincent, 2019).

Impacts of climate change on northern Baffin Bay are predicted to be large due to the adjacent Greenland Ice Sheet and glaciers of Baffin and Ellesmere islands inputting greater amounts of freshwater to the upper ocean layers (Dukhovskoy et al., 2016). A passive tracer experiment carried out from 2012 to 2016 by Dukhovskoy et al. (2019) predicts a salinity decrease of 0.2 near the coast of Greenland. The salinity decrease is even larger, when only considering the Baffin Bay interior waters in the upper 150 m. Additionally, the Greenland freshwater flux is expected to create negative salinity trends in the upper $300-500$ m of the subpolar basins, while no negative trend is observed below 500 m depth (Dukhovskoy et al., 2019). This study also highlighted the uncertainty of the depth that Greenland freshwater will mix to in Baffin Bay. The freshwater contribution from Greenland and adjacent regions into Baffin Bay is approximately $514\,\mathrm{km}^3/\mathrm{yr}$ for a time period of 2000 - 2010, this estimate increases to $563\,\mathrm{km}^3/\mathrm{yr}$ from 2007 - 2016 (Bamber et al., 2018). The freshwater flux associated with the Greenland Ice Sheet is expected to continue increasing in the future. A modelling study by Dunlap and Tang (2006) found that inflow to Baffin Bay through Davis Strait is influenced by the inflow from the CAA and transports in the Labrador Sea. Increased runoff from Greenland as a result of climatic warming is predicted to generate a positive feedback in Baffin Bay which raises isotherms, increasing heat content on the western Greenland shelves, and potentially leading to enhanced Greenland melt and stronger gyre circulation (Castro de la Guardia et al., 2015). Consequences of climatic warming on surface winds and precipitation are of greater uncertainty. Coupled climate models predict a total freshwater gain of about 50 % in Baffin Bay (Thomas et al., 2015).

A changing ice regime in northern Baffin Bay has been found to decrease both the mean ice thickness and duration the ice bridge forms in Nares Strait (Vincent, 2019). Vincent (2019) found that from 1979 to 2019 the ice bridge was decreasing in duration by 2.1days/year. Baffin Bay summer ice extent has decreased at a rate of $-16 \pm 4.1\,\%/\mathrm{decade}$ (Tivy et al., 2011). A possible result of continued climatic warming would be an increase of the areal extent of ice inside the polynya region in the near-future, due to an increased duration of ice inflow from the Arctic through Nares Strait. However, as the ice continues to thin, this will also act to decrease the duration of ice cover over the entire region.

In this study, we look at the impacts of climate change on northern Baffin Bay and the potential response of temperature, salinity, sea ice, and biogeochemical variables in the region. A model and experiment description is provided in section 2, results are presented in section 3, the impact of these changes and influence that they could have on the polynya are discussed in section 4, finally, section 5 gives a brief conclusion.

4.2 Model Description and Experiment Setup

4.2.1 Ocean-Ice Model

The ocean model used is the NEMO (Nucleus for European Modelling of the Ocean) numerical framework version 3.6 (Madec, 2008). NEMO is a primitive equation model developed from the Océan PArallélisé (OPA) ocean circulation model version 8.2 (Madec and the NEMO System Team, 2016). Equations of motion are written in curvilinear, orthogonal coordinates (Madec and the NEMO System Team, 2016). No salinity or temperature restoring is applied. Vertical mixing is parameterized using a TKE (turbulent kinetic energy) closure model (Madec and the NEMO System Team, 2016). Lateral mixing in the model uses a bi-laplacian operator with an eddy viscosity of $1.5 \times 10^{11}\,\mathrm{m}^4/s$. The baroclinic timestep is 1080s and a barotropic timestep of 6s (180 iterations between each baroclinic timestep). Tidal forcing is included, which requires the NEMO nonlinear surface and variable volume formulations to be used. Tidal forcing includes nine constituents: K1, K2, M2, M4, N2, O1, P1, Q1, and S2. The LIM2 sea ice model (Fichefet and Morales-Maqueda, 1997) is a dynamic-thermodynamic model which is composed of one snow layer and two ice layers (Timmermann et al., 2005). LIM2 uses a C-grid elastic-viscous-plastic (EVP) rheology (Hunke and Dukowicz, 1997). The sea ice model is coupled to the ocean model at every time-step. A more comprehensive description of the model configuration can be found in Garcia-Quintana et al. (2019). The Biogeochemistry with Light Iron Nutrient and Gas model (Galbraith et al., 2015, BLING) module is used, which has six prognostic variables; dissolved phosphate, dissolved organic phosphate, iron, oxygen, dissolved carbon, and total alkalinity.

4.2.2 Configuration

Experiments are ran on the ANHA4 (Arctic and Northern Hemisphere Atlantic) configuration which using a tri-polar grid with a $1/4^\circ$ resolution. The mesh for ANHA4 is extracted from the $1/4^\circ$ global tripolar grid, ORCA025 (Barnier et al., 2007). This gives a resolution of $\sim 10\,\mathrm{km}$ in Baffin Bay. The ANHA4 configuration encompasses the entire Arctic region with two open boundaries, one just south of Bering Strait and the other located at $20^\circ S$ in the Atlantic Ocean. The ANHA4 configuration has 50 vertical levels. Layer thickness smoothly varies from $1.05\,\mathrm{m}$ at the surface to $453.13\,\mathrm{m}$ in the bottom layer.

4.2.3 Initial Conditions

Experiments are initialized on the first January 1981 using climatological ocean temperature and salinity from the Polar Science Center Hydrographic Climatology (Steele et al., 2001, PHC 3.0). Initial conditions are such that the ocean is initially at rest, sea ice is initially 3 m thick in all grid-cells where the ocean temperature is close to the freezing temperature (following the UNESCO (United Nations Educational, Scientific and Cultural Organization) formulation to find the freezing temperature based off of ocean temperature and salinity of Steele et al. (2001)).

Biological fields for BLING were initialized with both observed climatologies and model output. Dissolved oxygen and inorganic phosphate fields come from World Ocean Atlas 2013 Version 2 climatologies (WOA13; Garcia et al. (2014a); Garcia et al. (2014b)). Dissolved iron and organic phosphate fields come from model output of the Geophysical Fluid Dynamics Laboratory (GFDL) Earth System Model version 2 (ESM2M) coupled with BLING version 0. The ESM2M simulation is a global configuration at 1° nominal resolution that was run for 100 years. Climatologies used were generated from the final 20 years. The initial conditions of total alkalinity and dissolved inor-

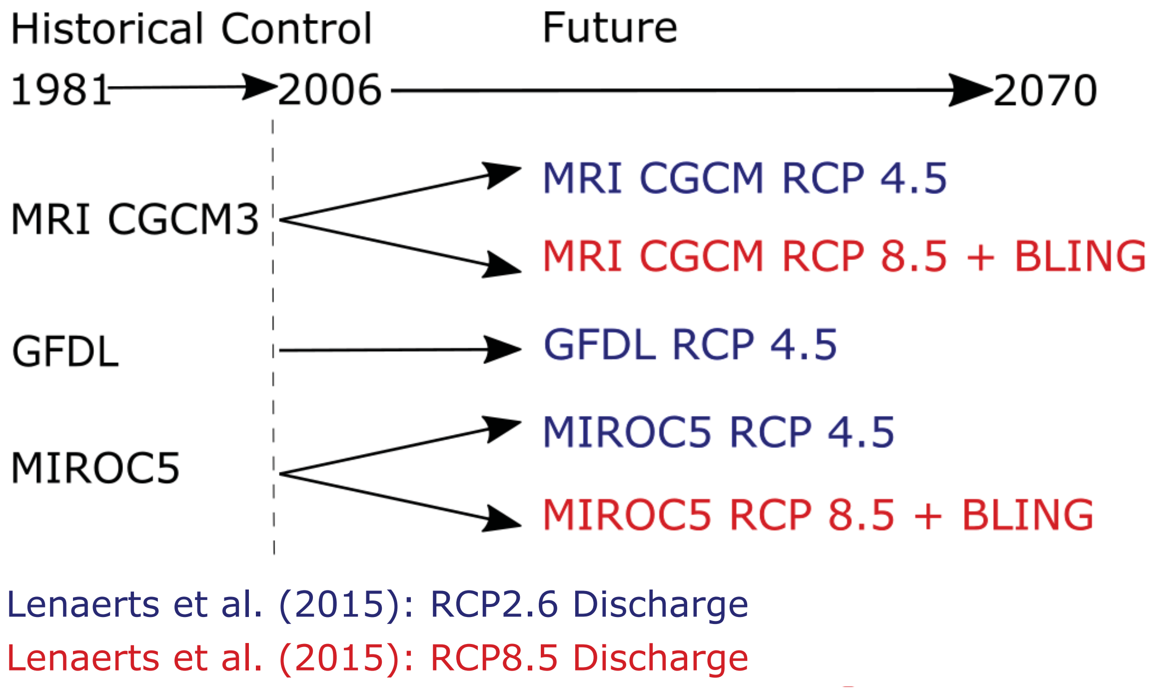

Figure 4.2: Climate ensemble schematic. Left three experiments represent the historical control which are run from 1981-2005, the five climate experiments are run from the start of 2006 to the end of 2070. Red text represents the RCP8.5 which also include the BLING module. RCP8.5 runs include Lenaerts et al. (2015) RCP8.5 Greenland discharge. Blue text represents the RCP4.5 experiments which include the Lenaerts et al. (2015) RCP2.6 Greenland discharge. The RCP4.5 experiments do not include the BLING module.

ganic carbon (DIC) derived from GLobal Ocean Data Analysis Project version2 (GLODAPv2; Key et al. (2015), Lauvset et al. (2016), Olsen et al. (2016)). DIC initial conditions are normalized to the simulation start year (1981) to account for anthropogenic carbon using DeVries (2014) estimates. All fields where remapped onto the ANHA4 grid with units of mol/m^3.

4.2.4 Climate Ensemble

The climate ensemble consists of five members. Each forcing (including atmospheric, initial, and boundary conditions) are selected from the Coupled Model Inter-comparison Project 5 (CMIP5). Temperature, precipitation, and wind were bias corrected as discussed in Stadnyk et al. (2019) and Braun et al. (2020). The following information on the climate ensemble is summarized in Figure 2. Three different forcings are used: the Meteorological Research Institute (MRI CGCM3; Yukimoto and Coauthors (2012)), the Geophysical Fluid Dynamics Laboratory (GFDL; Donner and Coauthors (2011)), and the Model for Interdisciplinary Research on Climate version 5 (MIROC5; Watanabe and Coauthors (2010)). Forcing fields were interpolated onto the NEMO model grid using NEMO's on-the-fly interpolation function (Madec, 2008). The five experiments come from three moderate emission RCP4.5 scenarios (MRI CGCM3 RCP4.5, MIROC5 RCP4.5, and GFDL

RCP4.5) and two business-as-usual RCP8.5 scenarios (MRI CGCM3 RCP8.5 and MIROC5 RCP8.5). The ensemble aims to encompass a wide range of future temperature and precipitation changes, and their associated uncertainty. Each experiment is divided into two parts: a historical control portion extending from 1981-2005, and a future period extending from 2006-2070. The forcings do not include Greenland or river runoff, so an external runoff product is considered. Atlantic river runoff was taken from the Canadian Centre for Climate Modelling and Analysis (CCCMA) CanESM2 model (Arora et al., 2011) for the southern regions. Arctic-HYPE (Stadnyk et al., 2020) was used for Hudson Bay and the Arctic. Greenland runoff comes from Lenaerts et al. (2015) and has two discharge scenarios: RCP2.6 and RCP8.5. The historical portion (prior to 2006) of each experiment utilize the historical RCP2.6 Greenland discharge. The future portion of each experiment uses discharge that corresponds to the forcing's RCP scenario: RCP4.5 experiments use the RCP2.6 Greenland discharge, while RCP8.5 experiments use the RCP8.5 Greenland discharge. All discharge fields were remapped onto the ANHA4 grid. Due to the additional computation cost, the BLING module is coupled only to the two RCP8.5 experiments to examine changes to the biogeochemical properties of northern Baffin Bay for the buisness-as-usual emission scenario.

Linear regression of the ensemble's timeseries are used to interpret future changes. Winter values correspond to December-January-February averages, spring values correspond to March-April-May, summer values correspond to June-July-August, and fall corresponds to September-October-November. Three different averaging periods are used to analyze long-term changes: a historical control, 1981-2005, near-future period, 2030-2049, and far-future period, 2050-2070. Winter, and spring means are used as these are the two seasons when the polynya is present. However, key biogeochemical variables are analyzed for spring and fall as well due to their differing seasons of importance and response to a changing ice regime in the region. A northern Baffin Bay averaging mask (inset Figure 1) is used for all spatial means. Henceforth, the masked area is refered to as northern Baffin Bay. The orange polygon in Figure 1 references the polynya or Pikialasorsuaq. Adjacent regions are refered to as the polynya region.

Analysis of forcing components

The ensemble mean surface air temperature (Figure 4.3c) in the historical control period (1981-2005) is $-13.1 \pm 0.6°$C, increasing to $-11.5 \pm 0.7°$C in the near-future (2030-2049) period and further increases to $-9.00 \pm 0.6°$C in the far-future (2050-2070) period. The mean spring temperature of the historical control period is $-18.2 \pm 0.8°$C, increases to $-18.0 \pm 0.7°$C in the near-future period, and further increases to $-16.4 \pm 0.7°$C in the far-future period. Winter temperatures experience the greatest change, increasing from a historical control mean of $-26.6 \pm 1.2°$C to $-24.3 \pm 1.3°$C in the near-future, and $-20.2 \pm 1.0°$C in the far-future period. The two RCP8.5 experiments have the greatest warming. However, the GFDL RCP4.5 has a similar warming to these two experiments. There is a noticable ($\sim 2°$C) magnitude difference in the surface air temperature of the far-future period between the RCP8.5 experiments, the GFDL RCP4.5 experiment and MRI-CGCM3 RCP4.5 and MIROC3 RCP4.5. Annual precipitation rates (Figure 4.3b) also grow from a historical control mean of 0.26 ± 0.02m/year to 0.32 ± 0.03m/year in the far-future. This represents a 23% increase in annual precipitation. The spring season experiences a smaller increase (7%) and winter experiences a larger increases (54%) from the historical period to the far-future. Both the oceanic and ice surfaces in northern Baffin Bay receive increased amount of heat and freshwater from the atmosphere. Finally, wind speeds at 10 m above the ground surface (not shown) remain relatively constant, with a minimal increase through to the future period. Mean spring and winter wind speeds are found to increase by ~ 0.2m/s over the study period. Additionally, the GFDL RCP4.5 experiment has the strongest winds over the course of the study period.

The remapped Greenland liquid discharge (Figure 4.3a) has a step-like increase in the transition from the historical period (1981 - 2005) to the future (2006-2070) RCP8.5 forcing. In the historical period, all experiments use the RCP2.6 Greenland discharge of Lenaerts et al. (2015). In 2006, the RCP4.5 experiments continue to use the RCP2.6 Greenland discharge and the RCP8.5 experiments use the RCP8.5 discharge of Lenaerts et al. (2015). When comparing the remapped Lenaerts et al. (2015) to Bamber et al. (2018), over a period of 1992 to 2017, it is found that RCP2.6 discharge better matches Bamber et al. (2018). The RCP8.5 experiment overestimates (from 2006 to 2017) by $\sim 2300\text{km}^3/\text{yr}$. In the future period, as temperatures warm and melting increases, the RCP8.5 Greenland discharge may be more realistic. In the the historical control period, the RCP2.6 discharge was selected for all experiments as it best matches discharge values of recent decades. Thus, the RCP2.6 and the RCP8.5 Greenland discharge provide an upper and lower bound of future freshwater and the ensemble mean a more realistic discharge value than either of the two forcings. Therefore, RCP4.5 experiments will have more realistic surface freshwater contents early in the future period, and may have too little by the late-future (2050-2070) period while the RCP8.5 will have a too great surface freshwater content at the beginning of the future period and be more realistic by the far-future. The solid discharge is approximately constant at $\sim 600\text{km}^3/\text{yr}$ from 1981 through to 2070.

4.3 Results

4.3.1 Transports into Baffin Bay

Model volume and freshwater fluxes (computed from a reference salinity of 34.8) are compared to observations at three gateways in Baffin Bay: Barrow (Figure 4.4a-b), Davis (Figure 4.4c-d), and Nares Straits (Figure 4.4e-f). The ensemble produces a larger than observed volume flux at the three gateways, though freshwater fluxes match better observational means. Positive values indicate flow which is directed into Baffin Bay. At Barrow Strait, model output is compared to observed fluxes obtained from Petersen et al. (2012) which extend from 1999-2010. The observed mean is 0.5 ± 0.2 Sv and the ensemble mean flux is 1.2 ± 0.1 Sv. The observed freshwater flux is 34.2 ± 10.4 mSv and the ensemble mean over this period is 46.4 ± 4.5 mSv. At Davis Strait, the ensemble is compared to observations obtained from Curry et al. (2014), extending from 2005-2013. The observed volume flux and freshwater flux over this period are -1.6 ± 0.2 Sv and -94.4 ± 11.6 mSv, compared to the

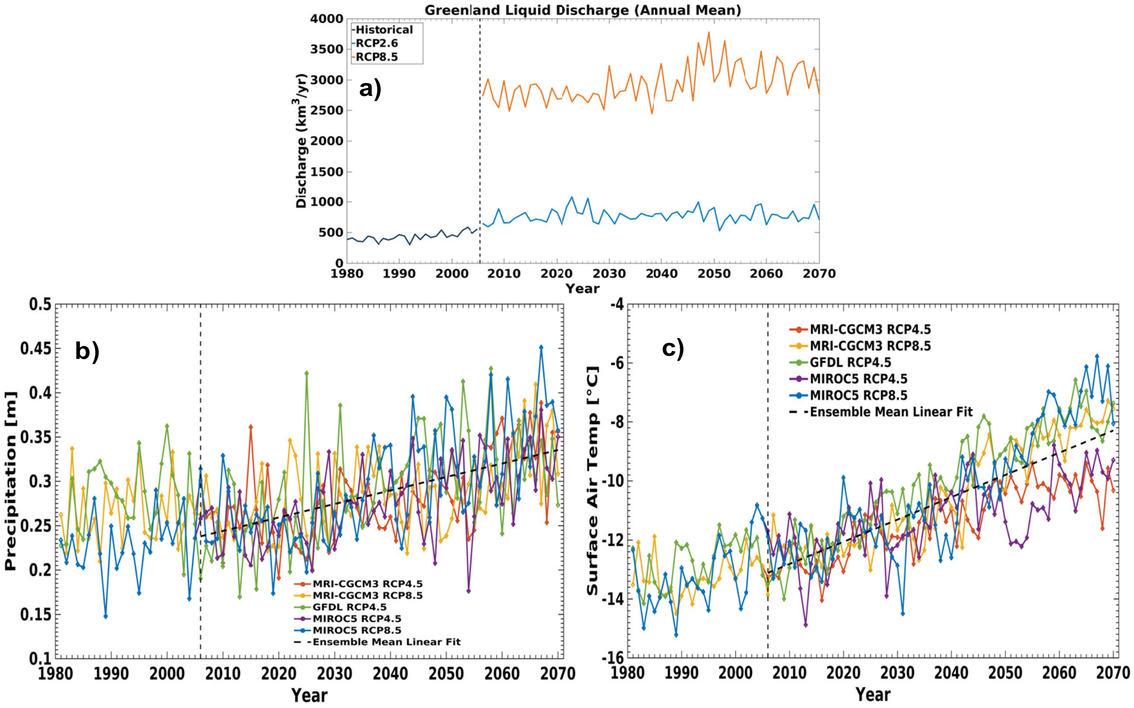

Figure 4.3: Model forcing timeseries. a) Greenland liquid discharge [km^3/yr] from Lenaerts et al. (2015). b) Annual mean precipitation [m] and c) Annual mean 2 m air temperature [°C] averaged over the North Water Polynya mask shown in the inset of Figure 1.

ensemble mean of -2.5 ± 0.2 Sv and -69.0 ± 5.8 mSv, respectively. At Nares Strait, the ensemble is compared to observations from Münchow (2016). Observations are broken into two periods; 2003-2006 and 2007-2009 and annual averages are taken. The observed 2003-2006 volume and freshwater flux means are; 0.7 ± 0.1 Sv and 32.1 ± 4.2 mSv, respectively. The ensemble produces a larger volume flux (1.5 ± 0.1 Sv) and a smaller freshwater flux (17.9 ± 1.2 mSv). Over the 2007-2009 period, observations yield a mean volume flux of 1.1 ± 0.2 Sv and freshwater flux of 55.6 ± 8.7 mSv. The ensemble over this period yields a similar volume flux (1.3 ± 0.0 Sv) and a smaller freshwater flux (16.9 ± 0.6 mSv).

When the ANHA4 configuration was forced with atmospheric reanalysis data, such as is in Grivault et al. (2018), hindcast experiments behave similar to the observed. The climate experiments used here do not match observations as well as these hindcast experiments due to the use climate forcings and not reanalysis data. At the three straits analyzed here, the Grivault et al. (2018) experiments compared better to observed, mean volume and freshwater fluxes than our ensemble. In the context of analyzing future impacts of climatic warming, the ensemble is producing large volume fluxes and slightly smaller than observed freshwater fluxes. We then expect to see larger transports of heat, salt, ice, etc. than observed and the freshwater content to be lower than what would be observed.

Over the full study period, changes in ensemble mean volume and freshwater fluxes through Barrow, Davis, and Nares straits are small compared to changes in other physical variables. The Barrow Strait volume flux decreases from a historical control mean (1981-2005) of 1.4 ± 0.2 Sv to 1.1 ± 0.1 Sv in the near-future (2030-2049) and then increases slightly to 1.2 ± 0.1 Sv in the far-future (2050-2070). The freshwater flux at Barrow Strait is increasing over the course of the study. The historical control mean is 59.8 ± 10.2 mSv and increases to 60.9 ± 4.3 mSv in the near-future and further grows to 70.2 ± 6.4 mSv in the far-future. These results contrast those of Hu and Myers (2014) who used NEMO version 3.1 and LIM2 forced with the Intergovernmental Panel on Climate Change A1B climate scenario to predict changes to Barrow Strait transports over the coming century. Hu and Myers (2014) predicted a decrease in both the volume and freshwater transport, with the volume and freshwater transports decreasing to zero by 2050. The volume and freshwater fluxes entering Baffin Bay through Barrow Strait in the ensemble are not found to change significantly. At Davis Strait the historical control mean volume flux is -3.1 ± 0.4 Sv, and decreases to -2.5 ± 0.2 Sv in the near-future, and remains around the same value at -2.6 ± 0.1 Sv in the far-future. There is significant uncertainty in the future of the Davis Strait volume flux as there is a range of ~ 1.5 Sv between experiments in the far-future period. The Davis Strait freshwater flux changes are small, increasing from -88.8 ± 16.1 mSv in the historical control to -97.5 ± 5.1 mSv in the near-future, and to -102.9 ± 5.0 mSv in the far-future. At Nares Strait, the volume flux remains relatively constant: there is a small decreases from 1.4 ± 0.2 Sv in the historical control to 1.3 ± 0.1 Sv in the near-future and far-future periods was found. The freshwater flux across Nares Strait decreases from 18.0 ± 6.8 mSv in the historical control period to 16.7 ± 2.0 mSv in the near-future and continues to decrease to a far-future mean of 12.0 ± 2.7 mSv. In summary, only the Davis

Strait volume flux is found to change from the historical control period.

4.3.2 Sea Ice

The annual mean (Jan-Dec) ice area and volume flux through Nares Strait (Figure 4.5) are compared to Kwok (2005) estimates, who used RADARSAT imagery to measure annual (Sep-Aug) ice area fluxes and estimate ice volume flux with a constant (4m) ice thickness. Kwok (2005) measured an ice area flux of $33 \times 10^3\,\mathrm{km}^2$ and approximated a volume flux of $\sim 130\,\mathrm{km}^3$. In comparison, the ensemble mean ice area flux through Nares Strait during the historical control period is larger than the observed: $120 \pm 29 \times 10^3\,\mathrm{km}^2$. The flux decreases to $111 \pm 9 \times 10^3\,\mathrm{km}^2$ in the near-future and in the far-future is $103 \pm 11 \times 10^3\,\mathrm{km}^2$. Ensemble values of the area flux are higher than that measured by Kwok (2005), this is likely due to the LIM2 not parameterizing landfast ice which creates a mobile ice pack throughout the year. Thus, the ensemble ice arch is not as stable as would be expected. Kwok (2005) emphasized the importance of the ice arch during the winter and spring seasons in measuring of the area flux and this process is occurring less frequently in the ensemble. Additionally, our flux calculations were taken further south in Nares Strait compared to the section used by Kwok (2005), in which calculations where done adjacent to the Arctic. Grivault et al. (2018) also found that along-channel winds in Nares Strait play a significant role in ice transports, a too great wind may also be driving large ice fluxes. We acknowledge and consider these shortcomings in our predictions for the future state of northern Baffin Bay.

The Nares Strait ice volume flux is found to decrease. The ensemble mean of the historical control is $229 \pm 31\,\mathrm{km}^3$, decreasing to $126 \pm 18 km^3$ in the near-future period and $99 \pm 16\,\mathrm{km}^3$ in the far-future period ($-1.1\mathrm{km}^3/\mathrm{yr}$, $\mathrm{p} < 0.01$). This represents a decrease of 45% between the historical control and near-future and a decrease of 57% between the far-future and historical control.

The ice area flux regression coefficient of the future period (2006-2070) is small and positive: $0.06 \times 10^3\mathrm{km}^2$, ($\mathrm{p} < 0.01$). The sea ice area flux increase is indicative of enhanced ice motion through Nares Strait when other key sea ice indicators (volume flux, thickness, concentration) are decreasing. The decreased late-future mean value is likely a product of a diminishing ice concentration across the region, rather than a smaller amount of ice being forced through the strait. The shape of the timeseries during the future period has two distinct categories: an increasing period from 2006-2040 as ice is pushed more readily through the strait and a decreasing period from 2040-2070 when nearly all ice is gone from the region. An enhanced ice area flux puts the formation of the polynya into question as the increasing ice area flux is indicative of the ice arch not forming as frequently. In the far-future period, when the mean ice area flux is at its lowest, a near complete loss of ice in the region limits any polynya formation.

The correlation between mean ice thickness and ice volume transport across Nares Strait is $\mathrm{r} = 0.81$, ($\mathrm{p} < 0.01$). Over the future period (2006-2070), the area flux is found to slightly increase and thus has a weaker correlation with ice volume at, $\mathrm{r} = 0.40$, ($\mathrm{p} < 0.01$). Ice thickness decrease is the driver for diminishing ice volume fluxes through Nares Strait.

Ensemble mean annual sea ice concentration (Figure 4.6a) is found to decrease over the study

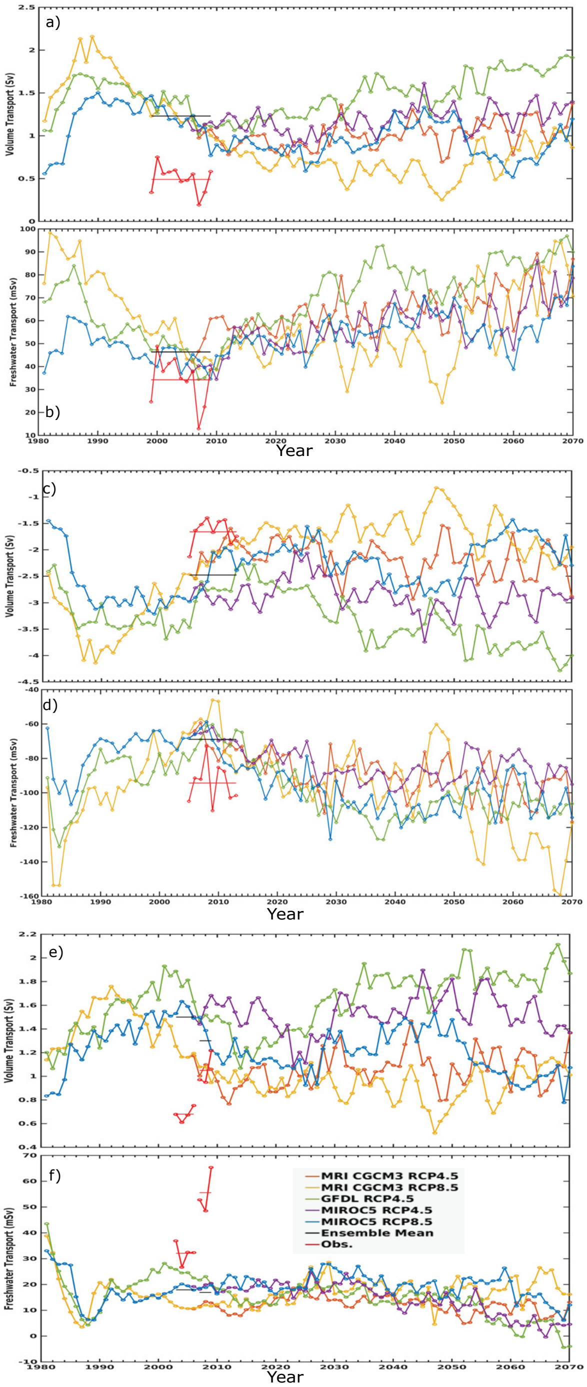

Figure 4.4: Volume [Sv] and freshwater fluxes [mSv]. a) Barrow Strait volume a) and freshwater flux b). Barrow Strait observations in (a-b) are from Petersen et al. (2012). c) Davis Strait volume c) and freshwater flux d). Davis Strait observations in (c-d) are from Curry et al. (2014). Nares Strait volume e) and freshwater flux f). Nares Strait observations in (e-f) are from Münchow (2016). Positive values indicate flow into Baffin Bay.

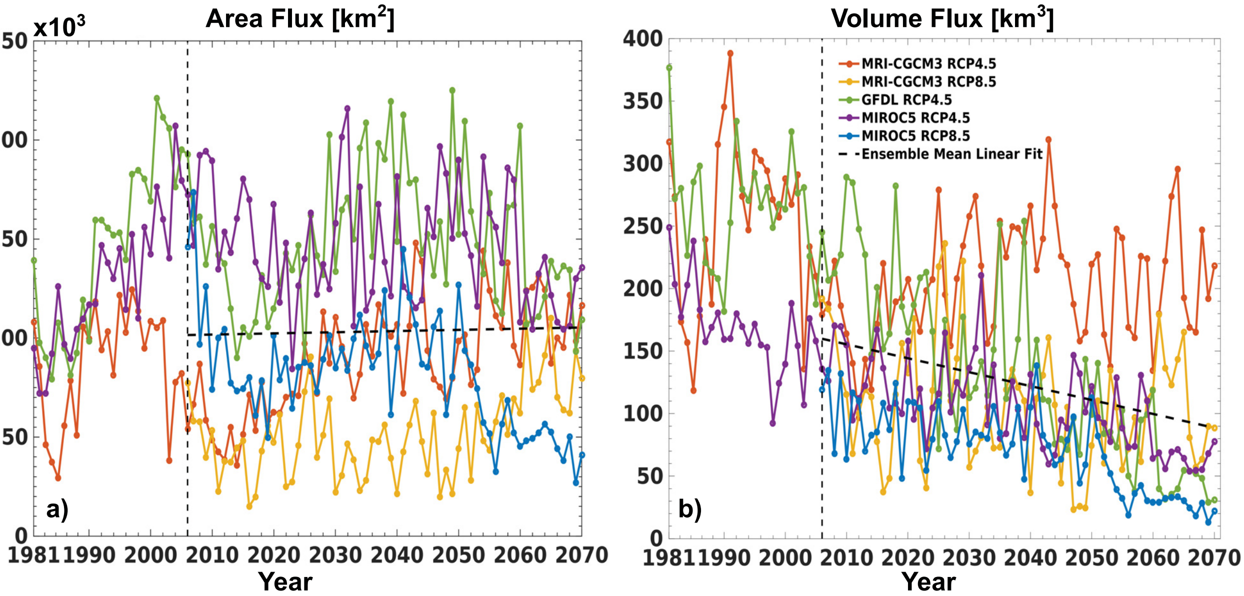

Figure 4.5: Nares Strait annual mean a) ice area flux [km^2] b) ice volume flux [km^3].

period reaching $48 \pm 2\%$ in the far-future. Down from a historical control mean of $67 \pm 5\%$ and a near-future mean of $57 \pm 3\%$. This represents a 15% and 29% loss in annual ice concentration in the near-future and far-future periods, relative to the historical period. Winter concentration (Figure 4.6b) is found to decrease from a historical mean of $94 \pm 1\%$ to $90 \pm 3\%$ (-5%) in the near-future and $79 \pm 4\%$ (-16%) in the far-future. The spring ice concentration (Figure 4.6c) losses are smaller, decreasing from a historical mean of $91 \pm 1\%$ to $89 \pm 1\%$ (-3%) in the near-future and $85 \pm 2\%$ (-7%) in the far-future. Both MRI-CGCM3 experiments have greater ice thickness and concentration compared to other ensemble members throughout the study period. The rate of ice thickness and concentration losses are similar across all members. Ice concentration losses contrast an increasing ice area flux discussed previously. In this context an increasing ice area flux is expected to play a role in the region only in the coming decade or so, though ice concentration losses dominate by the end of the study period.

Tivy et al. (2011) found that ice concentration has decreased by $-8.9 \pm 3.1\,\%/\text{decade}$ when considering the entire Baffin Bay and $-1.0 \pm 5.3\,\%/\text{decade}$ when considering western Baffin Bay for a time period of 1968-2008 (see Tivy et al. (2011) figure 9 for regional comparison to Figure 1 inset here). The ensemble mean annual ice concentration decreases in northern Baffin Bay at a rate of $\sim -3\%/decade(p < 0.01)$ over the time period of 2006 - 2070, over the historical control period (1981-2005) the rate of concentration loss is $-4\,\%/\text{decade}\,(\text{p} < 0.01)$. Both values are smaller than Tivy et al. (2011), but fall within the error of the western Baffin Bay region. The ensemble ice concentration is also compared to the observed AMSR-E and AMSR2 (Spreen et al., 2008, henceforth AMSR) ice concentration over a period of 2003-2019. The observed concentration compares well with the ensemble annual and seasonal means. Over the AMSR observation period the slope of the linear regression was also calculated, however both the ensemble and observed rates of change were not significant $(p > 0.01)$. The winter and spring ensembles had a small, positive slope and the annual slope was small and negative $(-0.04\%/\text{yr})$. The observed rates of change were all negative with the annual rate being $(-0.18\%/yr)$. Over the AMSR period, the ensemble is not capturing the observed rapid ice concentration loss, though the ensemble mean compares well to the observed ice concentration.

The ensemble mean sea ice thickness (Figure 4.6d-f) is found to decrease over the study period. Annual mean thickness in the region is predicted to decrease from a historical control mean (1981-2005) of $1 \pm 0.2\,\text{m}$ to a near-future (2030-2049) mean of $0.67 \pm 0.1\,\text{m}$ and a far-future (2050-2070) mean thickness of $0.47 \pm 0.05\,\text{m}$. Ice thickness decreases by 34% when comparing the historical control to the near-future mean and by 55% when compared to the far-future mean. In the summer and fall (timerseries not shown as the polynya does not occur in these seasons), ice thicknesses of $0 - 0.1\,\text{m}$ are found as early as 2040 in both MIROC5 and GFDL experiments. The winter ice thickness decreases from a historical control mean of $1.26 \pm 0.17\,\text{m}$ to $0.89 \pm 0.08\,\text{m}$ and $0.63 \pm 0.06\,\text{m}$ in the near- and far-future periods, respectively. Spring ice thickness decreases to a mean thickness in the near-future of $1.17 \pm 0.09\,\text{m}$ and in the far-future of $0.88 \pm 0.07\,\text{m}$ from a historical control mean of $1.53 \pm 0.17\,\text{m}$. Over the entire future period (2006-2070), the linear regression of the annual ice thickness timeseries has a slope of $-0.007\,\text{m/yr}\,(\text{p} < 0.01)$.

4.3.3 Temperature and Heat Content

The ensemble mean, annual top 50m ocean temperature (Figure 4.7a-c, Table 4.1) in northern Baffin Bay is predicted to increase by approximately $0.9°C$ over the study period. Over the entire future period, the 50 m ocean temperature is increasing at a rate of $0.02°\text{C/yr}\,(\text{p} < 0.01)$, whereas during the historical control period is $0.01°\text{C/yr}\,(p < 0.01)$. From the historical control period to the near-future period there is a 43% and to the far-future a 84% increase, respectively. The top 500m of northern Baffin Bay warms by $\sim 1.3°C$ more than the top 50 m. Over the top 500 m there is a 144% increase in the temperature from the historical control and a 355% increase to the far-future mean temperature. The top 500m temperature is found to increase at a rate of $0.03°\text{C/yr.}(\text{p} < 0.01)$, both the spring and winter rates of warming are similar. RCP8.5 experiments experience the greatest warming rates, however the GFDL and MIROC5 RCP4.5 experiments reach similar temperatures at the end of the study period. The MRI-CGCM3 RCP4.5 experiment consistently has the least amount of warming. The spatial structure between the three time periods remains constant with the greatest temperatures at depth and the eastern side being warmer than the west.

Heat content (Table 4.1) is calculated with a reference temperature of $-1.8°\text{C}$, the freezing temperature of sea water. In the top 50m, heat content is increasing in terms of annual averages and across all seasons. Over the top 50m, from the 1981-2005 to the 2050-2070 time periods the annual ensemble mean predicts a 201% increase of northern Baffin Bay heat content. Comparing the far-future to the historical mean, the spring heat content increases by 381% and the winter heat content increases by 390% over the top 50m. In the surface layer, RCP8.5 have the greatest heat content. In the top 500m (Figure 4.7d-f) the heat content increases by 111% from a historical mean value of $8.0 \pm 0.7 \times 10^{11}\text{GJ}$. The spring ensemble mean has a 109% increase, from a historical mean to the far-future. In winter, there is a 106% increase between the historical control and far-future periods. The percent change of the top 500m heat content in spring and winter for the near-future and far-future behave similarly to the annual average. This contrasts the changes in the top 50m where there are seasonal differences. Different mechanisms are working to warm the ocean at these depths causing the difference in seasonality. Over the top 500m, the constrast between the RCP4.5 and RCP8.5 output is more prominent than the top 50m. Over the future period, RCP8.5 experiments consistently have $\sim 0.3 \times 10^{12} GJ$ greater heat content than RCP4.5 experiments.

4.3.4 Atlantic Waters entering through Davis Strait

The timeseries of Atlantic Water (AW) volume entering through Davis Strait measures the potential impacts of this warm, saline water mass entering into northern Baffin Bay (Figure 4.8a). The AW definition we use is same as the Curry et al. (2014), West Greenland Irminger Water definition: $\theta > 2°$ and $\text{S} > 34.1$. These waters are warmer than the top 50m waters at any point in the study and play a greater role in warming the lower layers compared to atmospheric warming at the ocean surface. To quantify the amount of AW entering the bay only the components of the ocean

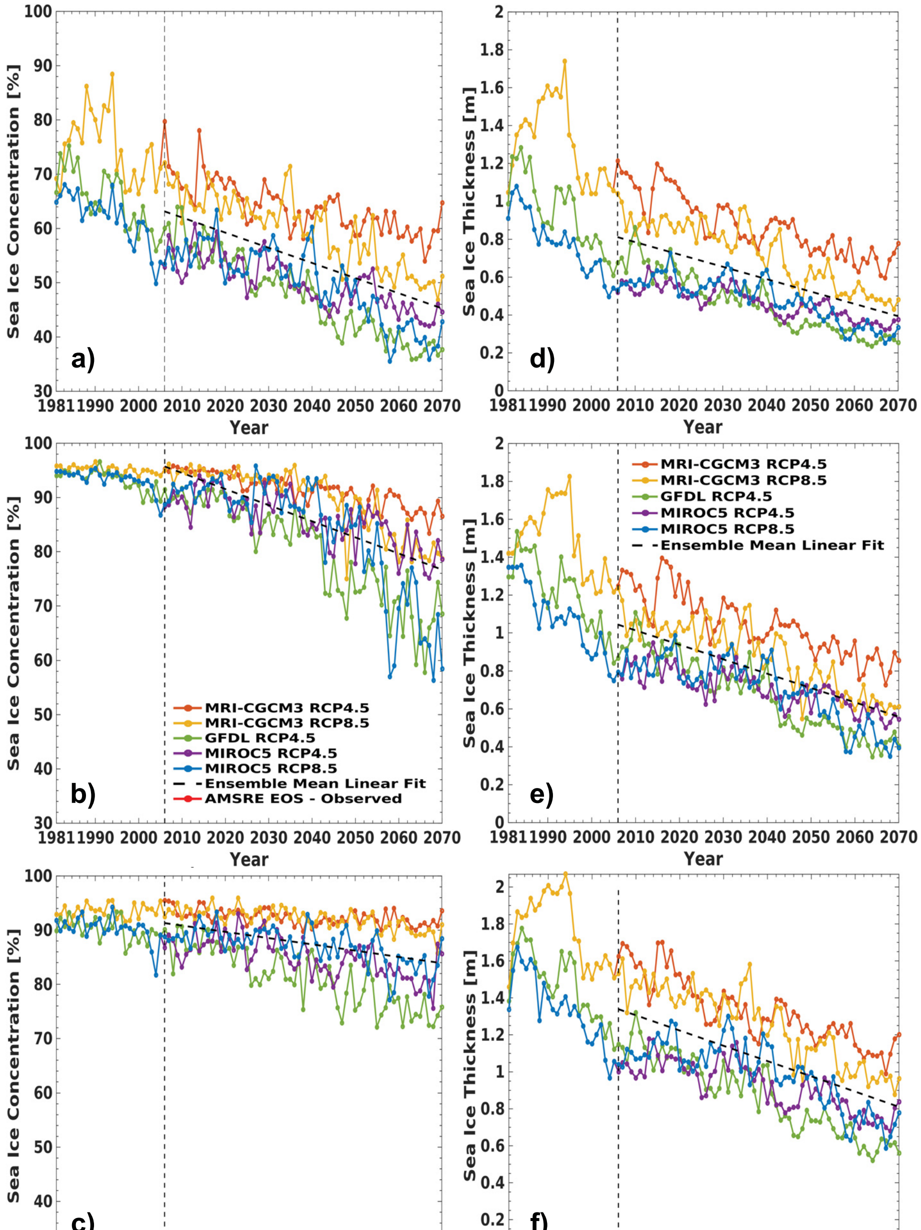

Figure 4.6: a) Annual average b) December-January-February average c) March-April-May average sea ice concentration [%] (observations based on AMSR-E and AMSR2 data Spreen et al. (2008)) d) Annual average e) December-January-February average f) March-April-May average sea ice thickness [m].

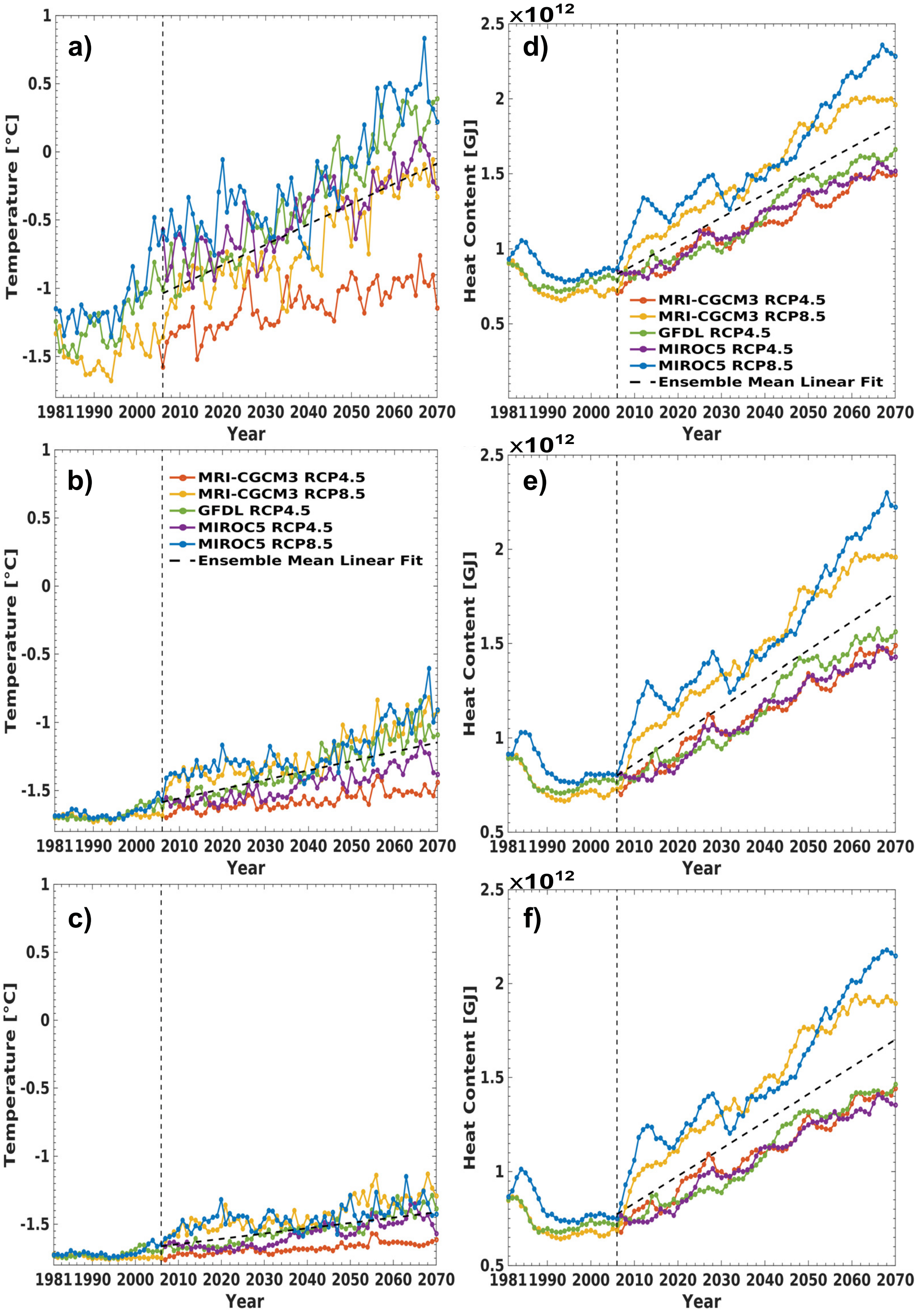

Figure 4.7: a) Annual average b) december-january-february average c) march-april-may average top 50m ocean temperature [°C] d) Annual average e) december-january-february average f) march-april-may average top 500m heat content [GJ].

Table 4.1: Ensemble mean heat content [GJ] and temperature [°C] for the historical control (1981-2005), near-future (2030-2049), and far-future (2050-2070) periods.

Variable	Depth	Season	Historical control	Near-future	Far-future
Heat Content	50 m	Annual	$4.1 \pm 1.1 \times 10^{10}$	$8.2 \pm 1.0 \times 10^{10}$	$1.2 \times 10^{11} \pm 1.0 \times 10^{10}$
Heat Content	50 m	Spring	$5.7 \pm 1.2 \times 10^{9}$	$1.7 \times 10^{10} \pm 1.2 \times 10^{9}$	$2.7 \times 10^{10} \pm 3.0 \times 10^{9}$
Heat Content	50 m	Winter	$9.4 \pm 2.3 \times 10^{9}$	$2.7 \times 10^{10} \pm 4.2 \times 10^{9}$	$4.6 \times 10^{10} \pm 5.8 \times 10^{9}$
Heat Content	500 m	Annual	$8.0 \times 10^{11} \pm 6.7 \times 10^{10}$	$1.2 \times 10^{12} \pm 1.2 \times 10^{11}$	$1.7 \times 10^{12} \pm 8.8 \times 10^{10}$
Heat Content	500 m	Spring	$7.5 \times 10^{11} \pm 7.1 \times 10^{10}$	$1.1 \times 10^{12} \pm 1.1 \times 10^{11}$	$1.6 \times 10^{12} \pm 7.7 \times 10^{10}$
Heat Content	500 m	Winter	$7.9 \times 10^{11} \pm 7.3 \times 10^{10}$	$1.1 \times 10^{12} \pm 1.1 \times 10^{11}$	$1.6 \times 10^{12} \pm 8.6 \times 10^{10}$
Temperature	50 m	Annual	-1.27 ± 0.15	-0.73 ± 0.14	-0.21 ± 0.14
Temperature	50 m	Spring	-1.73 ± 0.02	-1.58 ± 0.02	-1.44 ± 0.04
Temperature	50 m	Winter	-1.7 ± 0.03	-1.45 ± 0.06	-1.20 ± 0.08
Temperature	500 m	Annual	-0.43 ± 0.12	0.19 ± 0.21	1.10 ± 0.15
Temperature	500 m	Spring	-0.51 ± 0.12	0.05 ± 0.18	0.89 ± 0.13
Temperature	500 m	Winter	-0.45 ± 0.13	0.12 ± 0.19	0.99 ± 0.15

velocity moving northward into Baffin Bay were considered, excluding the southward flux exiting via the BIC. The section extends from the Greenland coast to the center of the Strait. There is an increase in the AW flux, with the flux increasing from a historical control mean of $0.78 \pm 0.25\,\mathrm{Sv}$ to $1.14 \pm 0.13\,\mathrm{Sv}$ $(+46\%)$ in the near-future and $1.28 \pm 0.88\,\mathrm{Sv}$ $(+63\%)$ in the far-future. All seasons show an increasing trend in the AW flux. All experiments have similar rates of change. This suggests that differing RCP scenarios and forcings only play a small role in the development of the positive trend in AW flux.

4.3.5 Surface Heat Flux

The annual surface heat flux (Figure 4.8b) increases from the historical control period to the far-future. From a historical mean of $4.2 \pm 2.1\mathrm{Wm}^{-2}$, it grows to $8.1 \pm 1.7\,\mathrm{Wm}^{-2}$ $(+93\%)$ in the near-future, and is $12.3 \pm 1.9\,\mathrm{Wm}^{-2}$ $(+193\%)$ in the far-future period. In terms of temperature and heat content (Figure 4.7), the two RCP8.5 experiments have the greatest values, but this is not the case for the surface heat flux. The surface heat flux is similar to the AW flux in that no experiment has markedly different heat flux values. However, percent changes are similar to those of temperature and heat content. Changes to the surface heat flux are then expected to be due to changes in the sensible heat brought into the region by AW as well as an increased shortwave and longwave fluxes as is the case for the surface temperatures. An enhanced surface heat flux plays a role in ice losses throughout the study period and is indicative of ice concentration losses. A smaller ice concentration allows for a greater surface heat flux through enhanced exposure of the sea surface to the atmosphere. Over the 2006-2035 period the surface heat flux decreases, this is predicted to be the product of an enhanced ice area flux. A slowing of ice concentration losses from 2006-2025 is predicted in winter and spring (Figure 4.6b, c) are also indicative of these changes.

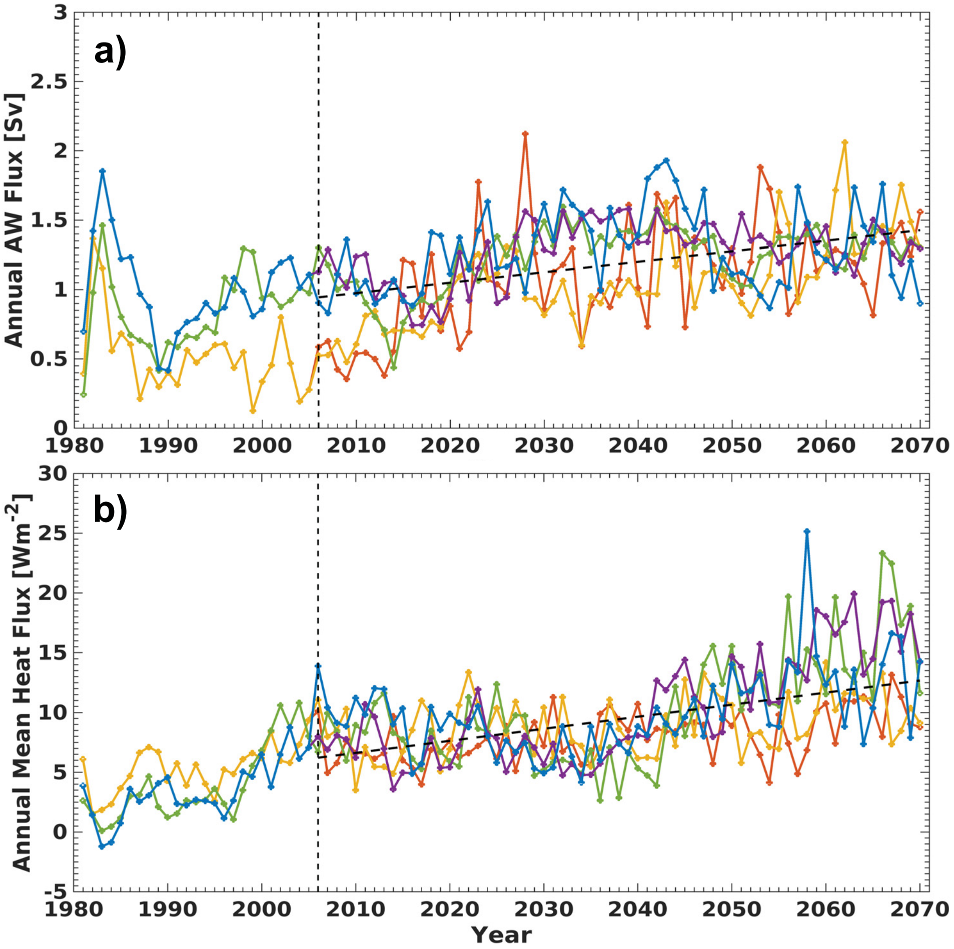

Figure 4.8: a)Annual average Davis Strait Atlantic Water flux [Sv]. Atlantic Water is defined as $\theta > 2°\text{C}$ and $S > 34.1$. b) Surface heat flux [Wm^{-2}]. Positive numbers indicate an upwards heat flux.

4.3.6 Salinity and Freshwater Content

The top 50m ensemble mean annual ocean salinity (Figure 4.9a-c, Table 4.2) remains similar to the historical control mean of 33.3 ± 0.3, corresponding to a 0.5% decrease between the historical control and far-future periods. RCP8.5 experiments have lower salinities (by ~ 1.5) than other ensemble members during the future period, due to the difference in Greenland discharge between RCP4.5 (which uses RCP2.6 discharge) and RCP8.5 experiments (Figure 4.3a). The top 500m ensemble mean annual and seasonal ocean salinities are higher than when only considering the top 50m of the water column. From the historical to the far-future there is a 1.2% increase in the top 500m salinity. Over the top 500 m there are smaller differences between RCP4.5 and RCP8.5 scenarios, with the RCP8.5 salinity being ~ 0.2 lower. The differences in the salinity trends of the top 50 m compared to the top 500 m highlight that there are different mechanisms for future salinity changes within these two layers.

A reference salinity of 34.8 was used to calculate freshwater content (FWC). Calculations use the ensemble mean salinity of the entire layer. FWC in the top 50m is found slightly increase over the study period. Top 50m FWC is found to increase by 20% in the near-future and 12% in the far-future. Notably, the near-future FWC is greater than the far-future values. The FWC linear trend over the future period (2006-2070) is $-1.61\,\mathrm{km}^3/\mathrm{yr}\,(\mathrm{p} < 0.01)$. The positive trend of the top 50m layer goes against the increasing Greenland discharge (Figure 3a), suggesting the decrease in FWC between the near- and far-future could be due to the sea ice loss and the increased presence of AW. However, the far-future mean is less than the near-future indicating that Greenland discharge is still predicted to play a role later in the century. In terms of a percent change, both the spring and winter changes are similar to the annual. As expected, RCP8.5 experiments have the highest FWC due to enhanced Greenland discharge. When looking at the top 500m (Figure 4.9d-f) there is a strong decreasing trend over the future period $-101\mathrm{km}^3/\mathrm{yr}\,(\mathrm{p} < 0.01)$. When considering the upper 500m seasonal trends, they are similar to the annual. There is found to be a 29% decrease in the near-future and a 69% decrease in the far-future. The negative trend in the top 500m FWC along with the absence of a smaller trend in the top 50m highlight the impact of AW entering the region at depth.

From the temperature, heat content, salinity, and FWC timeseries, the increased presence of warm, saline, Atlantic Waters at depth puts into context the predicted changes. An increasing air temperature and Greenland runoff are impacting the top 50m waters, while Atlantic Waters are dominating these changes over the top 500m.

4.3.7 Mixed Layer Depth

In the historical control, the maximum mixed layer depth (MLD, Figure 4.10a) is $208 \pm 50\,\mathrm{m}$. Future maximum mixed layer depth MLDs are largely determined by the RCP scenario and Greenland discharge used. RCP4.5 experiments maintain MLD $\sim 150-200$m out to 2070. Though a number of years have maximum MLDs ranging from $400-700$m, particularly in the GFDL RCP4.5 and MIROC5 RCP4.5 experiments. RCP8.5 experiments have maximum MLDs which are consis-

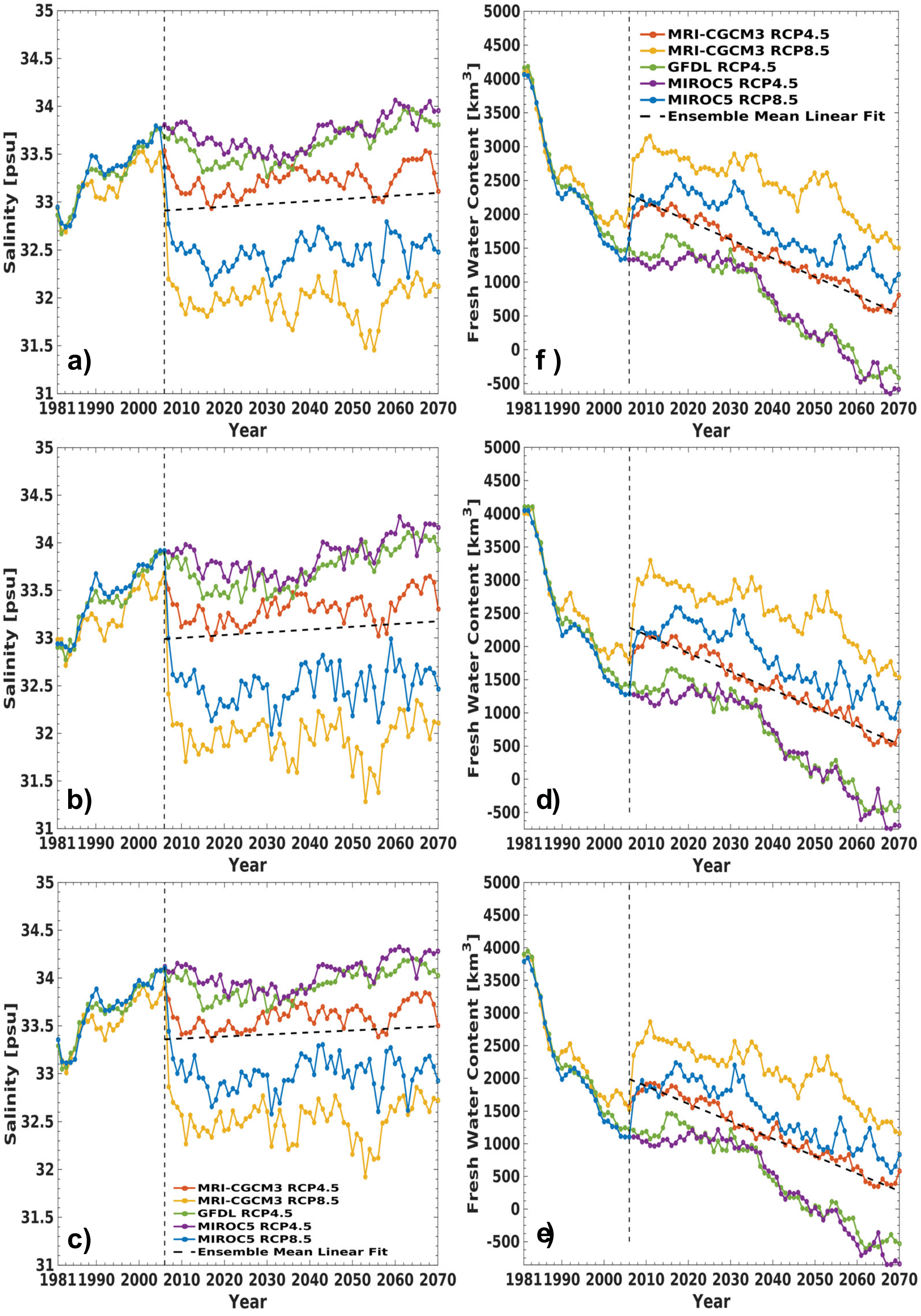

Figure 4.9: 50m Salinity [ ] a) Annual average b) December-January-February average c) March-April-May. 500m Freshwater Content [km^3] d) Annual average e) December-January-February average f) March-April-May. Freshwater content is calculated with a reference salinity of 34.8

Table 4.2: Ensemble mean freshwater content [km^3] and salinity [ ] for the historical control (1981-2005), near-future (2030-2049), and far-future periods (2050-2070).

Variable	Integrated depth	Time-period	Historical control	Near-future	Far-future
Freshwater Content	50 m	Annual	856 ± 151	1020 ± 54	956 ± 68
Freshwater Content	50 m	Spring	656 ± 146	782 ± 54	731 ± 62
Freshwater Content	50 m	Winter	810 ± 155	981 ± 67	907 ± 80
Freshwater Content	500 m	Annual	2430 ± 768	1722 ± 279	758 ± 246
Freshwater Content	500 m	Spring	2280 ± 777	1433 ± 276	498 ± 235
Freshwater Content	500 m	Winter	2505 ± 786	1719 ± 286	748 ± 260
Salinity	50 m	Annual	33.3 ± 0.3	33.0 ± 0.1	33.1 ± 0.1
Salinity	50 m	Spring	33.6 ± 0.3	33.4 ± 0.01	33.5 ± 0.1
Salinity	50 m	Winter	33.3 ± 0.3	33.0 ± 0.1	33.2 ± 0.1
Salinity	500 m	Annual	34.2 ± 0.2	34.4 ± 0.1	34.6 ± 0.1
Salinity	500 m	Spring	34.3 ± 0.2	34.5 ± 0.1	34.7 ± 0.1
Salinity	500 m	Winter	34.2 ± 0.2	34.3 ± 0.1	34.6 ± 0.1

Table 4.3: Ensemble mean linear regression rates of change over the historical control and future periods (2006-2070). Bolded values are significant to $p < 0.01$. An asterisk denotes values which are not significant.

Variable	Integrated Depth	Historical Control	Future Period
Convective Energy	200 m	$-4.2\,kgm^{-2}s^{-1}/yr$	$1.5\,kgm^{-2}s^{-1}/yr$
Davis Strait Atlantic Water Flux	N/A	$-6.0 \times 10^{-3}\,Sv/yr^{*}$	$8.0 \times 10^{-3}\,Sv/yr$
Fresh Water Content	50 m	$-19\,km^3/yr$	$-1.6\,km^3/yr$
Fresh Water Content	500 m	$-100\,km^3/yr$	$-28\,km^3/yr$
Heat Content	50 m	$1.1 \times 10^{9}\,GJ/yr$	$1.1 \times 10^{9}\,GJ/yr$
Heat Content	500 m	$-5.9 \times 10^{9}\,GJ/yr$	$1.6 \times 10^{10}\,GJ/yr$
Nares Strait Ice Area Flux	N/A	$3.5\,km^2/yr$	$5.9 \times 10^{-2}\,km^2/yr^{*}$
Nares Strait Ice Volume Flux	N/A	$-1.0\,km^3/yr^{*}$	$-1.1\,km^3/yr$
Salinity	50 m	$3.5 \times 10^{-2}\,/yr$	$3.0 \times 10^{-3}\,/yr$
Salinity	500 m	$2.4 \times 10^{-2}\,/yr$	$6.0 \times 10^{-3}\,/yr$
Sea Ice Concentration	N/A	$-0.44\,\%/yr$	$-0.28\,\%/yr$
Sea Ice Thickness	N/A	$-1.8 \times 10^{-2}\,m/yr$	$-7.0 \times 10^{-3}\,m/yr$
Surface Heat Flux	N/A	$0.2\,Wm^{-2}y^{-1}$	$0.1\,Wm^{-2}yr^{-1}$
Temperature	50 m	$1.4 \times 10^{-2}\,^{\circ}C/yr$	$1.5 \times 10^{-2}\,^{\circ}C/yr$
Temperature	500 m	$-1.0 \times 10^{-2}\,^{\circ}C/yr$	$2.7 \times 10^{-2}\,^{\circ}C/yr$

tently $\sim 80-100$m. The shallow MLDs in the RCP8.5 experiments begin almost immediately after 2006 which coincides with the beginning of the future portion of the study and the increased Greenland freshwater discharge. Increased glacial melt and the associated freshwater input to the region is increasing the stratification in the RCP8.5 experiments. 2015-2025 is a period of low MLDs in all experiments which is expected to be an adjustment period for the MLD in response to increasing freshwater input from the adjacent Greenland Ice Sheet and Ellesemere Island glaciers.

Sea ice also plays a role in future MLDs. The MRI-CGCM3 RCP4.5 experiment with the greatest sea ice thickness and concentration has the shallowest MLD relative to the other RCP4.5 experiments with lesser ice thickness and concentration. Further, the MRI-CGCm3 RCP4.5 experiment has the strongest increasing trend in the ice area flux during the future period, highlighting the role of an ice entering the region through Nares Strait. The 2015-2025 period of low MLDs could also then be a response to an increasing ice area flux.

Finally, precipitation (and its impact on the freshwater content of the ocean surface layer) is playing a small role in MLD changes as there is both a positive trend in the precipitation and the largest MLDs are occurring near the end of the study period. The GFDL RCP4.5 experiment maintains the greatest MLD with a maximum of ~ 750m in 2061. The GFDL experiment experiences the greatest increase in precipitation, but at the same time also having the strongest winds, providing energy for mixing. Precipitation changes are playing only a small role in modifying the MLD, while Greenland discharge has potential to limit deeper mixing in northern Baffin Bay.

4.3.8 Convective Energy

Convective energy (Figure 4.10b) provides insight to the changes in density stratification and is a measure of how much energy is required to mix the fluid column to a depth h (we use $h = 200\,\text{m}$). The definition of convective energy follows Bailey et al. (2005), Frajka-Williams et al. (2014), and Holdsworth and Myers (2015). In the historical control period the mean convective energy is $68946 \pm 61\text{kgm}^{-2}\text{s}^{-1}$, grows to $69190 \pm 26\text{kgm}^{-2}\text{s}^{-1}(+0.4\%)$ in the near-future and reaches $69234 \pm 47\text{kgm}^{-2}\text{s}^{-1}(+0.4\%)$ in the far-future. Similar to the MLD, future convective energy is largely dependent on the RCP scenario and Greenland discharge. The two RCP8.5 experiments have a $\sim 450\text{kgm}^{-2}\text{s}^{-1}$ greater convective energy than the RCP4.5 experiments. The difference between the two RCP scenarios is greater than the changes taking place over the study period. In the future-period, the rates of increase across all experiments are similar. Thus, runoff is dominating changes to future stratification, with temperature increases contributing to a lesser extent. The AW flux does not appear to play a significant role to future density stratification as theses waters are entering the region at a greater depth than the reference value h. The future of the density stratification will mirror future Greenland Ice Sheet melt rates. Potential changes could impact key biogeochemical properties and processes as well as the mixing of heat to the surface.

4.3.9 Biogeochemical Properties

To look at predicted changes to biogeochemical properties we focused on dissolved oxygen concentration, total alkalinity concentration, phytoplankton net primary production and the phytoplankton bloom dynamics using chlorophyll-a concentration. This analysis provides insight into how these critical variables may change in response to a changing ocean, ice, and atmosphere regime. Using the surface layer and deep layers as reference we checked for significant temporal trends (using linear regression) and differences between the historical, near- and far-future periods (using non-parametric Kruskal-Wallis H test and Wilcoxon rank test). The upper layer was defined from the surface down to 50m for dissolved oxygen and total alkalinity concentration or down to 30m for net primary production and chlorophyll-a concentration. The adjusted depth to 30m for the analyses of net primary production and chlorophyll-a is chosen because 30m is the average spring/summer mixed layer depth observed in Pikialasorsuaq (Lewis et al. (1996); Tremblay et al. (2002)). The deep layer was defined from surface down to 200m.

The annual mean surface dissolved oxygen concentration decreases at a rate of $0.2\,\text{mmol/m}^3/\text{yr}$ ($p < 0.01$) between 2006 to 2070 (Figure 4.11a). The annual mean surface dissolved oxygen concentration is $367.6 \pm 5.6\,\text{mmol/m}^3$ during the historical control period (1981-2005) and $355.6 \pm 2.9\,\text{mmol/m}^3$ (-3.4%) in the far-future (2050-2070). Spring oxygen concentrations did not change significantly during this period (2006-2070), but in winter and summer, the oxygen concentration declined at a rate of $0.2\,\text{mmol/m}^3/yr$ ($p < 0.01$), and in fall it declined at a rate of $0.3\,\text{mmol/m}^3/\text{yr}$ ($p < 0.01$). The historical control mean oxygen concentration of each season is: $362.4 \pm 6.6\,\text{mmol/m}^3$ in winter, $379.8 \pm 5.6\,\text{mmol/m}^3$ in summer, $373.4 \pm 6.6\,\text{mmol/m}^3$ in fall, and $355.3 \pm 6.2\,\text{mmol/m}^3$ in spring. The predicted far-future mean oxygen concentration is: $350.2 \pm 3.3\,\text{mmol/m}^3$ in winter, $368.2 \pm 2.3\,\text{mmol/m}^3$ in summer, $347.9 \pm 3.5\,\text{mmol/m}^3$ in fall and $356.0 \pm 3.5\,\text{mmol/m}^3$ in spring. Comparing these two periods, the mean dissolved oxygen concentration decreases in winter by $\sim 12\,\text{mmol/m}^3$ (3.5%), in summer by $\sim 11\,\text{mmol/m}^3$ (3.1%), and in fall by $\sim 26\,\text{mmol/m}^3$ (7.3%), and only a small (not significant) change in spring (0.2%).

The rates of decline of the oxygen concentration of the deep water layer are much larger than those presented for the surface layer. Deep water oxygen concentration declines at a rate of $0.5\,\text{mmol/m}^3/\text{yr}$ ($p < 0.01$) for the annual mean, and the four seasons. The concentration of oxygen in the deep layer is, $20\,\text{mmol/m}^3$ lower than in surface waters due to the combined effect of higher respiration rates in deep waters (4x higher remineralization rate, Figure S1), and poor deep water ventilation (i.e., monthly mean mixed layer depth shallower than 60 m year-round). It should be noted that across all seasons and on a yearly basis, the MRI RCP8.5 run maintains a higher dissolved oxygen concentration (by $\sim 10\,\text{mmol/m}^3$) and has a smaller rate of change over the course of the study period compared to the MIROC5 RCP8.5.

In surface waters, the annual mean total alkalinity remains stable from 2006 to 2070. However if seasonal trends are considered, total alkalinity decreases in summer and significantly increases in winter at rate of 0.3 and $0.2\,\text{mmol/m}^3/\text{yr}$ ($p < 0.01$), respectively. Deep waters experience more significant changes: the annual and spring total alkalinity increases at a rate of $0.2\,\text{mmol/m}^3/\text{yr}$

($p < 0.01$), and in the fall and winter it increases at a rate of 0.3mmol/m^3/yr ($p < 0.01$). In summer, the total alkalinity of the deep waters do not change significantly ($p = 0.02$). The historical mean total alkalinity concentration over the top 200m is 2329.0 ± 9.0 mmol/m^3 for the annual mean, 2332.1 ± 8.9 mmol/m^3 in winter, $\sim 2318.5 \pm 8.7$ mmol/m^3 in fall, 2332.1 ± 8.9 mmol/m^3 in spring. Comparing the historical control mean to the far-future mean we derived the total alkalinity concentration magnitude change of 0.3% (2336.3 ± 6.9 mmol/m^3) for the annual mean, 0.7% (2348.7 ± 7.3 mmol/m^3) in winter, 0.3% (2324.6 ± 6.9 mmol/m^3) in fall, and 0.4% (2350.7 ± 6.8 mmol/m^3) in spring. The total alkalinity concentration at depth in summer remains ~ 2320 mmol/m^3 from 1981-2070. The MIROC5 RCP8.5 experiment always maintains a higher and relatively constant total alkalinity across the study period. Conversely, the MRI RCP8.5 experiment shows large or steep decreases in total alkalinity.

The annual mean net primary production in surface water is not predicted to change significantly between 1981 and 2070 (linear trend: $b = -0.03$ mgC/m^2/d, $p = 0.28$; Figure 4.11c). The historical estimates is 62.9 ± 9.7 mgC/m^2/d, which is only 6% larger than the future estimate 58.9 ± 5.0 mgC/m^2/d (Wilcoxon rank test: $z = 1.65$, $p = 0.10$). Additionally, the simulations also do not predict a change in the magnitude of the annual maximum (Kruskal-Wallis H test: $H = 3.56$; $df = 2$; $p = 0.17$) nor on its timing ($H = 6.55$, $df = 2$, $p = 0.04$). The magnitude of the annual maximum is 250.8 ± 43.5 mgC/m^2/d and the timing is in early June. However, when seasonal trends (1981-2070) are considered, there is a significant decline in net primary production in summer and in fall that happens immediately after switching to the future simulation (Figure 4.11c). This sharp decline is linked to the step-like increase in Greenland discharge (Figure 4.3a), which causes an increase in the buoyancy of surface waters (Figure 4.10b) which leads to a sharp shallowing of the maximum mixed layer depth. The future shallowing of mixing and increase in stratification, particularly during winter (Figure 12b) leads to lower nutrient concentration in the surface water in spring. These nutrients are then all consumed during the spring, causing a stronger summer nutrient limitation (Figure S2) that results in the lower summer primary production. At the same time, the more buoyant waters lead to a late start of the fall mixing (Figure 12b) because more energy is needed to break through the stratification (convective energy). This delays the nutrient replenishment of surface waters. The delay results in the nutrients being available only once light limitation comes into play, thus causing a strong nutrient limitation in the fall reducing the primary production in the this season (Figure S2). Aside from this sharp decline, there is no change in summer or fall primary production between the near- and far-future period.

If we only consider changes over the future period (2006-2070), the annual mean net primary production gradually increases at a rate of 0.1 mgC/m^2/d/yr ($p < 0.01$) driven by the gradual increase in spring primary production at a rate of 0.4 mgC/m^2/d/yr ($p < 0.01$). Spring net primary production increases by 50% from a historical value of 60.8 ± 14.7 mgC/m^2/d to 91.7 ± 13.0 mgC/m^2/d in the far-future. We note that the MIROC5 RCP8.5 experiment has higher magnitude of net primary production compared to the MRI RCP8.5 experiment on the annual basis and across all seasons. Both experiments are in good agreement on the rate of change of net primary production. In the

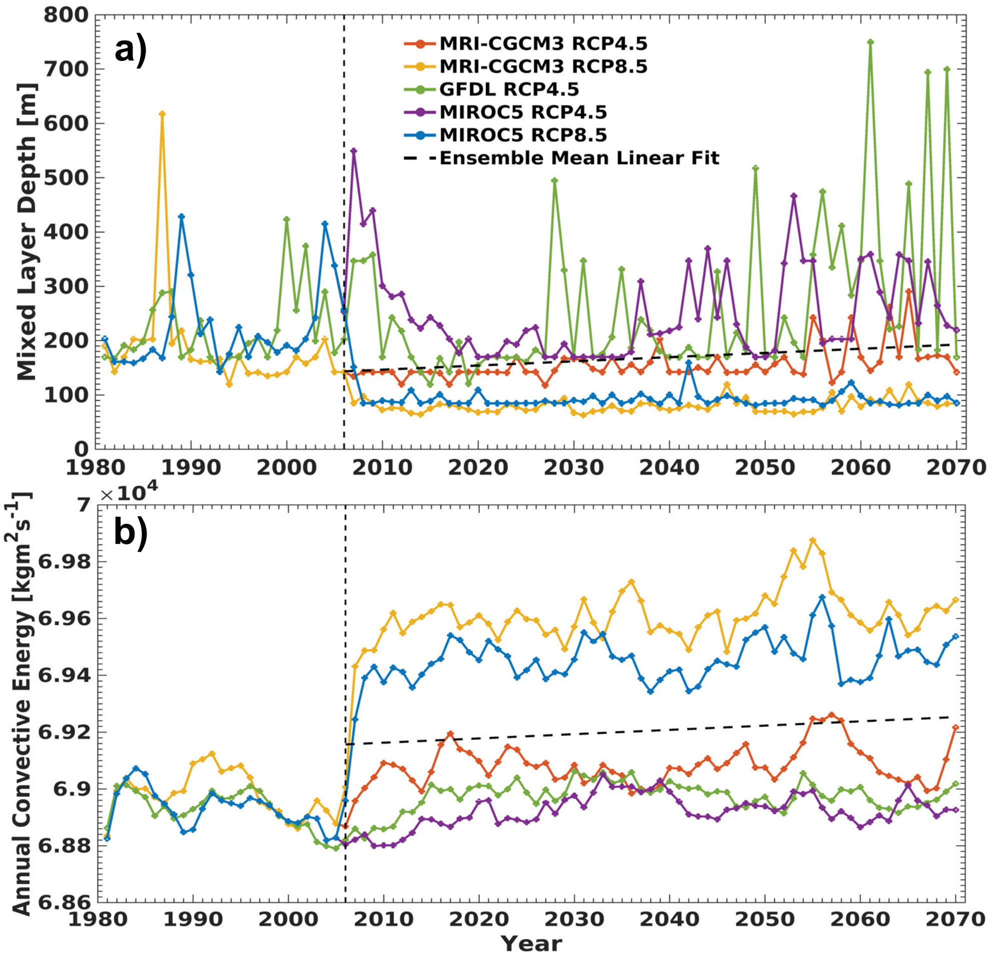

Figure 4.10: Northern Baffin Bay a) maximum mixed layer depth [m] b) 200*m* convective energy [kg $m^{-2}s^{-1}$].

deeper layers, biological consumption (remineralization) dominates over primary production. The simulation do not predict a significant change in remineralization over the future period (Figure S1).

Chlorophyll-a concentration is an indicator of phytoplankton biomass in the ocean, whereby high chlorophyll-a concentration indicates greater phytoplankton biomass. In northern Baffin Bay, the simulation predicts two phytoplankton blooms, one in spring and one in fall (seen as two maxima in chlorophyll-a concentration in Figure 12a). Over the historical control, near-, and far-future periods, the model predicts a similar magnitude of the spring bloom ($\approx 1.4\,\text{mg/m}^3$; Kruskal-Wallis H test: $H = 2.82$, $df = 2$; $p = 0.24$), however the three periods have a different timing of the spring bloom ($H = 41.67$, $df = 2$, $p < 0.01$). It advances 18 days in the near-future (Wilcoxon rank sum: median = May 01st, $z = 5.3$, $p < 0.01$), and 20 days in the far-future (median= Apr 30th, $z = 5.5$, $p < 0.01$) relative to the historical period (Figure 12a). On the other hand, the timing of the fall bloom does not change ($H = 3.14$, $df = 2$, $p < 0.2$), but the magnitude decreases from a median of $0.8\,\text{mg/m}^3$ during the historical period to a median of $0.4\,\text{mg/m}^3$ in the near- and far-future ($p < 0.01$, Wilcoxon rank sum: z = 5.7 and z = 5.8 respectively).

4.4 Discussion

Impacts on the sea ice regime by the end of the study period are primarily caused by a thinning ice pack. Ice thinning and concentration decreases are caused by a warming atmosphere, an increasing heat content in the upper ocean layers, and a growing surface heat flux. The small increase in ice area flux through Nares Strait (Figure 4.5a) is more indicative of the expected changes in the sea ice regime in the coming decades as thinning ice is more readily pushed through Nares Strait. A decreasing ice concentration in all seasons makes the increasing ice area flux significant given that there is less ice to move through the strait throughout the year. A decrease in the ice volume flux (Figure 4.5b) is the response to a strong thinning signal. Thinning and subsequent concentration losses will dominate the ice regime by the far-future period. Ice remains relatively thick until $\sim$ 2020 due to the slowly increasing ice area flux. A decreasing thickness and concentration will impact the ice arch in Nares Strait. Decreasing the duration of the ice arch in Nares Strait is predicted to have an impact on the region by changing the duration and shape of Pikialasorsuaq (Stern and Heide-Jorgensen, 2006; Vincent, 2019). A changing ice arch in Nares Strait will impact the seasonality of thick ice that enters Baffin Bay (Vincent, 2019). The increasing surface heat flux (Figure 4.8b) is also indicative of an increasing ice area flux from 2006-2030 where there is a decreasing trend at this time. Further, during this time there is a muting of winter and spring ice concentration losses (Figure 4.6b, c).

From a polynya formation and maintenance standpoint, there are two factors which are contradictory to the future of the polynya. First, the heat content in northern Baffin Bay is predicted to increase, this presents a possible mechanism for maintaining the polynya, particularly on the east side closest to Greenland, where northward heat transport is already thought to play a significant role in the formation of the polynya (Melling et al., 2002). Our results suggest an increase in warm, saline waters entering through Davis Strait, the propagation of these waters northward along the west coast of Greenland could potentially enhance ice melt in the eastern portion of the polynya and increase the duration and area occupied by the polynya. Second, the potential shallowing of MLDs and increase in convective energy presents the idea that there could be a significant decrease in vertical mixing. Mixing of heat to the surface during ice formation also plays a role in maintaining the polynya (Vincent, 2019; Yao and Tang, 2003). Processes such as convection generated by brine drainage from sea ice formation and upwelling due to Ekman motion are not able to overcome the enhanced stratification. This would eliminate one of the primary mechanisms of polynya formation. However, if the increased volume of warm waters are able to mix to the surface, they could enhance ice melt and magnify this mechanism. The magnitude at which these two processes will act to modify the polynya in the future is uncertain, though it is reasonable to consider that the east side of the polynya will continue to form with some regularity during the winter, while the west side might be greatly impacted by a thinning ice pack and increasing density stratification. All of these factors considered present the notion that biological processes in Pikialasorsuaq such as

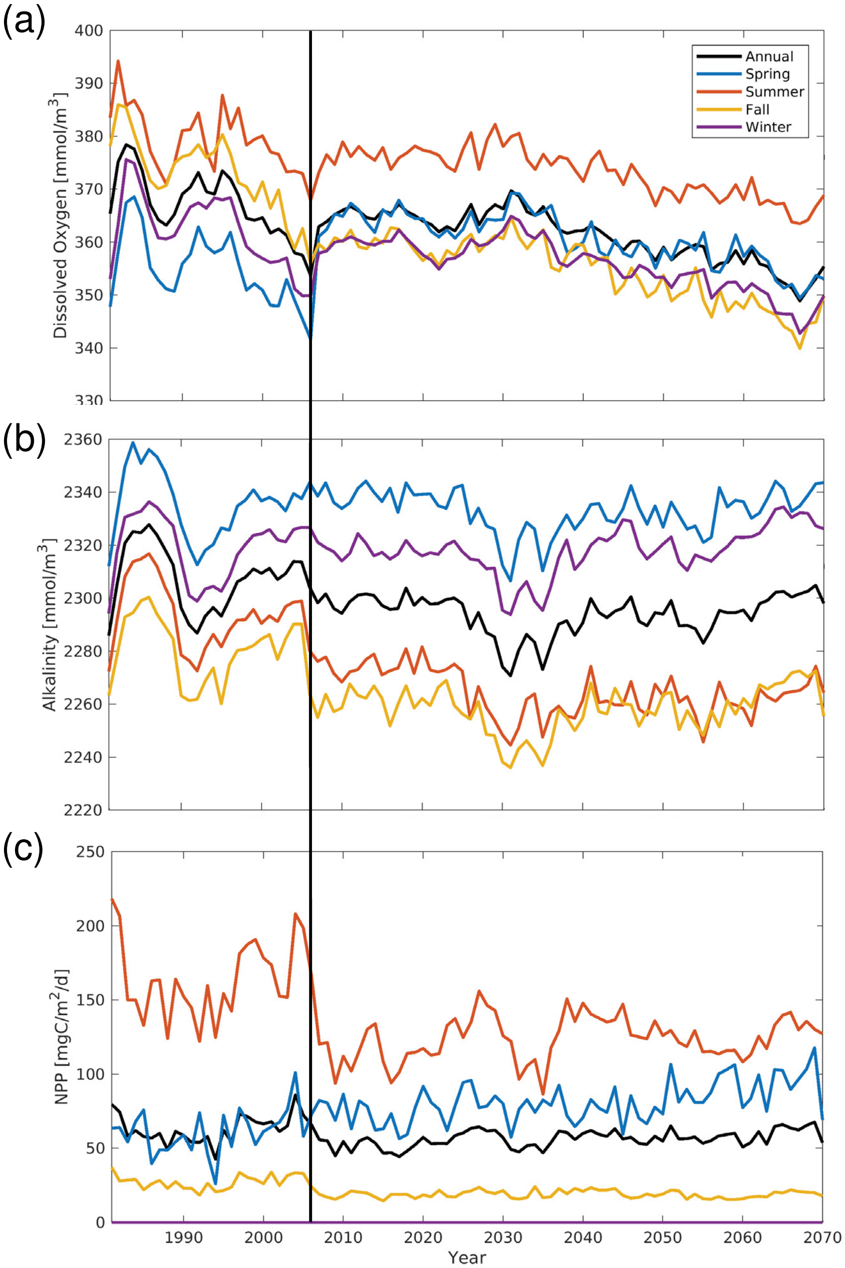

Figure 4.11: Time-series of (a) dissolved oxygen concentration, (b) total alkalinity and (c) phytoplankton net primary production (NPP) in northern Baffin Bay. Presenting the annual (Jan-Dec), spring (Mar-May), summer (Jun-Aug), fall (Sep-Nov) and winter (Dec-Feb) averages of the surface layer defined as the top 50m for dissolved oxygen and total alkalinity, and the top 30m for NPP. The averaging area of northern Baffin Bay is defined in the inset of Figure 1. Vertical black line marks the end of the historical period and the start of the future period.

nutrient levels, light levels, and the timing of production cycles will all be impacted by an evolving ice regime (Ingram et al., 2002).

Changes to surface waters are the product of warming surface air temperatures, an increase in surface freshwater input from Greenland, and AW penetrating the study region. This creates a warmer and slightly more saline top 50m. An enhanced Greenland freshwater input is being outweighed by the saline, AW. The top 500m of the water column is predicted to be more greatly impacted by AW. This is due to an increase in the warm, saline, AW penetrating into northern Baffin Bay. Moreover, during the far-future period every year has a mean salinity greater than 34. High salinities are indicative of the presence of AW (Münchow et al., 2015). A potential mechanism responsible for the increased AW penetration into northern Baffin Bay is an enhanced cyclonic gyre circulation caused by raised sea surface heights generated by the larger freshwater input. Castro de la Guardia et al. (2015) described that a positive feedback generated by enhanced Greenland glacier melt as the added freshwater raises the sea surface height along western Greenland causing a strengthening of the WGC. This results in a greater inflow of warm, saline AW into Baffin Bay at Davis Strait, and a reduction in the inflow of cold, fresh Arctic Water through the CAA. This feedback helps explain the simulated increase in temperature and salinity in northern Baffin Bay, and a 63% increase in the transport of warm, saline water entering Baffin Bay. There is an increase in heat content and a decrease in freshwater content in the top 500m layer, meanwhile in the top 50m layer has a near constant salinity trend despite having an increase in freshwater input. However, the two RCP8.5 scenarios would be expected to have the greatest AW flux as these experiments have the greatest Greenland discharge. Hence, we suggest that the drivers for the increased AW flux remain an open question, particularly in the RCP4.5 experiments. A study focusing more on quantitative changes in the water masses entering Baffin Bay through the CAA in the future would further the knowledge on the drivers of heat and freshwater content changes in northern Baffin Bay.

Freshwater content variations and distribution are critical to future MLDs (Figure 4.10a). In particular, the decrease of MLDs are the product of increased freshwater input by Greenland meltwater discharge and the presence of sea ice. Changes in density stratification (convective energy: Figure 4.10b) between RCP scenarios and runoff are greater than density stratification trends. Another source of freshwater, precipitation, plays only a small role. The latter was confirmed with the GFDL RCP4.5 experiment, which has the greatest amount of precipitation, continues to have deep MLDs through to 2070. All ensemble members show an increase in warm AW entering the region through Davis Strait, though this only appears to play a small role in changing the MLD and density stratification. The shape of the MLD timseries in the RCP4.5 experiments can be described in three distinct time periods: the historical period with largely varying MLDs, the 2015-2035 adjustment period where small MLDs are a response to increased runoff, and from 2035-2070 where a vastly reduced ice coverage (due to the thinning signal) then starts deepening the MLDs due to the increased open water in the winter months. The shallowing of mixing in increased runoff scenarios would effectively limit the formation of deep waters in the region and isolate the freshwater surface layer from the underlying more saline layers. Increased stratification also limits the nutrient rich, deep waters from mixing to the surface.

The biogeochemical variables analyzed, dissolved oxygen concentration, total alkalinity concentration, phytoplankton net primary production and bloom dynamic display smaller changes than many of the physical variables. Total alkalinity in surface waters is not predicted to change, and when considering the upper 200m, total alkalinity is predicted to increase by 0.3% with a maximum of 0.4% in spring. Alkalinity is the capacity of the sea water to resist ocean acidification, thus the overall small positive changes in alkalinity suggests that acidification is not likely to impact the region by a large degree. Dissolved oxygen concentration decrease in surface waters by an averaged of 3.4% and a maximum of 7.3% in fall, and if the upper 200m of the water column is considered the declines are in the order of $14 - 15\%$ in each season. Oxygen concentration is predicted to stay above the typical hypoxia threshold (Vaquer-Sunyer and Duarte, 2008, $65 - 125\,\mathrm{mmol/m^3}$). The changes in oxygen concentration within the 200m depth layer are driven by a reduction in the ventilation of waters below 30m depth rather than an increase in biological consumption. This is evident in the shallower depth of mixing during fall and winter during the future period, while remineralization rate do not change throughout the future period.

The annual net primary production of surface waters is not predicted to change between the historical control and far-future period. The apparent stability of the simulated annual mean phytoplankton productivity contrast the small decreasing trend found in the historical satellite records (Marchese et al., 2017). Furthermore, the simulations also predicts that the net primary production is likely to increase in spring with significant changes in the bloom dynamics. The spring bloom is predicted to occur 20 days earlier but the magnitude of the bloom's maximum will not change. On the other hand, the fall bloom timing does not change but its magnitude declines by 50%.

The seasonal advance of the phytoplankton bloom in spring corresponds with an earlier decrease in the sea ice concentration and shallowing of the mixing layer, allowing sunlight into the surface waters and freeing phytoplankton from the winter light limitation. It is the shallowing of the mixing layer depth that ultimately leads to the initiation of the spring phytoplankton bloom, a mechanism that is supported by observations (Marchese et al., 2017). From historical records, the onset of the spring phytoplankton bloom in northern Baffin Bay is linked to seasonal warming, sea ice break-up and also declining wind stress; three physical changes that cause shallowing of the MLD (Marchese et al., 2017). The reduced magnitude of the fall bloom in the far-future is due to a pronounced nutrient limitation. Wind-induced mixing is key to maintain the high productivity in northern Baffin Bay as it resupplies the surface waters with nutrients (Tremblay et al., 2002). In the future, mixing in northern Baffin Bay is significantly reduced due to higher buoyancy of surface waters as a result of increased freshwater content and temperature. Castro de la Guardia et al. (2019) also showed that the timing of the fall mixing in several Arctic regions is critical for the development of the fall bloom, as nutrients must become available before light becomes the limiting factor with the start of the polar night.

It is worth noting that the modelled phytoplankton net primary production and chlorophyll-a concentration over the historical period are lower than in-situ observations within the NOW. Cruisebased observations during the peak productive period (April-July) in 1998 yield an averaged net primary production that is three times larger than model estimates (observed estimates range between $1110-1800\,\mathrm{mgC/m^2/d}$; Klein et al. (2002); Tremblay et al. (2002); Mei et al. (2003)) and more than ten times the modelled chlorophyll-a concentrations during the spring bloom (observed estimates reach maximum values of $14.9-19.8\,\mathrm{mg/m^3}$; Lewis et al. (1996); Klein et al. (2002)). However, one must be cautious when comparing point-based observations to regional averages which can dilute the high values within the core of Pikialasorsuaq. The model estimates are computed over a broad area that covers northern Baffin Bay to Nares Strait, the seasonal maximum chlorophyll-a concentration average over this area is $1.37\,\mathrm{mg/m^3}$ and this estimate is within the range of the seasonal maximum chlorophyll-a concentration derived from satellite and averaged over a similar region (1 - $2.5\,\mathrm{mg/m^3}$; Marchese et al. (2017)).

4.4.1 Limitations

We use a $1/4^\circ$ degree resolution with 50 vertical levels, and although this is considered high resolution for climate simulations, there remain small-scale ocean processes (e.g. diffusion, eddies) that cannot be resolved and need to be parameterized. This inserts some uncertainty in the overall model results that must be considered. Further, the sea ice model, LIM2 (Fichefet and Morales-Maqueda, 1997), creates uncertainty in simulated ice cover as ice grows in thickness space only through thermodynamic processes and there is no parameterization of landfast ice. Finally, the ensemble size, differing RCP scenarios used, and the step-change in the Greenland discharge between the historical control and future period further add uncertainty, particularly in term of future salinity, freshwater content, MLD, and convective energy.

The biogeochemical module used here was selected for its simplicity and good results in the northern hemisphere (Castro de la Guardia et al., 2019; Galbraith et al., 2015), however it only solves for phytoplankton as a general class, leaving out of the scope of this work species specific adaptions or complex predator-prey interactions. The biogeochemical model does not include ice algae biology that has been shown to play a significant role in the polar regions total primary production (Lavoie et al., 2005; Mortenson et al., 2020; Sibert et al., 2010).

4.5 Conclusion

This study looks at climate scenarios for northern Baffin Bay and the Pikialasorsuaq; with atmospheric warming, Greenland discharge, and Atlantic Waters acting as the primary drivers of change to the region over the rest of this century. Climatic warming is found to bring significant changes to the physical properties of northern Baffin Bay and Pikialasorsuaq, while impacts on biogeochemical properties are smaller. Over the top 50m increasing air temperature, precipitation, and Greenland runoff act to increase oceanic temperature and heat content at the surface, but bring little change to salinity and freshwater content. Over the top 500m, an increased amount of Atlantic Waters entering Baffin Bay through Davis Strait increases temperature, heat content, and salinity and decreases the freshwater content. Atmospheric warming decreases both sea ice thickness and concentration by significant amounts in the later parts of this century. Ice entering the region through Nares Strait is found to be impacted by the thinning signal, while the weaker ice pack is more susceptible to wind forcing and it is more readily pushed into Baffin Bay. The MLD is largely dependent on Greenland runoff, and consequently the RCP8.5 experiments, which have larger runoff, experience the shallowest MLDs. Further, the MLD is found to respond to regional sea ice in the RCP4.5 experiments. In the beginning of the future period, the sea ice area flux increases and mixed layers are slightly damped. Though, by the end of the study period (2070), a largely decreased sea ice concentration promotes deeper mixing. Uncertainty is greatest in the salinity and freshwater content changes due to the large difference in the two Greenland discharge scenarios, while changes to temperature and heat content are relatively consistent between ensemble members. Low spring sea ice concentration and shallows MLDs causes a 20 day advance in the spring bloom, but primary production rates remain similar throughout the future period. Total alkalintity and dissolved oxygen concentration changes are small when considering the annual mean, but vary seasonally. Climatic warming puts into question the future formation of the polynya, which have a significant impact on humans and animals which rely on this unique ecosystem. This study looks at climate scenarios for northern Baffin Bay and the Pikialasorsuaq; with atmospheric warming, Greenland discharge, and Atlantic Waters acting as the primary drivers of change to the region over the rest of this century. Overall these results suggest that the eastern side of the polynya will form with some regularity, however the ability for the warm, Atlantic Water to mix with the surface depends on the strength of the stratification. We also show that these physical changes lead to alterations in the phytoplankton bloom dynamics which has the potential to cause a mismatch of resources and consumers in the future.

Bibliography

Arora, V., Scinocca, J., Boer, G., Christian, J., and adn et al., K. D. (2011). Carbon emission limits required to satisfy future representative concentration pathways of greenhouse gases. *Geophysical Research Letters*, 38.

Bailey, D., Rhines, B., and H´akkinen, S. (2005). Formation and pathways of north atlantic deep water in a coupled ice-ocean model of the arctic-north atlantic oceans. *Climate Dyn*, 25:497–516.

Bamber, J., Tedstone, A., King, M., Howat, I., Enderlin, E., van den Broeke, M., and Noel, B. (2018). Land ice freshwater budgets of the arctic and north atlantic oceans: 1. data, methods, and results. *Journal of Geophysical Research: Oceans*, 123.

Barnier, B., LeSommer, J., Molines, J., Pendruff, T., Treguier, S. T. A., and et al. (2007). Eddy-permitting ocean circulation hindcasts of the past decades. *CLIVAR-Exchanges*, 12:8–10.

Braun, M., Thiombiano, A., Vieiria, M., and Stadnyk, T. (2020). The changing climatology of hudson bay (1981-2070). *Elementa: Science of the Anthropocene. In press*.

Castro de la Guardia, L., Garcia-Quintana, Y., Claret, M., Hu, X., Galbraith, E., and Myers, P. (2019). Assessing the role of high-frequency winds and sea ice loss on arctic phytoplankton blooms in and ice-ocean-biogeochemical model. *Journal of Geophysical Research: Biogeosciences*, 124.

Castro de la Guardia, L., Hu, X., and Myers, P. (2015). Potential positive feedback between greenland ice sheet melt and baffin bay heat content on the west greenland shelf. *Geophysical Research Letters*, 42:4922–4930.

Curry, B., Lee, C., and Petrie, B. (2011). Volume, freshwater, and heat fluxes through davis strait, 2004-2005. *J. Phys. Oceanogr.*, 41:429–436.

Curry, B., Lee, C., Petrie, B., Moritz, R., and Kwok, R. (2014). Multiyear volume, liquid freshwater and sea ice transport through davis strait, 2004-2010. *J. Phys. Oceanogr.*, 44:1244–1266.

DeVries, T. (2014). The oceanic anthropogenic co2 sink: Storage, air-sea fluxes, and transports over the industrial era. *Global Biogeochem. Cycles*, 28:631–647.

Donner, L. and Coauthors (2011). The dynamical core, physical parameterizations, and basic simulation characteristics of the atmospheric circulation component am3 of the gfdl global coupled model cm3. *Journal of Climate*, 24:3484–3519.

Dukhovskoy, D., Myers, P., Platov, G., Timmermans, M.-L., Curry, B., Proshutinsky, A., Bamber, J., Chassignet, E., Hu, X., Lee, C., and Somavilla, R. (2016). Greenland freshwater pathways in the sub-arctic seas from model experiments with passive tracers. *Journal of Geophysical Research*, 121:1–31.

Dukhovskoy, D., Yashayaev, I., Proshutinsky, A., Bamber, J., Bashmachnikov, I., Chassignet, E., Lee, C., and Tedstone, A. (2019). Role of greenland freshwater anomaly in recent freshening in the subpolar north atlantic. *Journal of Geophyiscal Research: Oceans*, 124.

Dumont, D., Gratton, Y., and Arbetter, T. (2009). Modeling the dynamics of the north water polynya ice bridge. *Journal of Physical Oceanography*, 39:1448–1461.

Dunbar, M. and Dunbar, M. (1972). The history of the north water. *Proceedings of the Royal Society. Proceedings of the Royal Society of Edinburgh, Section B*, 72:231–241.

Dunlap, E. and Tang, C. (2006). Modelling the mean circulation of baffin bay. *Atmosphere-Ocean*, 44:99–109.

Fichefet, T. and Morales-Maqueda, M. (1997). Sensitivity of a global sea ice model to the treatment of ice thermodynamics and dynamics. *J. Geophy. Res.*, 102:12609–12646.

Frajka-Williams, E., Rhines, P., and Eriksen, C. (2014). Horizontal stratification during deep convection in the labrador sea. *J. Phys. Oceanogr.*, 44:220–228.

Galbraith, E., Dunne, J., Gnanadesikan, A., Slater, R., Sarmiento, J., Dufour, C., de Souze, G., Bianchi, D., Claret, M., Rodger, K., and Marvasti, S. (2015). Complex functionality with minimal computation: Promis and pitfalls of reduced-tracer ocean biogeochemistry models. *J. Adv. Model. Earth. Syst.*, 7:2012–2028.

Garcia, H., Locarnini, R., Boyer, T., Antonov, J., Baranova, O., Zweng, M., and Johnson, D. (2014a). World ocean atlas 2013: Dissolved oxygen, apparent oxygen utilization, and oxygen saturation. *S. Lavitus, Ed. A, Mishonov Technical Ed.*, 3.

Garcia, H., Locarnini, R., Boyer, T., Antonov, J., Baranova, O., Zweng, M., and Johnson, D. (2014b). World ocean atlas 2013: Dissolved inorganic nutrients (phosphate, nitrate, silicate). *S. Lavitus, Ed. A, Mishonov Technical Ed.*, 3.

Garcia-Quintana, Y., Courtois, P., Hu, X., Pennelly, C., Kieke, D., and Pyers, P. (2019). Sensitivity of labrador sea water formation to changes in model resolution, atmospheric forcing and freshwater input. *Journal of Geophysical Research: Oceans*, 2014.

Grivault, N., Hu, X., and Myers, P. (2018). Impact of surface stress on the volume and freshwater transport through the canadian arctic archipelago from a high-resolution numerical simulation. *Journal of Geophysical Research: Oceans*, 123:9038–9060.

Holdsworth, A. and Myers, P. (2015). The influence of high-frequency atmospheric forcing on the circulation and deep convection of the labrador sea. *Journal of Climate*, 28:4980–4996.

Hu, X. and Myers, P. (2014). Changes to the canadian arctic archipelago sea ice and freshwater fluxes in the twenty-first century under the intergovernmental panel on climate change a1b climate scenario. *Atmosphere-Ocean*, 52(4):331–350.

Hunke, E. and Dukowicz, J. (1997). An elastic-viscous-plastic model for sea ice dynamics. *Journal of Physical Oceanography*, 27:1849–1867.

Ingram, R., Bácle, J., Barber, D., Gratton, Y., and Melling, H. (2002). An overview of physical processes in the north water.

Key, R., Olsen, A., van Heuven, S., Lauvset, S. K., Velo, A., Lin, X., Schirnick, C., Kozyr, A., Tanhua, T., Hoppema, M., Jutterström, S., Steinfeldt, R., Jeansson, E., Ishi, M., Perez, F. F., and Suzuki, T. (2015). Global ocean data analysis project, version 2 (glodapv2), ornl/cdiac-162, nd-p093.

Klein, B., LeBlanc, B., Mei, Z.-P., Beret, R., Michaud, J., Mundy, C.-J., von Quillfeldt, C., Garneau, M.-E., Roy, S., Gratton, Y., Cochran, J., Bélanger, S., Larouche, P., Pakulski, J., Rivkin, R., and Legengre, L. (2002). Phytoplankton biomass, production and potential export in the north water. *Deep-Sea Res.*, 49:4983–5002.

Kwok, R. (2005). Variability of nares strait ice flux. *Journal of Geophysical Research Letters*, 32.

Lauvset, S., Key, R., Olsen, A., van Heuven, S., Velo, A., Lin, X., Schirinkick, C., Kozyr, A., Tanhua, T., Hoppema, M., Jutterstr´om, S., Steinfeldt, R., Jeansson, E., Ishii, M., Peréz, F., Suzuki, E., and Watelet, S. (2016). A new global interior ocean mapped climatology: the $1^{\circ}1^{\circ} glodapversion2. EarthSystemScienceData, 8 : 325 - -340.$

Lavoie, D., Denman, K., and Michel, C. (2005). Modeling ice algal growth and decline in a seasonally ice-covered region of the Arctic (Resolute Passage, Canadian Archipelago). *Journal of Geophysical Research*, 110(C11):C11009.

Lenaerts, J., Bars, D. L., van Kampenhout, L., Vizcaino, M., Enderlin, E., and van den Broeke, M. (2015). Representing greenland ice sheet freshwater fluxes in climate models. *Geophysical Research Letters*, 42.

Lewis, E., Ponton, D., Legendre, L., and LeBlanc, B. (1996). Springtime sensible heat, nutrients and phytoplankton in the northwater polynya, canadian arctic. *Continental Shelf Research*, 16:1775–1781, 1783–1792.

Madec, G. (2008). Nemo ocean engine. *Note du Pole de modélisation*, (27).

Madec, G. and the NEMO System Team (2016). Nemo ocean engine. *Scientific Notes of Climate Modelling Center*, 27:1288–1619.

Marchese, C., Albuoy, C., Tremblay, J.-E., Dumont, D., D'Ortenzio, F., Vissault, S., and B´elanger, S. (2017). Changes in phytoplankton bloom phenology over the north water (now) polynya: a response to changing evironmental conditions. *Polar Biology*, 40:1721–1737.

Maxwell, J. (1981). Climate regions of the canadian arctic archipelago. *Arctic*, 34:225–240.

McGeehan, T. and Maslowski, W. (2012). Evaluation and control mechansims of volume and freshwater export through the canadian arctic archipelago in a high-resolution pan-arcitc ice-ocean model. *Journal of Geophysical Research*, 117(C00D14).

Mei, Z.-P., Legendre, L., Gratton, Y., Trembley, J.-E., LeBlanc, B., Klein, B., and Gosselin, M. (2003). Phytoplankton production in the north water polynya: size-fractions and carbon fluxes, april to july 1998.

Melling, H., Gratton, Y., and Ingram, G. (2002). Ocean circulation within the norh water polynya of baffin bay. *Atmosphere-Ocean*, 39:301–325.

Mortenson, E., Steiner, N., Monahan, A. H., Hayashida, H., Sou, T., and Shao, A. (2020). Modeled Impacts of Sea Ice Exchange Processes on Arctic Ocean Carbon Uptake and Acidification (1980–2015). *Journal of Geophysical Research: Oceans*, 125(7):1–20.

Münchow, A. (2016). Volume and freshwater flux observations from nares strait to the west greenland at daily time scales from 2003 to 2009. *J. Phys. Oceangr.*, 46:141–157.

Münchow, A., Falkner, K., and Melling, H. (2015). Baffin island and west greenland current systems in northern baffin bay. *Progress in Oceanography*, 132:305–317.

Olsen, A., Key, R., van Heuven, S., Lauvset, S., Velo, A., Lin, X., Schirinkick, C., Kozyr, A., Tanhua, T., Hoppema, M., Jutterstr´om, S., Steinfeldt, R., Jeansson, E., Ishii, M., Per´ez, F., and Suzuki, T. (2016). The global ocean data analysis project version 2 (glodapv2).– an internally consistent data product for the world ocean. *Earth System Science Data*, 8:297–323.

Petersen, I., Hamilton, J., Prinsenberg, S., and Pettipas, R. (2012). Wind forcing and volume transport through lancaster sound. *Journal of Geophysical Research*, 117.

Sibert, V., Zakardjian, B., Saucier, F., Gosselin, M., Starr, M., and Senneville, S. (2010). Spatial and temporal variability of ice algal production in a 3D ice–ocean model of the Hudson Bay, Hudson Strait and Foxe Basin system. *Polar Research*, 29(3):353–378.

Spreen, G., Kaleschke, L., and Heygster, G. (2008). Sea ice remote sensing using amsr-e 89 ghz channels. *J. Geophys. Res.*, 113(CO2S03).

Stadnyk, T., Derry, S., MacDonald, M., and Keonig, K. (2019). The freshwater system. in kuzyk z, candlish l, eds. *From Science to Policy in the Greater Hudson Bay Marine Region: An Integrated Regional Impact Study (IRIS) of Climate Change and Modernization*, pages 113–154. ArcticNet.

Stadnyk, T., Tefs, A., Broesky, M., Dery, S., Myers, P., and et al. (2020). Changing freshwater contributions to the arctic: a 90-year trend analysis (1981-2070). *Elementa: Science of the Anthropocene*. In review.

Steele, M., Morley, R., and Ermold, W. (2001). Phc: A global ocean hydrography with high-quality arctic ocean. *Journal of Climate*, 14:2079–2087.

Stern, H. and Heide-Jorgensen, M. (2006). Trends and variability of sea ice in baffin bay and davis strait, 1953-2001. *Polar Research*, 22:11–18.

Stirling, I. (1997). The importance of polynyas, ice edges and leads to marine mammals and birds. *Journal of Marine Systems*, 10:9–21.

Tang, C., Ross, C., Yao, T., Petrie, B., DeTracey, B., and Dunlap, E. (2004). The circulation, water masses and sea-ice of baffin bay. *Progress in Oceanography*, 63:183–228.

Thomas, W., Curry, B., Gurdes, R., Hansend, E., Karcher, M., Lee, C., Rudels, C., Spreen, G., de Steur, L., Stewart, K., and Woodgate, R. (2015). Arctic freshwater export: Status mechanism, and prospects. *Global and Planetary Change*, 125:13–35.

Timmermann, R., Goosse, H., Madec, G., Fichefet, T., Ethé, C., and Duliére, V. (2005). On the representation of high latitude processes in the orcalim global coupled sea ice-ocean model. *Ocean Modelling*, 8:175–201.

Tivy, A., Howell, S., Alt, B., McCourt, S., Chagnon, R., Crocker, G., Carrieres, T., and Jackel, Y. (2011). Trends and variability in summer sea ice cover in the canadian arctic archipelago based on the canadian ice service digital archive, 1960-2008 and 1968-2008. *Journal of Geophysical Research*, 116.

Tremblay, J.-E., Gratton, Y., Fauchon, J., and Price, N. (2002). Climatic and oceanic forcing of new, net, and diatom production in the north water. *Deep Sea Research Part II: Topical Studies in Oceanography*, 49:4927–4946.

Vaquer-Sunyer, R. and Duarte, C. (2008). Threshold of hypoxia for marine biodiversity. *Proceedings of the National Academy of Sciences*, 105:15452–15457.

Vincent, R. (2019). A study of the north water polynya ice arch using four decades of satellite data. *Science Reports*, 9(20278).

Watanabe, M. and Coauthors (2010). Improved climate simulaiton by miroc5: Mean states, variability, and climate sensitivity. *Journal of Climate*, 23:6312–6335.

Yao, T. and Tang, C. (2003). The formation and maintenance of the north water polynya. *Atmosphere-Ocean*, 4(3):187–201.

Yukimoto, S. and Coauthors (2012). A new global climate model of the meteorological research institute: Mri-cgcm3 model description and basic performance. *Journal of Meteorological Society of Japan Set II*, 90A:23–64.

Chapter 5

Conclusion

The mean ice thickness across the Arctic has decreased by 1.75m in recent decades (Kwok and Rothrock, 2009). The sea ice extent has decreased at a rate of $-9.1\%/yr.$ (Stroeve et al., 2007) and when only considering the thick, multi-year ice this trend increases to $-15.6\%/decade$ (Comiso, 2012). Sea ice is also found to become more mobile due to warming as open water is conducive to enhanced sea ice velocities (Kwok et al., 2013). Sea ice losses are leaving the surface of the Arctic Ocean exposed to the atmosphere on scales never witnessed before. Further, enhanced freshwater input from melting sea ice, glaciers, and ice sheets increases stratification and has potential to impact ocean circulation.

Ice-ocean models are a foremost tool for studying the Arctic system, though improvements are necessary to best simulate the current state and to predict future changes. Ice-ocean models are not accurately capturing sea ice losses across the Arctic (Stroeve et al., 2007). Current sea ice models use parameters which are often not bounded by physical observations (Hunke, 2010). There is a need to adjust parameters and other key components to best match the observed sea ice on a variety of scales, such as was looked at in Chapter 3 to tune the Louvain-la-Neuve, LIM3 sea ice model for Arctic-scale and in northern Baffin Bay. Additionally, due to the shortcomings of current models, ensemble averages are an important tool for making predictions, such as was used in Chapter 4 to look at the potential impacts to Pikialasorsuaq and adjacent regions due to climate change.

5.1 Key Findings

1. Access key parameters in a state-of-the-art sea ice model (Louvain-la-Neuve LIM3) in modelling Arctic and Pikialasorsuaq sea ice. Then further, choose a set of tuned parameters which best model sea ice for both regions in terms of satellite observed ice concentration and thickness.

Sensitivity experiments highlight that simulated sea ice concentration is relatively insensitive to ice density, the eccentricity of the elliptical yield curve, ice compressive strength, the number of ice thickness categories, and to including nine tidal constituents. Mean thickness, however, shifted by as much as 0.5m when modifying model parameters. On a month-to-month bases, increasing the ice compressive strength from 20000N/m to 60000N/m thinned ice by 0.3m from the control and decreasing the eccentricity of the elliptical yield curve thickens ice by $0.2m$ when compared to the LIM3 Control experiment. Including nine tidal consituents produces the most realistic summer ice concentration. In terms of mean ice velocity, lowering the ice density produces a greater, summer Fram Strait outflow. No other parameter produces significant differences in the mean velocity. In Pikialasorsuaq, the responses to the perturbed parameters are smaller. Ice concentration does not fluctuate by more than 2% between experiments. Thickness sensitivity in Pikialasorsuaq differ in that they are smaller (maximum of $0.05m$ difference between experiments) and result in different thickness responses. In spring months decreasing the eccentricity of the elliptical yield curve and increasing the ice strength thickens ice by $0.05m$ compared to the LIM3 Control. However, in the late-summer the same experiments thin ice by $0.05m$ compared to the LIM3 Control. Finally, lowering the eccentricity of the elliptical yield curve produces a more realistic ice velocity pattern and a ice volume flux consistent with an ice bridge. No experiment is able to properly simulate as much open water as observed in the polynya. A suggested set of tuned parameters is to include nine tidal constituents (K1, K2, M2, M4, N2, O1, P1, Q1, and S2), keeping the ice density at $917kg/m^3$, decreasing the eccentricity of the elliptical yield curve from 2.0 to 1.2, and increase the ice strength from $20000N/m$ to $40000N/m$.

2. Analyze the potential impact of climate warming on Pikialasorsuaq and adjacent regions. Predict the state of the polynya and the changes in oceanic temperature, salinity, stratification, and primary production which are expected to accompany Arctic warming.

A small member climate ensemble is used to analyze the potential impact of climate change on Pikialasorsuaq. By the end of the study period (2070) there are significant ice thickness and concentration losses. Further, there is a fresher, warmer top $50m$ layer and a warmer, more saline top $500m$ layer. The discrepancy between layers is driven by enhanced Greenland melt and an increase in the amount of Atlantic Water penetrating northern Baffin Bay. Future mixed layer depths in the region are determined by the Greenland runoff scenario used. Greater runoff is found to minimize future mixed layer depths. Changes to the ice regime and oceanic temperature and stratification are predicted to impact the formation of the polynya. The eastern side is predicted to continue forming with some regularity while the west side is expected to be impacted by ice moving more readily through Nares Strait into the region.

5.1.1 Limitations and Future Work

Major limitations for both studies stem from the number of experiments used. In Chapter 3, sensitivity experiments with the LIM3 sea ice model analyze four parameters and the use of tidal constituents. The four parameters, ice density, the eccentricity of the elliptical yield curve, ice compressive strength, and the number of ice thickness categories focus in ice mechanical redistribution and dynamics rather than thermodynamic components. An extensive suite of sensitivity experiments which take into account thermodynamic parameters, as well as key oceanic and atmospheric parameters would enhance the study by clarifying which paramters most impact sea ice and provide a greater range of tuning variables to produce the highest quality model output. Future work on LIM3 sensitivities should be focused on expanding the parameters studied as well as the take a closer look at other critical regions as was done for Pikialasorsuaq.

All experiments conducted in both studies (Chapters 3 and 4) are further limited by the coarse resolution of the atmospheric forcing used. A finer scale atmospheric forcing dataset would better capture topographic effects on the wind, particularly in Baffin Bay and the CAA. A more realistic wind would improve sea ice motion in the model and may improve exchanges between the ice-atmosphere-ocean systems.

Future work involving sensitivity studies (Chapter 3) results are wide-ranging. A tuned set of parameters which improves sea ice model output will enhance the output of ocean general circulation models which can be used for studies ranging from smaller scale process analysis to long-term climate change studies. Improved sea ice modelling improves the amount of freshwater in the ocean and critical exchanges of mass, energy, and momentum with the atmosphere. Improving these process opens the door for more accurate findings with these models in the future.

Climate scenario studies continue raise warming flags to the potential changes the Arctic, and rest of the planet, are set to face in the coming decades. Climate models provide an infinite amount of insight to climate change and its impacts and continuing to use these tools is critical to better learn about the complex earth system. In northern Baffin Bay and Pikialasorsuaq specifically, more studies are required to better understand the coming changes. Key results include changes to the Arctic outflow through Smith, Jones, and Lancaster Sounds and the drivers of enhances Atlantic inflow across Davis Strait. Studies of this sort would continue to grow a knowledge base on how the polynya is going to respond to climate change in the coming decades. Additionally, this climate study was limited by the LIM2 sea ice model. LIM2 has too large ice volume flux through Nares Strait and the polynya is not properly simulated. However, this model was selected as new sea ice models, such as LIM3 are not as well tested. Thus, in order to complete a computationally heavy, climate study within reasonable timeline, the LIM2 model was required.

5.2 Thesis Summary

This thesis focuses on modelling sea ice in the Arctic with an emphasis on Pikialasorsuaq, otherwise known as the North Water polynya, in northern Baffin Bay. In the coming decades sea ice is expected to enter a new regime and the Arctic will significantly be impacted. As human continue to impact the climate, well functioning sea ice models are necessary tool to predict changes.

In Chapter 3 sensitivity experiments are run with the LIM3 sea ice model to access the relative importance of parameters related to mechanical redistribution and ice dynamics. Work done tuning parameters will aid in future sea ice and ocean modelling studies by providing more accurate model output in terms of ice thickness, concentration, and motion.

In Chapter 4 a small member climate ensemble is run to look at climate scenarios for Pikialasorsuaq out to 2070. The ensemble provides insight to the potential impacts of climate warming on the polynya, a critical ocean ecosystem. This study further clarifies how the complex processes involved in polynya formation will respond to warming and changes to stratification in northern Baffin Bay.

Significant changes are predicted to impact the region, providing motivation for continued work in an important ecosystem.

In summary, Pikialasorsuaq is a difficult region to accurately resolve using a sea ice model. This thesis aims to improve the ability to accurately model the polynya as well as to predict changes in the coming decades. This region is important to wildlife and humans alike, continued work is needed to protect and understand it.

Bibliography

Comiso, J. (2012). Large decadeal decline of the arctic multiyear ice cover. *Journal of Climate*, 25:1176–1193.

Hunke, E. (2010). Thickness sensitivities in the cice sea ice model. *Ocean Modelling*, 34:137–149.

Kwok, R. and Rothrock, D. (2009). Decline in arctic sea ice thickness from submarine and icesat record: 1958-2008. *Geophysical Research Letters*, 36.

Kwok, R., Spreen, G., and Pang, S. (2013). Arctic sea ice circulation and drift speed: decadal trends and ocean currents. *Journal of Geophysical Research: Oceans*, 118:2408–2425.

Stroeve, J., Holland, M., Meier, W., Scambos, T., and Serreze, M. (2007). Arctic sea ice decline: Faster than forecast. *Geophysical Research Letters*, 34(L09501).

Bibliography

Aagaard, K. and Carmack, E. (1989). The role of sea ice and other freshwater in the arctic circulation. *Journal of Geophysical Research*, 94:14485–14498.

Alkire, M., Morison, J., Schweiger, A., Zhang, J., Steele, M., Peralta-Ferriz, C., and Dickinson, S. (2017). A meteoric water budget for the arctic ocean. *Journal of Geophysical Research: Oceans*, 122:10020–10041.

Arora, V., Scinocca, J., Boer, G., Christian, J., and adn et al., K. D. (2011). Carbon emission limits required to satisfy future representative concentration pathways of greenhouse gases. *Geophysical Research Letters*, 38.

Asplin, M., Lukovich, J., and Barber, D. (2009). Atmsheric forcing of the beaufort sea ice gyre: Surface pressure climatology and sea ice motion. *Journal of Geophysical Research: Oceans*, 114.

Asselin, R. (1972). Frequency filter for time integration. *Monthly Weather Review*, 100(6):487–490.

Babko, O., Rothrock, D., and Maykut, G. (2002). Role of rafting in the mechanical redistribution of sea ice thickness. *J. Geophy. Res.*, 107:3113.

Bailey, D., Rhines, B., and H´akkinen, S. (2005). Formation and pathways of north atlantic deep water in a coupled ice-ocean model of the arctic-north atlantic oceans. *Climate Dyn*, 25:497–516.

Bamber, J., Tedstone, A., King, M., Howat, I., Enderlin, E., van den Broeke, M., and Noel, B. (2018). Land ice freshwater budgets of the arctic and north atlantic oceans: 1. data, methods, and results. *Journal of Geophysical Research: Oceans*, 123.

Bamber, J., van den Broeke, M., Ettema, J., Lenaerts, J., and Rignot, E. (2012). Recent large increases in freshwater fluxes from greenland into the north atlantic. *Geophysical Research Letters*, 39(19).

Barnier, B., LeSommer, J., Molines, J., Pendruff, T., Treguier, S. T. A., and et al. (2007). Eddy-permitting ocean circulation hindcasts of the past decades. *CLIVAR-Exchanges*, 12:8–10.

Bitz, C., Holland, M., Weaver, A., and Eby, M. (2001). Simulating the ice-thickness distribution in a coupled climate model. *J. Geophy. Res.*, 106:2441–2463.

Bitz, C. and Lipscomb, W. (1999). An energy-conserving thermodynamic model of sea ice. *J. Geophys. Res.*, 104:15669–15677.

Bouillion, S., Maqueda, M. M., Fichefet, T., and Legat, V. (2009). An elastic-visous-plastic sea ice model formulated on arakawa b and c grids. *Ocean Modelling*, 27(3-4):174–184.

Braun, M., Thiombiano, A., Vieiria, M., and Stadnyk, T. (2020). The changing climatology of hudson bay (1981-2070). *Elementa: Science of the Anthropocene. In press*.

Castro de la Guardia, L., Garcia-Quintana, Y., Claret, M., Hu, X., Galbraith, E., and Myers, P. (2019). Assessing the role of high-frequency winds and sea ice loss on arctic phytoplankton blooms in and ice-ocean-biogeochemical model. *Journal of Geophysical Research: Biogeosciences*, 124.

Castro de la Guardia, L., Hu, X., and Myers, P. (2015). Potential positive feedback between greenland ice sheet melt and baffin bay heat content on the west greenland shelf. *Geophysical Research Letters*, 42:4922–4930.

Cavelieri, D. and Parkinson, C. (2012). Arctic sea ice variability and trends, 1979-2006. *J. Geophys. Res.*, 113.

Comiso, J. (2012). Large decadeal decline of the arctic multiyear ice cover. *Journal of Climate*, 25:1176–1193.

Connolley, W., Gregor, J., Hunke, E., and McLaren, A. (2004). On the consistent scaling of terms in the sea-ice dynamics equation. *J. Phys. Oceanogr.*, 34:1776–1780.

Cox, G. and Weeks, W. (1988). Numerical simulations of the profile of properties of undeformed first-year sea ice during growth season. *J. Geophy. Res.*, 93:12449–12460.

Curry, B., Lee, C., and Petrie, B. (2011). Volume, freshwater, and heat fluxes through davis strait, 2004-2005. *J. Phys. Oceanogr.*, 41:429–436.

Curry, B., Lee, C., Petrie, B., Moritz, R., and Kwok, R. (2014). Multiyear volume, liquid freshwater and sea ice transport through davis strait, 2004-2010. *J. Phys. Oceanogr.*, 44:1244–1266.

Dai, A., Qian, T., Trenberth, K., and Milliman, J. (2009). Changes in continental freshwater discharge from 1948 to 2004. *Journal of Climate*, 22:2773–2792.

Dai, A. and Trenberth, K. (2002). Estimates of freshwater discharge from continents: Latitudinal and seasonal veriations. *Journal of Hydrometeorology*, 3:660–687.

DeVries, T. (2014). The oceanic anthropogenic co2 sink: Storage, air-sea fluxes, and transports over the industrial era. *Global Biogeochem. Cycles*, 28:631–647.

Dickson, R., Rudels, B., Dye, S., Karcher, M., Meincke, J., and Yashayaev, I. (2007). Current estimates of freshwater flus through arctic and sub-arctic seas. *Progress in Oceanography*, 73:210–230.

Donner, L. and Coauthors (2011). The dynamical core, physical parameterizations, and basic simulation characteristics of the atmospheric circulation component am3 of the gfdl global coupled model cm3. *Journal of Climate*, 24:3484–3519.

Dukhovskoy, D., Myers, P., Platov, G., Timmermans, M.-L., Curry, B., Proshutinsky, A., Bamber, J., Chassignet, E., Hu, X., Lee, C., and Somavilla, R. (2016). Greenland freshwater pathways in the sub-arctic seas from model experiments with passive tracers. *Journal of Geophysical Research*, 121:1–31.

Dukhovskoy, D., Yashayaev, I., Proshutinsky, A., Bamber, J., Bashmachnikov, I., Chassignet, E., Lee, C., and Tedstone, A. (2019). Role of greenland freshwater anomaly in recent freshening in the subpolar north atlantic. *Journal of Geophyiscal Research: Oceans*, 124.

Dumont, D., Gratton, Y., and Arbetter, T. (2009). Modeling the dynamics of the north water polynya ice bridge. *Journal of Physical Oceanography*, 39:1448–1461.

Dunbar, M. and Dunbar, M. (1972). The history of the north water. *Proceedings of the Royal Society. Proceedings of the Royal Society of Edinburgh, Section B*, 72:231–241.

Dunlap, E. and Tang, C. (2006). Modelling the mean circulation of baffin bay. *Atmosphere-Ocean*, 44:99–109.

Dupont, F., Higginson, S., Bourdallé-Badie, R., Lu, Y., Roy, F., Smith, G., Lemieux, J.-F., Garric, G., and Davidson, F. (2015). A high-resolution ocean and sea-ice modelling system for the arctic and north atlantic oceans. *Geosci. Model Dev.*, 8:1577–1594.

Ferry, N., Greiner, E., Garric, G., Penduff, T., Treiguier, A.-M., and Reverdin, G. (2008). Glorys-1 reference manual for stream 1 (2002 - 2007), glorys project report. *GLORYS project report*.

Fichefet, T. and Morales-Maqueda, M. (1997). Sensitivity of a global sea ice model to the treatment of ice thermodynamics and dynamics. *J. Geophy. Res.*, 102:12609–12646.

Flato, G. and Hibler, W. (1995). Ridging and strength is modeling the thickness distribution of arctic sea ice. *Journal of Geophysical Research: Oceans*, 100(C9):18611–18626.

Frajka-Williams, E., Rhines, P., and Eriksen, C. (2014). Horizontal stratification during deep convection in the labrador sea. *J. Phys. Oceanogr.*, 44:220–228.

Galbraith, E., Dunne, J., Gnanadesikan, A., Slater, R., Sarmiento, J., Dufour, C., de Souze, G., Bianchi, D., Claret, M., Rodger, K., and Marvasti, S. (2015). Complex functionality with minimal computation: Promis and pitfalls of reduced-tracer ocean biogeochemistry models. *J. Adv. Model. Earth. Syst.*, 7:2012–2028.

Garcia, H., Locarnini, R., Boyer, T., Antonov, J., Baranova, O., Zweng, M., and Johnson, D. (2014a). World ocean atlas 2013: Dissolved oxygen, apparent oxygen utilization, and oxygen saturation. *S. Lavitus, Ed. A, Mishonov Technical Ed.*, 3.

Garcia, H., Locarnini, R., Boyer, T., Antonov, J., Baranova, O., Zweng, M., and Johnson, D. (2014b). World ocean atlas 2013: Dissolved inorganic nutrients (phosphate, nitrate, silicate). *S. Lavitus, Ed. A, Mishonov Technical Ed.*, 3.

Garcia-Quintana, Y., Courtois, P., Hu, X., Pennelly, C., Kieke, D., and Pyers, P. (2019). Sensitivity of labrador sea water formation to changes in model resolution, atmospheric forcing and freshwater input. *Journal of Geophysical Research: Oceans*, 2014.

Goosse, H. and Fichefet, T. (1999). Importance of ice-ocean interactions for the global ocean circulation: a model study. *J. Geophy. Res.*, 104:23337–23355.

Griffies, S. (2004). *Princeton, N.J. : Princeton University Press.*

Grivault, N., Hu, X., and Myers, P. (2018). Impact of surface stress on the volume and freshwater transport through the canadian arctic archipelago from a high-resolution numerical simulation. *Journal of Geophysical Research: Oceans*, 123:9038–9060.

Grivault, N. and Myers, P. (2018). Impacts of surface stress on volume and freshwater transport in the canadian arctic archipelago from a high resolution numerical simulation. *Journal of Geophysical Research*, 123:9038–9060.

Haapala, J. (2000). On the modelling of ice-thickness redistribution. *Journal of Glaciology*, 46(154):427–437.

Hibler, W. (1979). A dynamic-thermodynamic sea ice model. *Journal of Physical Oceanography*, 9:815–846.

Hibler, W. (1980). Modeling a variable thickness sea ice cover. *Monthly Weather Review*, 108:1943–1973.

Holdsworth, A. and Myers, P. (2015). The influence of high-frequency atmospheric forcing on the circulation and deep convection of the labrador sea. *Journal of Climate*, 28:4980–4996.

Holland, D., Mysak, L., Manak, D., and Oberhuber, J. (1993). Sensitivity study of a dynamic thermodynamic sea ice model. *Journal of Geophysical Research: Oceans*, 98.

Holland, M., Bitz, C., Hunke, E., Lipscomb, W., and Schramm, J. (2006a). Influence of the sea ice thickness distribution on polar climate in ccdm3. *J. Clim.*, 19:2398–2414.

Høoyland, K. (2002). Consolidation of first-year sea ice ridges. *J. Geophy. Res.*, 107(C6):3062.

Howell, S., Brady, M., Derkens, C., and Kelly, R. (2016). Recent changes in the sea ice area flux through the beaufort sea during the summer. *Journal of Geophysical Research: Oceans*, 121:2659–2672.

Howell, S., Derkksen, C., Pizzolato, L., and Brady, M. (2015). Multiyear ice replenishment in the canadian arctic archipelago: 1997-2013.

Howell, S., Wohlleben, T., Dabboor, M., Derksen, C., Komarov, A., and Pizzolato, L. (2013). Recent changes in teh exchange of sea ice between the arctic ocean and the canadian arctic archipelago. *Journal of Geophysical Research: Oceans*, 118:3595–3607.

Hu, X. and Myers, P. (2014). Changes to the canadian arctic archipelago sea ice and freshwater fluxes in the twenty-first century under the intergovernmental panel on climate change a1b climate scenario. *Atmosphere-Ocean*, 52(4):331–350.

Hu, X., Myers, P., and Lu, Y. (2019). Pacific water pathways in the arctic ocean and beaufort gyre in two simulations with different horizontal resolution. *Journal of Geophysical Research: Oceans*, 124:6414–6432.

Hu, X., Sun, J., Chan, T., and Myers, P. (2018). Thermodynamic and dynamic ice thickness contributions on the canadian arctic archipelago in nemo-lim2 numerical simulations. *The Cryosphere*, 12:1233–1247.

Hunke, E. (2001). Viscous-plastic sea ice dynamics with the evp model: Linearization issues. *Journal of Computational Physics*, 170(1):1849–1867.

Hunke, E. (2010). Thickness sensitivities in the cice sea ice model. *Ocean Modelling*, 34:137–149.

Hunke, E. and Dukowicz, J. (1997). An elastic-viscous-plastic model for sea ice dynamics. *Journal of Physical Oceanography*, 27:1849–1867.

Hunke, E. and Dukowicz, J. (2002). The elastic-viscous-plastic sea ice dynamics model in general orthogonal curvilinear coordinates on a sphere-incorporation of metric terms. *Monthly Weather Review*, 130:1848–1865.

Ingram, R., Bácle, J., Barber, D., Gratton, Y., and Melling, H. (2002). An overview of physical processes in the north water.

Johannessen, O., Bengtsson, L., Miles, M., Kuzmina, S., Semenov, V., Alakseev, G., Nagurnyi, A., Zakharov, V., Bobylev, L., Pettersson, L., Hasselmann, K., and Cattle, H. (2004). Arctic climate change: observed and modelled temperature and sea-ice variability. *Tellus A: Dynamic Meteorology and Oceanography*, 56:328–341.

Karcher, M., Smith, J., Kauker, F., Gerdes, R., and Smiethie, W. (2012). Recent changes in the arctic ocean circulation revealed by iodine-129 observations and modelling. *Journal of Geophysical Research*, 117.

Key, R., Olsen, A., van Heuven, S., Lauvset, S. K., Velo, A., Lin, X., Schirnick, C., Kozyr, A., Tanhua, T., Hoppema, M., Jutterström, S., Steinfeldt, R., Jeansson, E., Ishi, M., Perez, F. F., and Suzuki, T. (2015). Global ocean data analysis project, version 2 (glodapv2), ornl/cdiac-162, nd-p093.

Kim, J., Hunke, E., and Lipscomb, W. (2006). Sensitivity analysis and parameter tuning scheme for global sea-ice modeling. *Ocean Modelling*, 14:61–80.

Klein, B., LeBlanc, B., Mei, Z.-P., Beret, R., Michaud, J., Mundy, C.-J., von Quillfeldt, C., Garneau, M.-E., Roy, S., Gratton, Y., Cochran, J., Bélanger, S., Larouche, P., Pakulski, J., Rivkin, R., and Legengre, L. (2002). Phytoplankton biomass, production and potential export in the north water. *Deep-Sea Res.*, 49:4983–5002.

Kovacs, A. (1996). Sea ice. part 1, bulk salinity versus ice floe thickness. In *Technical Report 96-7*. Cold Regions Research and Engineering Laboratory, Hanover, New Hampshire.

Kurtz, N. and Harbeck, J. (2017). Cryosat-1 level-4 sea ice elevation, freeboard, and thickness, version 1. rdeft4.

Kwok, R. (2005). Variability of nares strait ice flux. *Journal of Geophysical Research Letters*, 32.

Kwok, R. and Rothrock, D. (2009a). Decline in arctic sea ice thickness from submarine and icesat record: 1958-2008. *Geophysical Research Letters*, 36.

Kwok, R. and Rothrock, D. (2009b). Decline in artic sea ice thickness from submarine and icesat records: 1958-2008. *Geophysical Research Letters*, 36(L15501).

Kwok, R., Spreen, G., and Pang, S. (2013). Arctic sea ice circulation and drift speed: decadal trends and ocean currents. *Journal of Geophysical Research: Oceans*, 118:2408–2425.

Kwon, M. and Lee, H. (2016). The effect of tides on the volume of sea ice in the arctic ocean. *Ocean Science Journal*, 51:183–194.

Large, W. and Yeager, S. (2004). Diurnal to decadal global forcing for ocean and sea-ice models: The data sets and flux climatologies. *No. NCAR/TN-460+STR*. University Corporation for Atmospheric Research.

Lauvset, S., Key, R., Olsen, A., van Heuven, S., Velo, A., Lin, X., Schirinkick, C., Kozyr, A., Tanhua, T., Hoppema, M., Jutterstr´om, S., Steinfeldt, R., Jeansson, E., Ishii, M., Peréz, F., Suzuki, E., and Watelet, S. (2016). A new global interior ocean mapped climatology: the $1^{\circ}1^{\circ}glodapversion2.EarthSystemScienceData, 8:325--340$.

Lavoie, D., Denman, K., and Michel, C. (2005). Modeling ice algal growth and decline in a seasonally ice-covered region of the Arctic (Resolute Passage, Canadian Archipelago). *Journal of Geophysical Research*, 110(C11):C11009.

Lee, C., Curry, B., Petrie, B., Azetsu-Scott, K., and Gobat, J. (2014). Arctic outflow west of greenland: Mass and freshwater fluxes at davis strait.

Lenaerts, J., Bars, D. L., van Kampenhout, L., Vizcaino, M., Enderlin, E., and van den Broeke, M. (2015). Representing greenland ice sheet freshwater fluxes in climate models. *Geophysical Research Letters*, 42.

Leppäranta, M., Lensu, M., Koslof, P., and Witch, B. (1995). The life story of a first-year sea ice ridge. *Cold Regions Science and Technology*, 23(3):279–290.

Lewis, E., Ponton, D., Legendre, L., and LeBlanc, B. (1996). Springtime sensible heat, nutrients and phytoplankton in the northwater polynya, canadian arctic. *Continental Shelf Research*, 16:1775–1781, 1783–1792.

Lipscomb, W. (2001). Remapping the thickness distribution in sea ice models. *J. Geophys. Res.*, 106(C7):13989–14000.

Lipscomb, W., Hunke, E., Maslowski, W., and Jackaci, J. (2007). Ridging, strength, and stability in high-resolution sea ice models. *J. Geophy. Res.*, 112:C0329.

Madec, G. (2008). Nemo ocean engine. *Note du Pole de modélisation*, (27).

Madec, G., Delecluse, P., Imbard, M., and Levy, C. (2008). Opa 8 ocean general ciruclation model - reference model. tech rep., lodyc/ipsl note 11.

Madec, G. and the NEMO System Team (2016). Nemo ocean engine. *Scientific Notes of Climate Modelling Center*, 27:1288–1619.

Malmgren, F. (1927). On the properties of sea ice in the norwegian north polar expedition with the 'maud'. *Scientific Results*, pages 1–67.

Marchese, C., Albuoy, C., Tremblay, J.-E., Dumont, D., D'Ortenzio, F., Vissault, S., and B´elanger, S. (2017). Changes in phytoplankton bloom phenology over the north water (now) polynya: a response to changing evironmental conditions. *Polar Biology*, 40:1721–1737.

Massonnet, F., Barthélemy, A., Worou, K., Fichefet, T., Vancoppenolle, M., Rousset, C., and Moreno-Chamarro, E. (2019). On the discretization of the ice thickness distribution in the nemo3.6-lim3 global ocean-sea ice model. *Geosci. Model Dev.*, 12:3745–3758.

Maxwell, J. (1981). Climate regions of the canadian arctic archipelago. *Arctic*, 34:225–240.

Maykut, G. and Untersteiner, N. (1971). Some results from a time-dependent thermodynamic model of sea ice. *J. Geophy. Res.*, 76:1550–1575.

McGeehan, T. and Maslowski, W. (2012a). Evaluation and control mechanisms of volume and freshwater export through the canadian arctic archipelago in a high-resolution pan-arctic ice-ocean model. *Journal of Geophysical Research*, 117.

McGeehan, T. and Maslowski, W. (2012b). Evaluation and control mechansims of volume and freshwater export through the canadian arctic archipelago in a high-resolution pan-arcitc ice-ocean model. *Journal of Geophysical Research*, 117(C00D14).

McPhee, M. (1992). Turbulent heat flux in the upper ocean under sea ice. *J. Geophy. Res.*, 97(C4):5365–5379.

Mei, Z.-P., Legendre, L., Gratton, Y., Trembley, J.-E., LeBlanc, B., Klein, B., and Gosselin, M. (2003). Phytoplankton production in the north water polynya: size-fractions and carbon fluxes, april to july 1998.

Melling, H. (2002). Sea ice of the northern canadian arctic archipelago. *J. Geophys. Res.*, 107(3181).

Melling, H., Gratton, Y., and Ingram, G. (2002). Ocean circulation within the norh water polynya of baffin bay. *Atmosphere-Ocean*, 39:301–325.

Mellor, G. and Hakkinen, S. (1994). A review of coupled ice-ocean models in the polar oceans and their role in shaping the global environment. *Geophysical Monograph, American Geophysical Union*, 85:21–31.

Melsheimer, C. and Spreen, G. (2019). Amsr2 asi sea ice concentration data, arctic, version 5.4 (netcdf) (july 2012 - december 2018). *PANGAEA*.

Melsheimer, C. and Spreen, G. (2020). Amsr-e asi sea ice concentration data, arctic version 5.4 (netcdf) (june 2002 - september 2011). *PANGAEA*.

Mesinger, F. and Arakawa, A. (1976). Numerical methods used in atmospheric models. *GARP Publication Series No. 17*, I:64.

Moreno-Chamarro, E., Ortega, P., and Massonnet, F. (2020). Impact of the ice thickness distribution discretization on the sea ice concentration variability in the nemo3.6-lim3 global ocean-sea ice model. *Geoscientific Model Development*, 13:4773–4787.

Morison, J., Kwok, R., Peralta-Ferriz, C., Alkire, M., Rigor, I., Andersen, R., and Steele, M. (2012). Changing arctic ocean freshwater pathwats. *Nature*, 481.

Mortenson, E., Steiner, N., Monahan, A. H., Hayashida, H., Sou, T., and Shao, A. (2020). Modeled Impacts of Sea Ice Exchange Processes on Arctic Ocean Carbon Uptake and Acidification (1980–2015). *Journal of Geophysical Research: Oceans*, 125(7):1–20.

Münchow, A. (2016). Volume and freshwater flux observations from nares strait to the west greenland at daily time scales from 2003 to 2009. *J. Phys. Oceangr.*, 46:141–157.

Münchow, A., Falkner, K., and Melling, H. (2015). Baffin island and west greenland current systems in northern baffin bay. *Progress in Oceanography*, 132:305–317.

Olsen, A., Key, R., van Heuven, S., Lauvset, S., Velo, A., Lin, X., Schirinkick, C., Kozyr, A., Tanhua, T., Hoppema, M., Jutterstr´om, S., Steinfeldt, R., Jeansson, E., Ishii, M., Per´ez, F., and Suzuki, T. (2016). The global ocean data analysis project version 2 (glodapv2).– an internally consistent data product for the world ocean. *Earth System Science Data*, 8:297–323.

Parmerter, R. (1975). A model of simple rafting of sea ice. *J. Geophy. Res.*, 80:198=48–1952.

Petersen, I., Hamilton, J., Prinsenberg, S., and Pettipas, R. (2012). Wind forcing and volume transport through lancaster sound. *Journal of Geophysical Research*, 117.

Prather, M. (1986). Numerical advection by convervation of second-order moments. *J. Geophy. Res.*, 91:6671–6681.

Pringle, D., Eicken, H., Trodahl, H., and Backstrom, L. (2007). Thermal conducitivty of landfast antarctic and arctic sea ice. *J. Geophy. Res.*, 112:C04017.

Robert, A. (1966). The integration of a low order spectral form of the primitive meteorological equations. *Journal of the Meteorological Society of Japan*, 44(5):237–245.

Rousset, C., Vancoppenolle, M., Madec, G., Fichefet, T., Flavoni, S., Barthélemy, A., Benshila, R., Chanut, J., Levy, C., Masson, S., and Vivier, F. (2015). The louvain-la-neuve sea ice model lim3.6: global and regional capabilities. *Geosci. Model Dev.*, 8:2991–3005.

Shine, K. and Henderson-Sellers, A. (1985). The sensitivity of a thermodynamic sea ice model to changes in surface albedo parameterization. *J. Geophy. Res.*, 90:2243–2250.

Sibert, V., Zakardjian, B., Saucier, F., Gosselin, M., Starr, M., and Senneville, S. (2010). Spatial and temporal variability of ice algal production in a 3D ice–ocean model of the Hudson Bay, Hudson Strait and Foxe Basin system. *Polar Research*, 29(3):353–378.

Smith, G., Roy, F., Mann, P., Dupont, F., Brasnett, B., Lemieux, J.-F., Laroche, S., and Bélair, S. (2014). A new atmospheric dataset for forcing ice-ocean models: Evaluation of reforecasts using the canadian global deterministic prediction system. *Q. J. Roy. Meteor. Soc.*, 140:881–894.

Sou, T. and Flato, G. (2009). Sea ice in the canadian arctic archipelago: Modelling the past (1950-2004) and future (2041-2060). *Journal of Climate*, 22:2181–2198.

Spreen, G., de Steur, L., Divine, D., Gerland, S., Hansen, E., and Kwok, R. (2020). Arctic sea ice volume export through fram strait from 1992 to 2014. *Journal of Geophysical Research: Oceans*, 125.

Spreen, G., Kaleschke, L., and Heygster, G. (2008). Sea ice remote sensing using amsr-e 89 ghz channels. *J. Geophys. Res.*, 113(CO2S03).

Stadnyk, T., Derry, S., MacDonald, M., and Keonig, K. (2019). The freshwater system. in kuzyk z, candlish l, eds. *From Science to Policy in the Greater Hudson Bay Marine Region: An Integrated Regional Impact Study (IRIS) of Climate Change and Modernization*, pages 113–154. ArcticNet.

Stadnyk, T., Tefs, A., Broesky, M., Dery, S., Myers, P., and et al. (2020). Changing freshwater contributions to the arctic: a 90-year trend analysis (1981-2070). *Elementa: Science of the Anthropocene*. In review.

Steele, M. and Ermold, W. (2007). Steric sea level change in the northern seas. *Journal of Climate*, 20:403–417.

Steele, M., Morley, R., and Ermold, W. (2001). Phc: A global ocean hydrography with high-quality arctic ocean. *Journal of Climate*, 14:2079–2087.

Stern, H. and Heide-Jorgensen, M. (2006). Trends and variability of sea ice in baffin bay and davis strait, 1953-2001. *Polar Research*, 22:11–18.

Stirling, I. (1997). The importance of polynyas, ice edges and leads to marine mammals and birds. *Journal of Marine Systems*, 10:9–21.

Stroeve, J., Holland, M., Meier, W., Scambos, T., and Serreze, M. (2007). Arctic sea ice decline: Faster than forecast. *Geophysical Research Letters*, 34(L09501).

Stull, R. (1988). *An Introduction to Boundary Layer Meteorology*. Dordrecht: Kluwer Academic Publisher.

Tang, C., Ross, C., Yao, T., Petrie, B., DeTracey, B., and Dunlap, E. (2004). The circulation, water masses and sea-ice of baffin bay. *Progress in Oceanography*, 63:183–228.

Tartinville, B., Campin, J.-M., Fichefet, T., and Goosse, H. (2001). Realistic representation of the surface freshwater flux in an ice-ocean general circulation model. *Ocean Modelling*, 3:95–108.

Thomas, W., Curry, B., Gurdes, R., Hansend, E., Karcher, M., Lee, C., Rudels, C., Spreen, G., de Steur, L., Stewart, K., and Woodgate, R. (2015). Arctic freshwater export: Status mechanism, and prospects. *Global and Planetary Change*, 125:13–35.

Thorndike, A., Rothrock, D., Maykut, G., and Colony, R. (1975). The thickness distribution of sea ice. *J. Geophys. Res.*, 80(33):4501–4513.

Timmermann, R., Goosse, H., Madec, G., Fichefet, T., Ethé, C., and Duliére, V. (2005). On the representation of high latitude processes in the orcalim global coupled sea ice-ocean model. *Ocean Modelling*, 8:175–201.

Tivy, A., Howell, S., Alt, B., McCourt, S., Chagnon, R., Crocker, G., Carrieres, T., and Jackel, Y. (2011). Trends and variability in summer sea ice cover in the canadian arctic archipelago based on the canadian ice service digital archive, 1960-2008 and 1968-2008. *Journal of Geophysical Research*, 116.

Travers, C. (2012). Quantifying sea-ice volume flux using moored instrumentation in the bering strait.

Tremblay, J.-E., Gratton, Y., Fauchon, J., and Price, N. (2002). Climatic and oceanic forcing of new, net, and diatom production in the north water. *Deep Sea Research Part II: Topical Studies in Oceanography*, 49:4927–4946.

Tremblay, L.-B. and Hakkinen, M. (2007). Estimating the sea-ice compressive strength from satellite derived sea-ice drift and ncep reanalysis data. *Journal of Physical Oceanography*, 36:2165–2172.

Vancoppenolle, M., Fichefet, T., and Bitz, C. (2005). On the sensitivity of underformed arctic sea ice to its vertical salinity profile. *Geophy. Res. Let.*, 32:L16502.

Vancoppenolle, M., Fichefet, T., and Bitz, C. (2006). Modeling the salinity profile of undeformed arctic sea ice. *Geophy. Res. Let.*, 33:L21501.

Vancoppenolle, M., Fichefet, T., Goosse, H., Bouillon, S., Madec, G., and Maqueda, M. A. M. (2009). Simulating the mass balance and salinity of arctic and antarctic sea ice. 1. model description and validation. *Ocean Modelling*, 27(1):33–53.

Vaquer-Sunyer, R. and Duarte, C. (2008). Threshold of hypoxia for marine biodiversity. *Proceedings of the National Academy of Sciences*, 105:15452–15457.

Vincent, R. (2019). A study of the north water polynya ice arch using four decades of satellite data. *Science Reports*, 9(20278).

Wadhams, P., Hughes, N., and Rodrigues, J. (2011). Arctic sea ice thickness characteristics in winter 2004 and 2007 from submarine sonar transects. *J. Geophy. Res.*, 116.

Wang, Q., Ilicak, M., Gerdes, R., Drange, H., Aksenov, Y., Bailey, D. A., Bentsen, M., Biastoch, A., Bozec, A., Bóning, C., Cassou, C., Chassignet, E., Coward, A., Curry, B., Danabasoglu, G., Danilov, S., Fernandez, E., Fogli, P., Fujii, Y., Griffies, S., Iovino, D., Jahn, A., Jung, T., Large, W., Lee, C., Lique, C., Lu, J., Masina, S., Nurser, A., Rabe, B., Roth, C., Mélina, D., Samuels, B., Spence, P., Tsujino, H., Valcke, S., Voldoire, A., Wang, X., and Yeager, S. (2016). An assessment of the arctic ocean in a suite of 1239 interannual core-(2) simulations. part 1. sea ice and solid freshwater. *Ocean Modelling*, 99:110–132.

Watanabe, M. and Coauthors (2010). Improved climate simulaiton by miroc5: Mean states, variability, and climate sensitivity. *Journal of Climate*, 23:6312–6335.

Yao, T. and Tang, C. (2003). The formation and maintenance of the north water polynya. *Atmosphere-Ocean*, 4(3):187–201.

Yukimoto, S. and Coauthors (2012). A new global climate model of the meteorological research institute: Mri-cgcm3 model description and basic performance. *Journal of Meteorological Society of Japan Set II*, 90A:23–64.

Zhang, J. (2020). Sea ice properties in high-resolution sea ice models. *Journal of Geophysical Research: Oceans*, 126.